Electrically Small Particles for Energy Harvesting in the Infrared and Microwave Regimes

by

Mohammed R. AlShareef

A thesis
presented to the University of Waterloo
in fulfillment of the
thesis requirement for the degree of
Doctor of Philosophy
in
Electrical and Computer Engineering

Waterloo, Ontario, Canada, 2014

Author's Declaration

I hereby declare that I am the sole author of this thesis. This is a true copy of the thesis, including any required final revisions, as accepted by my examiners.

I understand that my thesis may be made electronically available to the public.

Abstract

Harnessing energy from clean and sustainable resources is of crucial importance to our planet. Several attempts through different technologies have been pursued to achieve efficient and sustainable energy production systems. However, having systems with a high energy harvesting efficiency and at the same time low energy production cost are challenging with the existing technologies. In this research, several novel structures based on electrically small particles are proposed for harvesting the microwave and infrared energy efficiently. First, a proof of concept demonstrates a metamaterial unit cell's ability to harness the ambient electromagnetic energy. A split-ring resonator (SRR) representing the metamaterial unit cell is designed at a microwave frequency (5.8 GHz) and then fabricated by using printed circuit board technology to prove this concept. A bow-tie antenna, operating at the above frequency, is also designed to show the power efficiency improvement achieved by utilizing the SRR. More than 37% of power efficiency is achieved using SRRs-based structure compared to the 13% of the bow-tie antenna. A new efficiency term is also proposed to take into account the size reduction and efficiency advancement resulting from SRR structures. To this end, two comparable arrays of SRRs and bow-tie antennas are made. Power efficiency of 63.2% and 15.3% for the SRRs and bow-tie arrays, respectively, are achieved. Another structure composed of an ensemble of electrically small resonators for harvesting microwave energy is presented. A flower-like structure composed of four electrically small SRRs arranged in a cruciate pattern, each with a maximum dimension of less than $\lambda_o/10$, is shown to achieve more than 43% microwave-to-alternating current (AC) conversion efficiency at 5.67 GHz. Even- and odd-mode currents are realized in the proposed harvester to improve the efficiency and concurrently reduce the dielectric loss in the substrate. An experimental validation is conducted to prove the harvesting capability.

To extend the work to operate at the far-infrared regime, a novel structure based on electrically small resonators is proposed for harvesting the infrared energy and yielding more than 80% harvesting efficiency. The dispersion effects of the dielectric and conductor materials of the resonators are taken into account by applying the Drude model. A new scheme to channel the infrared waves from an array of SRRs is proposed, whereby a wide-bandwidth collector is utilized by employing this new channeling concept. With the same pattern of the flower-like harvester operating in microwave regime, a new structure composed of electrically small SRRs, each of whose greatest length is less than $\lambda_o/21$, is proven to achieve more than 85% of power harvesting efficiency at 0.348 THz. Furthermore, the infrared energy harvesters are fabricated using nano-fabrication tools. At last, the infrared harvesters are experimentally validated with the numerical findings using THz time-domain spectroscopy (THz-TDS).

Acknowledgements

In the Name of Allāh, the Most Beneficent, the Most Merciful. First and foremost, all the praises and thanks be to God Almighty, who has granted me the health, wellness, knowledge and patience to accomplish this overseas academic journey.

I am indebted to my parents for their endless love, thoughts, support and prayers during my study abroad. They have kept asking me if they could be of any help to ease my life and specifically my study in Canada. I owe a debt of gratitude to my lovely wife, Ohood Saud Al-Thunaiyan, who has been a true helpmate, loyal and caring. Certainly, her unique foresight, patience and encouragement lightened the road of this research work. My two beloved sons, Rashed and Saud, I am deeply thankful to both of you for your love and innocent laughs that filled my spare times. I apologize for any difficulties my journey may have caused. I am also obliged to my kind parents-in-law, Saud Al-Thunaiyan and Muneerah Al-Khozaim, for being considerate and supportive to me and my family over the years of my study. I extend my appreciation to my brothers and sisters for their thoughts and encouragement throughout my PhD program.

I would like to express my thanks to my supervisor, Prof. Omar Ramahi, for his supervision and patience through the course of this work. I also extend my gratitude to my PhD exam committee members: Prof. Raafat Mansour, Prof. Mustafa Yavuz and Prof. Bo Cui for their insightful comments and time dedicated to reviewing my thesis. My special thanks go to Prof. Steven M. Anlage for serving on my committee as the external examiner. I appreciate his valuable feedback and his constructive criticism.

I would like to thank all my colleagues and friends for their discussion, help and joyful moments. I would like to thank Dr. Muhammed S. Boybay, Dr. Mohammed Bait-Suwailam, Dr. Abdullah F. Basiouni, Dr. Babak Alavikia, Dr. Zhao Ren, Nael Suwan, Ferhat Aydinoglu, Abdulaziz Alqahtani, Dr. Vahid Nayyeri, Abdulbaset Ali, Miguel Ruphuy, Mohamed Albadawi and Humayra Naosaba. I am also grateful to Dr. Nathan Nelson-Fitzpatrick for his insightful advice regarding nano-fabrication processes and to Dr. Reza Rafi and Aidin Taeb for their time and help on microwave measurements.

I am really thankful to King Abdulaziz City for Science and Technology (KACST) and to the Saudi Arabian Cultural Bureau in Canada for their generous financial and administrative support.

Dedication

To whoever contributes to
bettering this vibrant world

Table of Contents

List of Tables

List of Figures

List of Abbreviations

Abbreviations

SRR	Split Ring Resonator
AC	Alternating Current
TDS	Time-Domain Spectroscopy
MJ	Multi-Junction
WPT	Wireless Power Transmission
EMR	Electromagnetic Radiation
SOI	Silicon-On-Insulator
HCPV	High Concentrated Photovoltaic
IR	Infrared
MIM	Metal-Insulator-Metal
MOM	Metal-Oxide-Metal
DPS	Double-Positive
SNG	Single Negative
ENG	ϵ-Negative
MNG	μ-Negative
DNG	Double Negative
ISM	Industrial, Scientific and Medical
PMMA	Polymethylmethacrylate
EBL	Electron-Beam Lithography
SEM	Scanning Electron Microscope

Chapter 1

Introduction

1.1 Motivation

The massive amount of solar power received by the earth can theoretically supply all human electricity consumption. Thus, many attempts have been going on to exploit this abundant resource, mainly through photovoltaic technologies. Different solar cell efficiencies above 20% have been reported [10]. More recently, multi-junction (MJ) solar cells have proven to convert solar energy with above 40% efficiency [11]. However, the recent solar cell efficiency was achieved under a sunlight concentrator, which basically needs lenses along with the photovoltaic module [1]. Furthermore, the multijunction solar cell is usually built by stacking multi layers with different bandgaps, resulting in sophisticated manufacturing and high production cost.

Other attempts have been devoted to decreasing the production cost of photovoltaic technology by utilizing thin-film silicon solar cells, which have thicknesses of a few micrometers [12–14]. However, the conversion efficiency of thin-film are lower than that of wafer-based solar cells, owing to the weak absorption in such thin thickness. Consequently, many researchers have proposed different methods to enhance light trapping in thin-film solar cells. In particular, silver particles in nanoscale were deposited on top of the thin-film solar cell to increase the scattering cross section, which in turn enhances the light trapping or absorption inside the silicon substrate [15].

Generally speaking, to make photovoltaic technology competitive, its production cost needs to be decreased by a factor of 2-5 compared with fossil fuel. Figure 1.1 shows the leading-edge of solar cell efficiencies, where the highest performance belongs to multijunction concentrator technology.

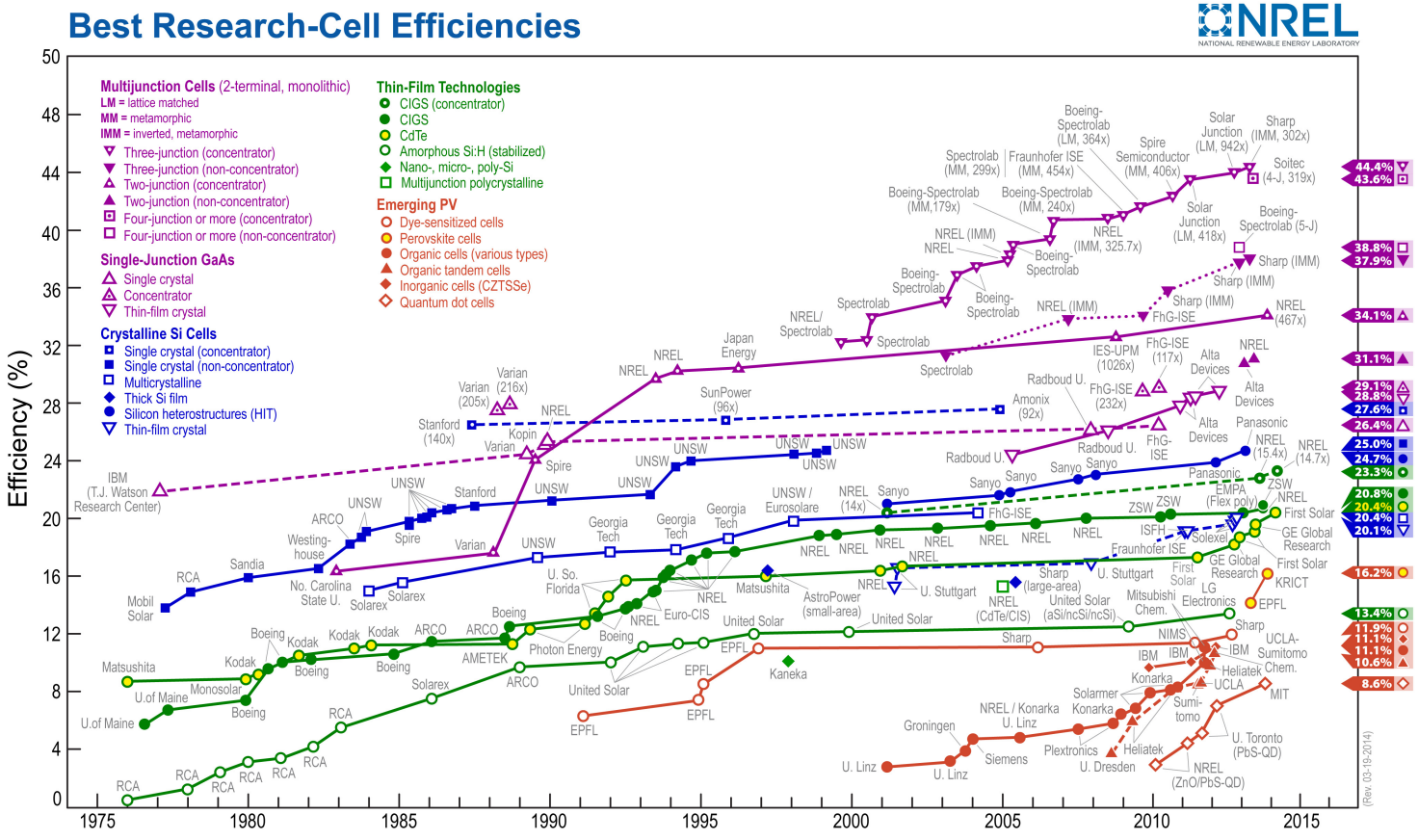

Figure 1.1: Research cell efficiency records. Courtesy of NREL.

Indeed, seeking efficient technologies to provide environmental-friendly energy excites scientists to look back into antennas for energy harvesting purposes. Surprisingly, antenna-based technology was first suggested to trap and convert solar energy by R. Baily in 1975 [16]. Following Baily's proposal, much attention has focused on harnessing solar energy using classical antennas, by which electromagnetic waves can be confined and directed to the intended load.

After the 1990s, Chang's group contributed significantly in the development of systems composed of antennas and rectification circuits for energy harvesting [17]. Many different rectenna systems that consist of three major elements, the antenna, the rectifying circuit and the load, are extensively employed in wireless power transmission (WPT) systems, to harvest and collect ambient RF and solar wave energy. Many publications have considered WPT using classical antennas [6, 17–23]. In particular, McSpadden et al. presented theoretical and experimental investigation of a rectenna element for WPT [17]. This investigation developed a measurement method to characterize a packaged GaAs Schottky barrier diode. McSpadden also showed that the DC conversion efficiency may achieve about 82% at 2.45 GHz. Another patch antenna was designed at millimeter frequency (35 GHz), achieving a 29% RF-to-DC conversion efficiency.

McSpadden and Fan continued to improve DC conversion efficiency by designing a dipole antenna at 5.8 GHz by means of a full wave simulator [6]. An 82% conversion efficiency was achieved by employing a Schottky diode. In 2002, Suh and Chang added another contribution to WPT systems by creating a new dual-frequency rectenna that operates at 2.45 GHz and 5.8 GHz [18, 19]. This structure achieved markedly higher efficiencies than the aforementioned works, with 84.4% and 82.7% of conversion efficiency reported at 2.45 GHz and 5.8 GHz, respectively. A circularly polarized antenna operating at 5.8 GHz was later designed as a component of a rectenna system. Next to the antenna, a coplanar stripline (CPS) filter was positioned to improve the conversion efficiency, which reached 82% [20].

In 2006, Chang's team designed a rectenna system with two pairs of retroactive bow-tie antennas [21]. This rectenna model includes a band pass filter, a Schottky diode and a resistive load, in addition to the antenna. An overall DC conversion efficiency is reported of 84%. Another structure of retroactive rectenna arrays was also designed by Chang's group [22]. Utilizing circularly polarized proximity-coupled microstrip rings, reduced the likelihood that the antenna performance would be affected by the circuit rotation. A measured conversion efficiency for a 2×2 array was reported of 73%.

In view of the importance of miniaturizing in rectenna systems, Tu et al. designed a stepped impedance dipole rectenna that led to about 23% reduction of the dipole antenna

arms' length by utilizing a capacitive patch on each side of the dipole [24]. This work achieved about 76% DC conversion efficiency.

To increase rectenna system power transfer capability, rectenna arrays have been introduced [22, 25–27], and different configurations have also been designed and implemented to gain better power harvesting efficiency. For example, Youn and Park from Korea developed a microstrip patch rectenna centering at 2.45 GHz [26, 27]. A 20×20 array rectenna system was connected in series and parallel to improve the overall efficiency. Although one rectenna element demonstrated about 75% DC conversion efficiency, the entire efficiency from the transmitter to the receiver was only about 33%. However, these designs add great complexity to the rectenna systems in terms of their matching networks and connectivity.

Most of the aforementioned advancements in rectenna systems have focused on either improving the DC conversion efficiency or miniaturizing the rectenna footprint. The emphasis is on the DC conversion efficiency, which it is defined as the ratio of the output DC power dissipated in a load to the AC power received before the rectification circuit. This definition reflects the rectification efficiency only, not whether the antennas or collectors are efficient in trapping the ambient electromagnetic energy. For example, approximately 33% harvesting efficiency from the source to the load was reported in [26, 27], utilizing an array of 400 microstrip patch antennas.

Typically, power harvesting using a classical rectenna is still not able to provide significant amounts of energy and has the disadvantage of design complexity. However, artificially engineered structures (metamaterials) have received much attention in recent years owing to the uniqueness of their electromagnetic properties [28]. Pendry showed that metamaterials possess interesting characteristics such as negative-refractive index and the capability of amplifying evanescent fields [29].

In 2011, a near-field metamaterial structure to enhance the coupling between magnetic dipoles was studied [30]. This work demonstrated an improvement of power transfer efficiency using a metamaterial slab compared with free-space efficiency. In practice, employing multiple unit cells to harvest and collect feasible amounts of power necessitates the design of efficient, miniaturized and cost-effective systems.

1.2 Thesis Objectives

The main goal of this thesis is the design and implementation of an efficient and cost-effective electromagnetic energy harvester that can work in the microwave and infrared

regimes, while concurrently occupying a small footprint area. The work is broken down into the following objectives:

- To analyze and prove the feasibility of an electrically small resonator for electromagnetic energy harvesting in the microwave regime, for which a split-ring resonator (SRR) is chosen as a scope of this analysis.
- To compare the energy harvesting efficiencies per unit area of two arrays of metamaterial unit cells and microstrip antennas, where the two arrays occupy the same footprint area.
- To investigate the coupling effect between any two adjacent SRR cells or microstrip antennas, and whether the coupling contributes positively or negatively to the overall harvesting efficiency.
- To extend the analysis of energy harvesting by a single electrically small resonator to the far infrared frequency regime, and to study the optical properties of the dielectric and conductor materials of the proposed structures, where these materials behave nonlinearly at such high frequencies.
- At infrared frequency, an ensemble of SRR cells is proposed to increase the energy harvesting efficiency. The proposed structure is designed, fabricated using nanotechnology facilities, then is experimentally tested to validate the promising numerical findings.
- A new channeling concept to collect and transfer trapped energy by multiple unit cells to a resistive load is presented for the first time.
- To improve the electromagnetic energy harvesting efficiency, a compact flower-like array consisting of circular SRRs and a central microstrip line is introduced. Two flower-like array harvesters at microwave and far infrared frequencies are designed, analyzed, and validated experimentally with the simulation results.

1.3 Thesis Outline

The remaining parts of this thesis are outlined as follows. Chapter 2 presents the main recent technologies used to harvest ambient electromagnetic radiation. Specifically, photovoltaic technology and recent advancements to improve the conversion efficiency are discussed. Furthermore, the latest nanoantennas that operate in infrared or visible regimes are

introduced, as well as their capability in energy harvesting. An overview of the three main components of rectennas is presented. Utilizing a metamaterial element as a collecting source for energy harvesting, and its advantages over classical antennas are summarized.

Chapter 3 introduces metamaterial and its ability to harvest electromagnetic radiation efficiently. A harvester utilizing an SRR is proposed and compared with a classical bow-tie antenna. The scattering parameters of the SRR harvester and bow-tie antenna with and without loading the structure are computed giving a sense of energy harvesting possibility. Moreover, a new efficiency definition is proposed to take into account the size reduction achieved by utilizing electrically small resonators. Thus, two arrays of bow-tie antennas and SRRs, having the same area and operate at 5.8 GHz, are designed and compared in terms of power harvesting efficiency.

Chapter 4 proposes a new array composed of electrically small resonators to harvest electromagnetic energy in the microwave regime. Each single resonator is designed in a circular shape and has a gap with a sharp and wide opening. The proposed configuration creates in- and out-of-phase currents, which in turn increases the current flow on the channeling line and concurrently limits the dielectric loss in the substrate. The concept of power harvesting with the proposed configuration is validated by measuring the voltage across the resistive load. Moreover, the coupling effect achieved by positioning any two elements of the proposed configuration in a closely-adjacent manner is studied in terms of improving the overall harvesting efficiency.

Chapter 5 extends the concept of using an SRR as an electromagnetic energy collector to be used in the infrared frequency regime. The metal of the resonator, chosen to be silver in this work, is modeled using the Drude dispersion model. An ensemble of SRR cells will be used to increase the energy harvesting efficiency by employing a microstrip line within the SRR array to collect the power from the SRR elements and channel it to a resistive load. The power harvesting efficiencies of the proposed structure at different incident electromagnetic waves are calculated. In addition, the proposed structure has been fabricated using nano-technology tools, and its robustness improved by adding a thin layer of titanium.

Chapter 6 presents the proposed array in Chapter 4, but to operate at infrared frequency after proper scaling and designing procedures. The dispersion effect of metals used in this configuration are computed and considered. The structure is then fabricated using nano-fabrication facility followed by experimental work to prove the harvesting capability.

Lastly, Chapter 7 contains the concluding remarks of this thesis work, its contributions, and the potential developments of the research.

Chapter 2

Recent Advancements in EMR Energy Harvesting

Many efforts have been devoted to exploit new efficient and environmental-friendly energy resources. As photovoltaic technology is the most prominent sustainable energy, it has received the lion's share in sustainable energy research advancements. However, and as of yet, none of the photovoltaic technologies have reported more than 50% conversion efficiency. This relatively low conversion efficiency and the associated high production cost have led researchers to investigate new technologies that pave the way for more efficient and low-cost renewable energy resources. This chapter presents an overview of recent advancements in electromagnetic radiation (EMR) energy harvesting, including photovoltaic technology.

2.1 Photovoltaic Technologies

2.1.1 Thin-Film Silicon Solar Cells

As the most of solar cell devices are made from crystalline silicon wafers, with thicknesses of 200-300 μm, about 40% of the total cost of a solar module fabrication is due to the crystalline silicon wafers. Therefore, many researchers have focused on thin-film solar cells, which have thicknesses that vary from 1-2 μm. However, thin-film solar cells have a weakness related to near-bandgap light absorption, leading to the need to design and investigate new structures to enhance light trapping [31].

Recently, a technique for scattering the incident light from novel metallic nanoparticles at their surface plasmon resonance has been developed. The basic mechanisms of enhancing photocurrent by metallic islands, followed by two different solar cell structures using nanoparticles, are introduced.

Light scattering and near field intensity are the two mechanisms that have been suggested to explain the enhancement of light trapping into solar cells using metallic nanoparticles. Each mechanism is generally characterized by three factors: particle size, the ability of the semiconductor to absorb the light, and the electrical design of the solar cell [31]. Because of the importance of adding nanoparticels to improve light trapping solar cells, the mechanism of scattering by such particles is presented.

At wavelengths of light close to the plasmon resonance of metallic particles, light is intensely scattered owing to a collective oscillation of the conduction electrons in the metal. A point dipole model is considered to explain explicitly the absorption and scattering mechanisms of light. The scattering and absorption cross-sections are given by [32]:

$$C_{scat} = \frac{1}{6\pi}(\frac{2\pi}{\lambda})^4|\alpha|^2, C_{abs} = \frac{2\pi}{\lambda}Im[\alpha] \tag{2.1}$$

where

$$\alpha = 3V[\frac{\varepsilon_p/\varepsilon_m - 1}{\varepsilon_p/\varepsilon_m + 2}] \tag{2.2}$$

is the polarizability of the nanoparticle, and V represents the particle volume. Also, ε_p and ε_m are the dielectric function of the particle and dielectric function of the embedding medium, respectively. It is obvious that when $\varepsilon_p = -2\varepsilon_m$, the particle polarizability tends to be infinity, and at this condition, a resonance known as the surface plasmon occurs. In a particular case, when silver nanoparticles are excited by incident light at resonance, their scattering cross section is tenfold the cross section of silver particles. In other words, if only 10% of the surface area of a device is covered by particles, theoretically, all incident light could be scattered and absorbed [31].

In a work by S. Pillai et al. [15], nanoparticles are used and deposited by thermal evaporation of thin layers of silver followed by annealing. This method is considered the easiest way to deposit metallic particles onto the substrate. Silver is chosen due to its low losses compared to other metallic particles.

Figure 2.1 shows two different silicon cell structures, where 1.25 μm silicon-on-insulator (SOI) test cells and planar PERL (passivated emitter rear locally diffused) Si cells are used. A lateral pn junction diffused into a p-type layer is used to form the SOI cells used in these experiments. Moreover, in order to increase the carrier extraction, the p

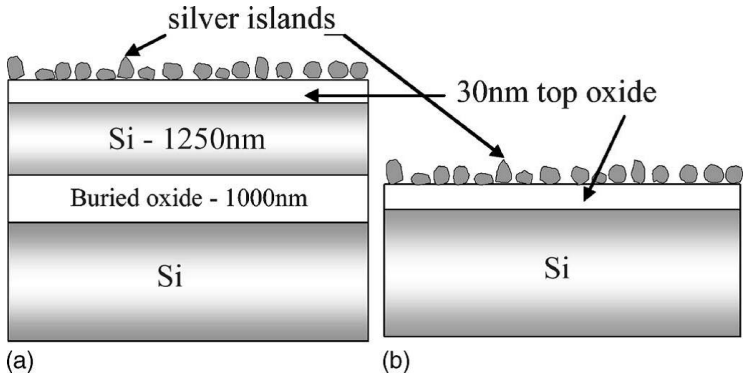

Figure 2.1: The silicon cell structures used in the experiments. (a) Silicon-on-insulator with 1.25 μm active Si and (b) wafer-based 300 μm planar Si cell [15].

and n metal contacts are interdigitated. The thickness of the layers of the first structure (SOI cell) is measured at about 1248 nm for the silicon layer and 1000 nm for the buried oxide layer. Both of the two cells have a top oxide layer of 30 nm thickness; this layer acts as a passivating layer, where the oxide layer thickness is significantly affecting the coupling between the active silicon layer and the plasmons. Although the passivation of the silicon layer is necessary to control the surface recombination, the oxide layer thickness is designed to be low to maintain the coupling to the silicon without losing a reasonable surface passivation.

As presented earlier, a point dipole method has been used for modeling the effect of the plasmons. The effect of material from the emission spectrum and the scattering cross section point of views can be calculated using the model mentioned above. In [15], experimental bare particles' resonance data are used for the initial scattering cross section for light incident from air; thus, a variety of particle shapes and sizes are considered in their work. Also, the absorbtion is neglected in the model, and the extinction is only assumed to be scattering. As the silver island sizes are greater than 100 nm, absorption would be insignificant within the particles above wavelengths of 500 nm, where the radiative efficiency of these particles is high at longer wavelengths.

As shown in Figure 2.2, a device was made from SOI material, and on its lateral p-n junction, silver nanoparticles were deposited [33]. This device can be used in light-emitting diodes and test solar cells. The electroluminescence and photocurrent generated by this device were measured.

The silver nanoparticles showed about a 42% enhancement of the calculated photocurrent compared to the planar device, whereas the grating structure gave only 30% of pho-

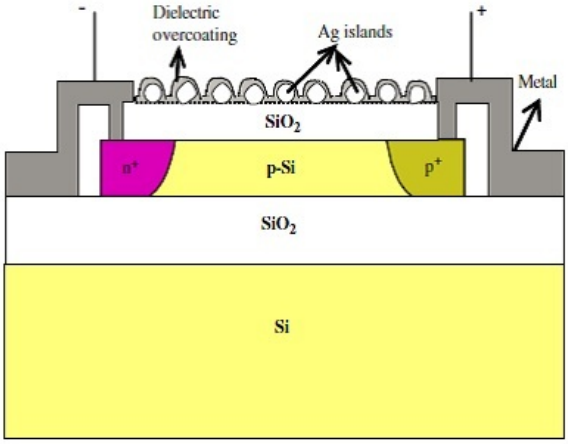

Figure 2.2: Structure of the SOI devices. Layer thicknesses were 35 nm top oxide, 95 nm active Si layer and 408nm buried oxide [33].

tocurrent enhancement in the wavelength range from 500-1100 nm. A thick 300 nm a-Si solar cell structure on glass was modeled using silver nanoparticles and with an optimized TiO_2 rectangular groove grating on the front. The absorptance of the two modeled structures was compared with the planar cell.

In [33], in order to further investigate the absorption enhancement, an ideal dipole was modeled to be able to completely scatter the incident light. Figure 2.3 depicts the potential absorptance enhancement for the ideal dipole modeled on the 95 nm SOI device.

2.1.2 Multi-Junction (MJ) Solar Cells

Having a solar cell able to accept only a narrow spectrum radiation will lead to less recombination within the cell substrate; thus, more power can be extracted. This mechanism has been brought to reality by mechanically stacking cells with different semiconductors [34] or illuminating monochromatic radiation on each cell [35], to name but a few approaches. Monolithic multijunction cells are considered the most common technology for multijunction cells, in which multi solar cells composed of III-V semiconductor types are connected in series along with tunnelling diodes [1]. For example, in [36], three cells backed with a Ge substrate have been stacked, forming a multijunction solar cell with a thickness of more than 200 μm. By this solar cell and at 454 suns, 41.1% conversion efficiency was achieved in Germany.

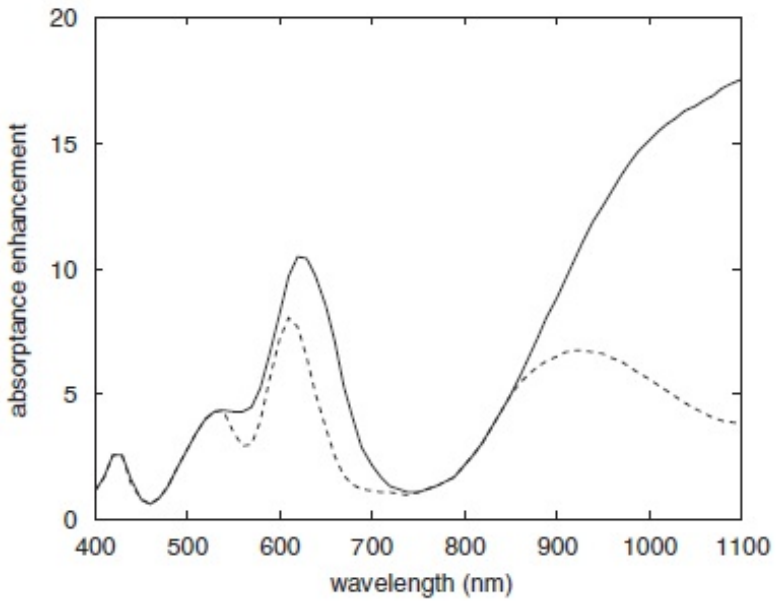

Figure 2.3: Absorptance enhancement for the modeled SOI devices (dotted line) and the potential absorptance enhancement, assuming that all incident light is scattered (solid line) [33].

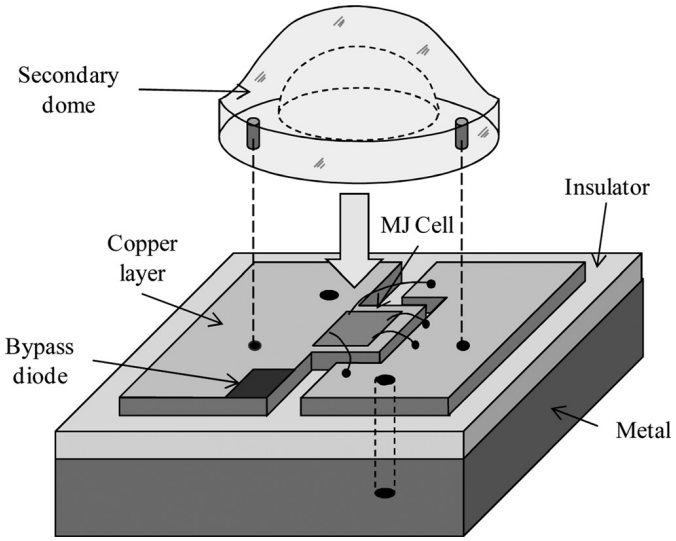

Figure 2.4: High concentrator photovoltaic module combining optics, and a MJ solar cell within the same assembly [2].

The photovoltaic production cost can be lowered by increasing the conversion efficiency in sophisticated solar cells, such as by using a multijunction. But to gain a high efficiency in such cells, high concentrated illumination should be applied in order to produce a high electric power. Therefore, photovoltaic concentrators have been developed [37, 38] aiming to improve the efficiency; thus, cost-effective solar cells are possible.

A canonical configuration is considered one of the most suitable concentrators to be assembled with high efficiency solar cells. Concentrators are generally arranged in modules that form photovoltaic arrays, along with a tracking system [1]. To conceive how complex high efficiency solar cells are, Figure 2.4 depicts a schematic diagram of a multijunction solar cell containing a Fresnel lens to provide a concentrated luminous flux. The solar cell sets on a metallic layer, such as copper or aluminum, to facilitate the wires' connections to the next cells. Furthermore, the metallic layer is backed by a substrate for insulation and thermal transmission purposes [2].

To illustrate how much each element in a photovoltaic module contributes to the module's total cost, a specific module solution consisting of epi-wafers and a multijunction solar cell integrated with a primary (Fresnel lens) and secondary concentrators is considered. Dr. Sala of IES/UPM found that wafers and substrates contribute much more than the other elements for small cell size ($1 \times 1\, mm$). The costs of other parts, such as Fresnel lenses and base plates, are relatively independent of cell size [1].

Table 2.1: Yearly ground efficiency for two photovoltaic plants in different irradiation conditions and for four different photovoltaic technologies [1].

Concept	HCPV	Si Track	Si fixed	Organic
Module efficiency	45.0%	20.0%	20.0%	10.0%
Plant efficiency	40.0%	17.8%	17.8%	8.9%
Ground efficiency, Madrid	8.9%	5.4%	12.1%	6.1%
Ground efficiency, Albuquerque	10.3%	5.7%	12.1%	6.1%

In summary, real-world photovoltaic technology still does not provide highly efficient modules. In [1], Luque calculated the estimated ground efficiency of two large plants, in which, good (Madrid, Spain) and excellent (Albuquerque, NM, USA) irradiation are received. Luque also calculated the efficiencies of four different photovoltaic technologies, as presented in Table 2.1. All the irradiation data were taken from [39]. One can see that high concentrated photovoltaic (HCPV) has the highest module and plant efficiencies. However, if it comes to a practical scenario, HCPV ground efficiency goes down to 10.3% as estimated for the Albuquerque plant.

2.2 Nanoantennas

The visible solar radiation that extends from the 400 nm to the 700 nm wavelength forms only 39% of the whole solar spectrum, while the Infrared (IR) represents 52% [40]. The fact that photovoltaic based technologies are only able to harness the visible light radiation, and yet provide low conversion efficiency, has led to the investigation of alternative technologies for solar energy harvesting. Recently, nanoantennas have received great interest for different applications such as, field enhancing [41], focusing [42] and more interestingly, for solar energy harvesting [3, 5, 43–45].

For solar energy harvesting, a nanoantenna is not only able to harness the visible light, but it can be properly scaled to collect infrared radiation as well. Several researchers have shown the feasibility of energy harvesting utilizing nanoatennas. In particular, a square spiral antenna was numerically shown able to collect and focus an infrared electric field in a central gap [43]. The spiral antenna works at a frequency of 28.3 THz and has a total length of 10.6 μm. However, this work did not calculate any energy conversion efficiency.

Kotter et al. have realized an array of nanoantennas to collect electromagnetic radiation at a wavelength of 6 μm [3]. In their work, approximately 90% absorption was

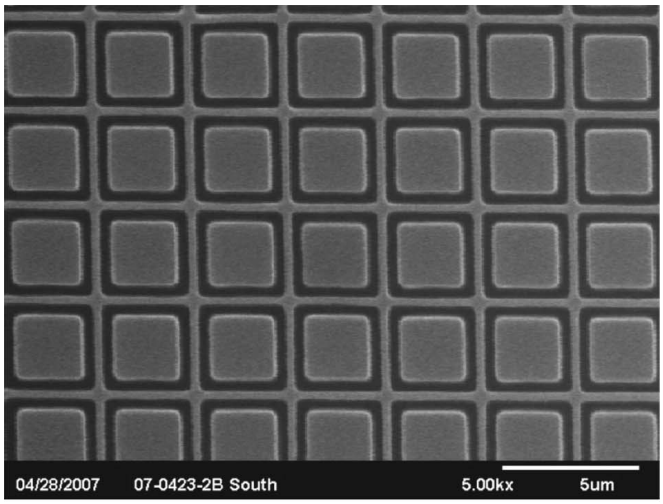

Figure 2.5: SEM image of an array composed of loop nanoantenna designed to operate in infrared regime [3].

achieved using a unit cell of loop antenna, where the arm length of the loop is approximately $> \lambda_o/3$, as depicted in Figure 2.5. Although the ability of electromagnetic infrared energy absorption was proven, the efficiency of collecting or conversion the energy was not accomplished.

Another trend in utilizing nanoantennas is to enhance light trapping in thin-film solar cells. An array of nanoantennas on top of a photovoltaic layer has been designed to excite different nanoantennas' collective modes and then localize the resultant electric fields between the metal parts of the nanoantennas. Consequently, more light is trapped in the photovoltaic layer, which in turn, enhances the photovoltaic absorption [4]. This proposed structure has at least five different layers in addition to the nanoantenna array, which implies complexity and high production cost. Figure 2.6 illustrates a schematic diagram of the thin-film solar cell with nanoantenna arrays.

Providing a DC current to targeted devices or applications from a collected electromagnetic waves requires a rectification mechanism along with the collecting source. The rectification element converts the collected AC current to a consumable DC power, either in high or low frequencies. Hence, different configurations and topologies of rectenna systems have been introduced aiming to efficiently achieve power in worthwhile amounts.

For example, different antenna designs have been proposed for solar energy harvesting in [5]. A log periodic, a square-spiral, and an Archimedean spiral gold antenna were

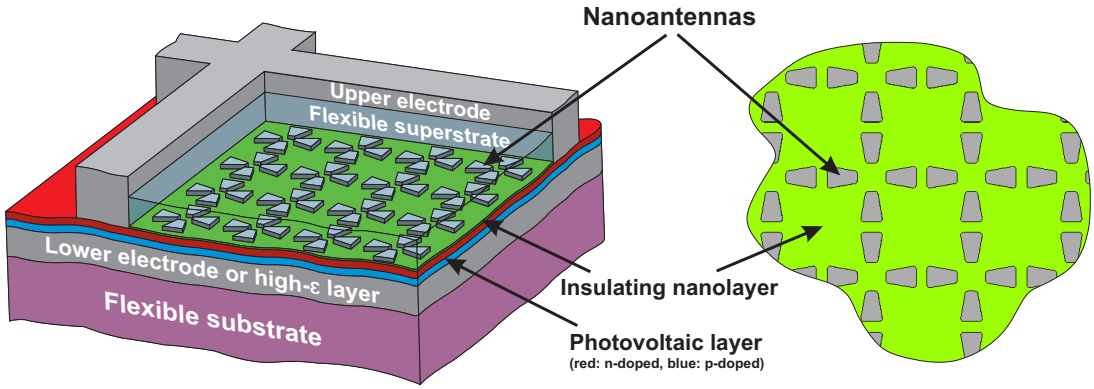

Figure 2.6: A schematic of thin-film solar cell topped with nanoantenna arrays [4].

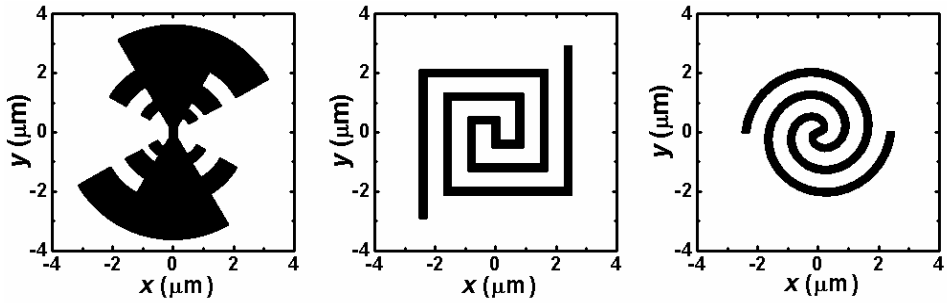

Figure 2.7: broadband solar antennas, (left) log-periodic antenna, (middle) square-spiral antenna and (right) Archimedean-spiral antenna [5].

numerically designed to cover a broad bandwidth ranging from $3\,\mu m$ to $17\,\mu m$ radiation spectrums, as shown in Figure 2.7. These antennas were coupled to two tunneling diodes (Metal-Insulator-Metal and Esaki diodes) to rectify the harvested signals. However, the reported conversion efficiencies are very low and not practical (order of 10^{-6} to 10^{-9}). The authors attributed these low efficiencies to antenna-diode mismatching and to the diodes' weak performance. In more detail, the next section gives an overview of rectenna system elements by which energy collecting and conversion can be accomplished.

2.3 Rectenna Systems

Since the development of rectenna systems, researchers have utilized antennas as power sources for those systems. However, the antennas employed in rectenna systems deliver

only limited power to the rectification circuit. This section describes rectenna system elements to provide a solid background on which to base such advancements.

2.3.1 Antenna as a Collecting Source

The antenna by which a rectenna system can receive electromagnetic radiation is a critical element for energy harvesting and WPT. Hence, many antenna designs have been proposed seeking higher rectenna performance. The half-wavelength printed dipole antenna is extensively used in the literature for WPT purposes, but in such antennas, the total dimension is $\lambda_o/2$, which requires more space compared to the rectification circuit.

The printed dipole antenna is a vertically polarized radiator, so this feature allows the formation of an array to collect more power per unit area [46]. However, a space of $\lambda_o/2$ should be retained between adjacent antennas to suppress mutual coupling. Compromising this spacing will effect antenna efficiency, and the received power will decrease dramatically [47, 48].

In an attempt to shrink the rectenna's physical size, Ziolkowski's group has proposed a rectenna to harvest electromagnetic radiation at 1.5754 GHz, composed of two-cane monopole antennas and backed by a metamaterial unit cell (S-shaped resonator), resulting in a significant rectenna size reduction. About 85% rectifying efficiency was achieved utilizing this electrically small rectenna [49].

Single rectennas are capable of transferring only limited power, forming rectennas into arrays has been studied to increase the harvest and delivery of power. Such arrays can be connected either in series or parallel, or in a mixed configuration. In [50], the total power uniting from an array of rectennas has been studied. The power collected from such an array and its related efficiency issues are based on Nahas' Model. The power efficiency was found to be insensitive to the way the rectennas are connected. Shinohara and Matsumoto [25] demonstrated that power combining in an array of parallel connectivity is higher than that of series connection. They attributed the shortage of power efficiency in their series to the low input power associated with this kind of combination.

2.3.2 Rectifying Devices

The rectification circuit comes immediately after the antenna or integrated within the antenna element, as shown in Figures 2.8a and 2.8b, respectively. Generally, the rectification circuit consists of a matching network and diode for DC conversion. The diode circuit

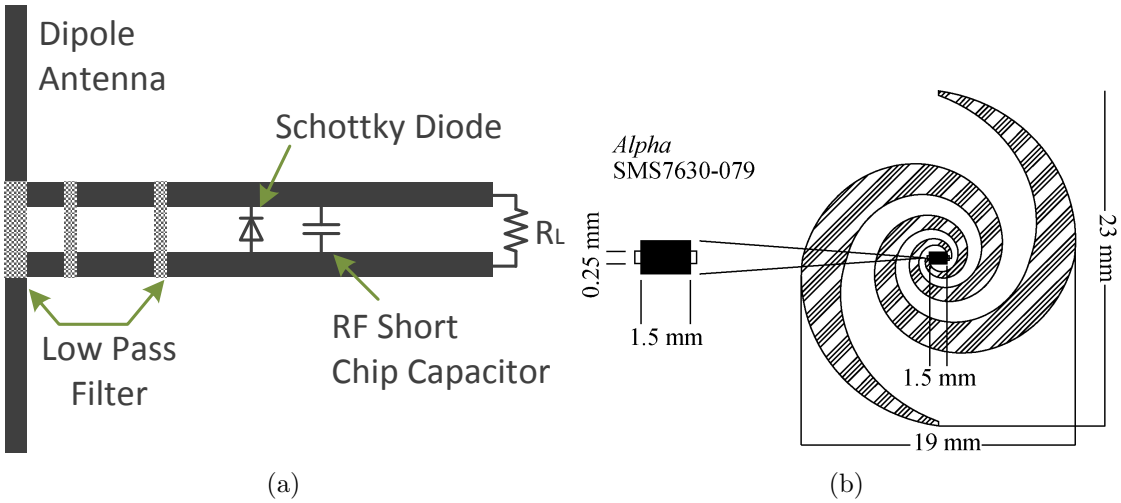

(a) (b)

Figure 2.8: (a) 5.8 GHz printed rectenna element [6] and (b) spiral rectenna integrated with the Schottky diode [7].

is a nonlinear device which causes unwanted harmonics to appear and degrade the overall rectenna efficiency. In other words, the harmonic signals created by the diode can be radiated by the antenna into the surrounding area and then absorbed by the material of the rectenna, which in turn degrades system performance. The harmonic effect can be neglected by utilizing a well-designed filter through which only the fundamental wave can pass.

The Schottky diode is widely used in rectenna systems for WPT. In general, this diode operates at low frequencies up to just a few THzs. Mainly, the Schottky diode can be characterized by three components: series resistance R_s, junction resistance R_j and junction capacitance C_j. The non-linearity of the Schottky diode results from the change of junction resistance with respect to variation of bias and saturation currents through operation. The equivalent circuit model of the Schottky diode is shown in Figure 2.9 [51].

In the reverse bias, the junction resistance R_j is larger than that of the forward bias; this is due to the exponential increase of current as it appears on the I-V characteristic curve. The series or spreading resistance R_s is considered to be parasitic; that is, the current flow lines tend to shrink close to the contact in the semiconductor region. For circular contact cases, and from potential theory, equation 2.3 gives the value of the diode resistance R_s

$$R_s = \frac{1}{2\sigma d} \tag{2.3}$$

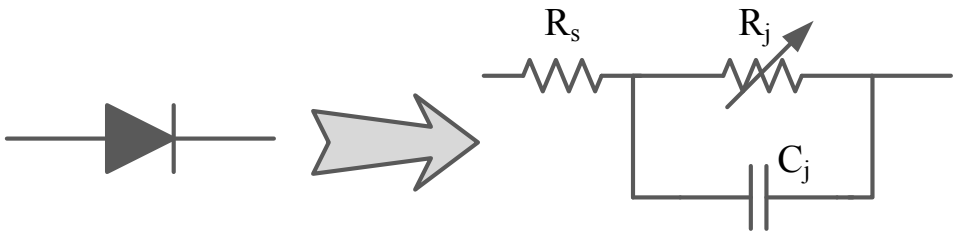

Figure 2.9: Schottky diode equivalent circuit model

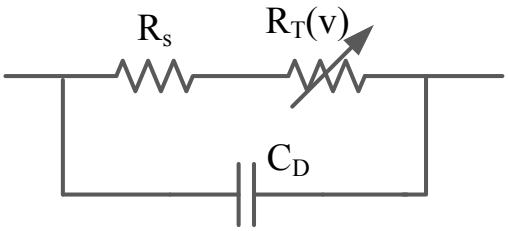

Figure 2.10: MIM diode equivalent circuit model

where σ is the conductivity of the semiconductor material, and d represents the circular contact area diameter. The junction capacitance C_j develops from the charges at the boundary layer. The capacitance value can be evaluated by using the parallel plate capacitance expression in equation 2.4:

$$C_j = \epsilon_r \epsilon_0 \frac{A}{d} \tag{2.4}$$

where A is the contact area, and d represents the barrier thickness. It is obvious that the capacitance is affected by the barrier thickness d, which means that with any change of the applied voltage, the capacitance magnitude will change [52].

In the far infrared to visible spectrums, the rectifying device should be fast in response to accommodate rectennas operating at these high frequencies. The metal-insulator-metal (MIM) is utilized instead of the Schottky diode at high frequencies, owing to the MIM diode fast switching properties. Generally, an MIM diode consists of a thin insulating layer sandwiched between two metallic plates. An MIM diode is a quantum device where the rectification proceeds by tunneling electrons through the insulating barrier [52]. Odashima et al. [53] introduced an equivalent model for an MIM diode, as displayed in Figure 2.10.

This model considers the spread (contact) resistance R_s along with the tunneling resistance R_T, since it gives a valid assumption for the linear as well as square low regions.

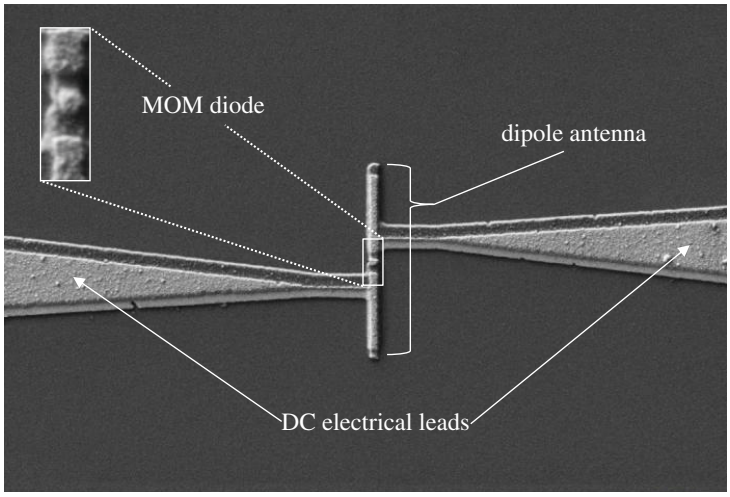

Figure 2.11: IR detectors consisting of antenna-coupled MOM tunnel diode [8].

The zero bias resistance R_0 can be calculated using equation 2.5 [54].

$$R_0 = R_T + R_s \tag{2.5}$$

The capacitance C_D value is also obtained by using the parallel plate capacitance expression cast in equation 2.4.

A practical example of employing an MIM or MOM (metal-oxide-metal) diode at infrared frequency is illustrated in Figure 2.11. Bean et al. developed an IR detector adopting the rectenna system principle, where the rectenna assembles a half-wavelength dipole antenna coupled to an MOM diode [8]. Although this coupled-antenna was designed for IR radiation detection, it can be diverted for IR energy harvesting. Still, the relatively large size of the antenna and DC electrical leads prevent the proper utilization of the footprint area; thus, more miniaturization is needed to gain higher energy harvesting efficiency.

2.3.3 Impedance Matching

Impedance matching has been used to ensure maximum power transmission efficiency in rectenna systems. If well designed, impedance matching lets the input power transfer from the source to the load efficiently. In other words, impedance matching prevents the received energy from being reflected back to the receiving antenna. Due to the non-linearity of some devices used in rectenna systems, such as the Schottky barrier diode, impedance matching is necessary for high power efficiency, specifically at the operating band.

In the case of a reactive component used in a rectifier (inductor or capacitor) connected to a 50 Ω antenna, conjugate impedance matching is vital to eliminate the reactance and match the rectifier to the antenna impedance.

2.4 Metamaterial Particles as a Transducer

As presented in the preceding sections, most rectenna systems have used the antennas as transducer to collect electromagnetic radiation. Typically, power harvesting using a classical antenna still does not provide a highly efficient energy harvesting and has the disadvantages of design complexity and destructive coupling issues. Employing other collecting sources that can achieve high power harvesting efficiency per unit area is necessary; thus, electromagnetic radiation collectors based on electrically small particles (metamaterial) are proposed to meet these demands. Using electrically small particles has many advantages over other approaches:

- Metamaterial resonators are electrically small structures, which miniaturizes the footprint of the harvesting system [30].
- The coupling effect between two adjacent SRR cells is much weaker in comparison to antenna coupling; hence, the distance maintained between cells is much smaller than the $\lambda_o/2$ required by classical antennas.
- The power collected from the single negative media is much higher than that of electromagnetic radiators. A simple comparison between an SRR and a bow-tie antenna demonstrates that the potential power trapped by an SRR is higher than that of the antenna.

However, at high frequencies, the optical properties of the dielectric and conductor materials of the proposed structures should be taken into account, where these materials behave nonlinearly at such high frequencies.

2.5 Conclusion

To conclude, the main recent technologies used to harvest ambient electromagnetic radiation were presented. Specifically, photovoltaic technology and its recent advancements to improve conversion efficiency were discussed. Furthermore, the latest nanoantennas that

operate in infrared or visible regimes were introduced, as well as their ability in energy harvesting. An overview of the three main components that compose rectennas was presented. Utilizing a metamaterial element as a collecting source for energy harvesting, and its advantages over classical antennas were summarized. The next chapter introduces the metamaterial unit cell and its ability to harvest electromagnetic radiation more efficiently than classical bow-tie antennas can.

Chapter 3

Energy Harvesting using Metamaterial Particles

In nature, materials which possess negative macroscopic parameters permittivity, ε, or permeability, μ, are relatively uncommon. However, artificial materials which exhibit a negative media, either a single or double negative, have been subjects of interest. Various applications utilizing metamaterials had been reported, such as cloaking [55], electromagnetic field absorption [56] and sensing [57]. The media can be classified based on their parameters: those with both positive permittivity and permeability($\varepsilon > 0, \mu > 0$) are labeled double-positive (DPS), under which most natural media are classified; those with a negative permittivity and a positive permeability ($\varepsilon < 0, \mu > 0$) are classified as epsilon-negative (ENG); those with a positive permittivity and a negative permeability ($\varepsilon > 0, \mu < 0$) falls under a mu-negative (MNG) classification, and those with both negative permittivity and permeability ($\varepsilon < 0, \mu < 0$), are labeled double-negative (DNG). For this last classification, artificially engineered structures need to be constructed to exhibit these properties. A graphical illustration of these four classifications is shown in Figure 3.1.

3.1 Operational Principle of the Unit Cell of Metamaterial

Recently, the SRR shape has been proposed to exhibit the negative constitutive parameters, either the permittivity ε, or permeability, μ, or both. A magnetic resonance is developed

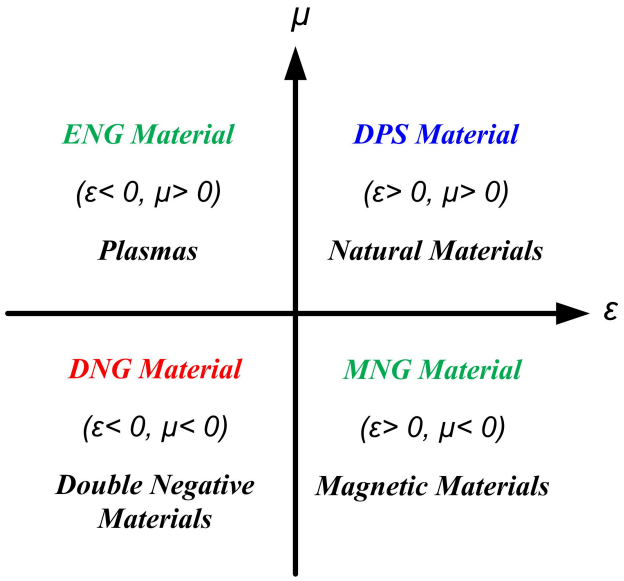

Figure 3.1: Materials classification based on their constitutive parameters ε and μ

by using this type of structure. If an orthogonal magnetic field H^{ext} is applied on the structures shown in Figure 3.2, electromotive force (emf^{ext}) is induced. Near the resonant frequency, the structures can be characterized by the total effective current flowing through their rings.

The capacitive gap in the SRR lets the effective current circulate through the structure and creates a magnetic field normal to the ring, which in turn, develops an inductive reactance of the total impedance of the structure. The real part of this impedance characterizes the finite conductivity loss and magnetic dipole radiation. Therefore, the effective current passing through these unit cells can be formulated as follows [58]:

$$I = \frac{emf^{ext}}{Z_{tot}} = \frac{emf^{ext}}{jwL_{eff} + \frac{1}{jwC_{eff}} + R_{eff}} \tag{3.1}$$

It is obvious that the inclusion (structure) represents an RLC resonator model as illustrated in Figure 3.3. From Faraday's law, the electromotive force (emf^{ext}) can be expressed as [58]

$$emf^{ext} = -jw\phi = -jwBS = -jw\mu_0 NSH^{ext} \tag{3.2}$$

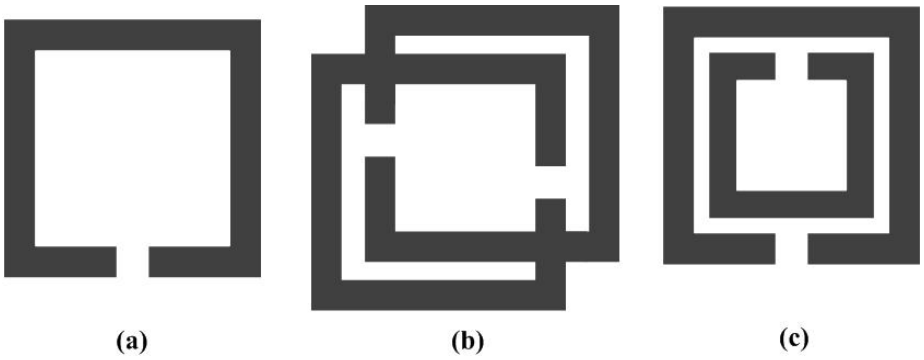

Figure 3.2: Different unit cell structures of the artificial engineered material a) Single SRR b) Broadside-coupled SRR c) Edge-coupled SRR

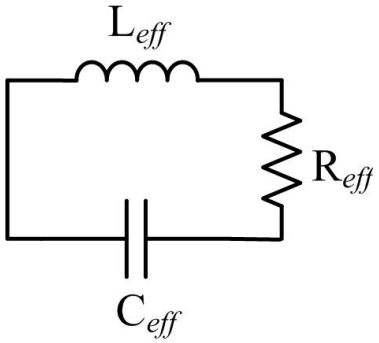

Figure 3.3: Equivalent RLC circuit model of the unit cell of metamaterial

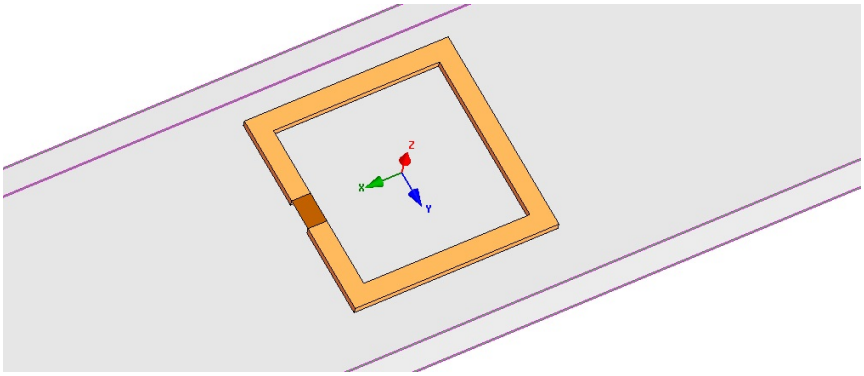

Figure 3.4: Simulation geometry for numerical retrieval of scattering parameters of the SRR

where S is the particle cross-section area excited by the external magnetic field H^{ext}, and N is the number of turns [$N = 1$ for the both cases (a) and (b) of Figure 3.2]. The induced magnetic dipole moment in a single unit cell is calculated as [58]

$$m = \mu_0 NSI = \frac{w^2 \mu_0^2 N^2 S^2 C_{eff} H^{ext}}{1 - w^2 L_{eff} C_{eff} + jw R_{eff} C_{eff}} \tag{3.3}$$

3.2 SRR Ability of Power Harvesting

In this section, a single SRR is modeled and simulated using numerical full-wave analysis to show the ability of power harvesting. A commercial full-wave simulation tool (ANSYS® HFSS™) based on the finite-element method is used to study the SRR response. In order to examine the behavior of the SRR, the scattering parameters, S_{11} and S_{21}, are computed. A vacuum waveguide with the single-negative magnetic metamaterial (split-ring resonator) is excited by two wave ports; appropriate boundary conditions are also applied to force the magnetic field (**H**) to be perpendicular to the inclusion's surface as depicted in Figure 3.4. The geometric dimensions of the resonator are shown in Figure 3.5, and are optimized to obtain its resonance frequency at 5.8 GHz, where the arm length $L = 6.3mm$, arm width $W = 1.1\,mm$, and the gap $g = 0.8\,mm$. This metallic inclusion (resonator) is etched on a dielectric slab with a dielectric constant $\varepsilon_r = 2.2$ and thickness $h = 0.787\,mm$.

Figure 3.6a represents the reflection and transmission coefficients, S_{11} and S_{21}, of this SRR, which resonates at 5.8 GHz. It can also be seen that this resonator, at resonance frequency, exhibits almost a full wave reflection and nothing is transferred through. By

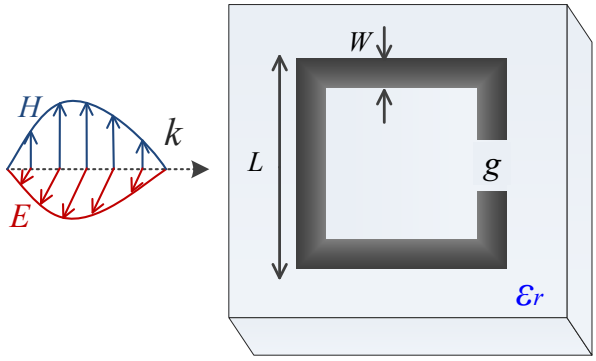

Figure 3.5: Geometric representation of the split ring resonator and its wave vector orientation.

plotting the electric field intensity over the inclusion surface, one can observe that the high field intensity is concentrated in the SRR gap as depicted in Figure 3.7. This observation indicates a high potential voltage which can be seen as a power source or collector. It is worth mentioning that loading a matching impedance on the SRR allows the power absorbed by this ring to be transferred and collected. In order to validate the previous assumption, an optimal resistive sheet ($2.7\mathrm{k}\,\Omega$) is placed across the SRR gap; whereby different resistive loads are varied to obtain the highest power efficiency. The scattering parameters S_{11} and S_{21}, are then computed again to show the effect of placing a matching resistive load.

As illustrated in Figure 3.6b, after applying the resistive load, the SRR demonstrates its ability to absorb or harvest the incident power on its plane. To elaborate, the transmitted and reflected waves are both diminished at resonance frequency, which means that the waves coexist inside the resonator as stored energy.

3.3 Power Harvesting using Metamaterial and Classical Antenna

Maximizing power efficiency is a substantial requirement in power harvesting systems; hence, many structures based on classical antenna have been proposed to gain efficient power collecting. Nevertheless, although marked improvements in terms of power efficiency have been realized, collecting power by means of antennas has some limitations. Therefore, metamaterial-based element is proposed, by which a tremendous power har-

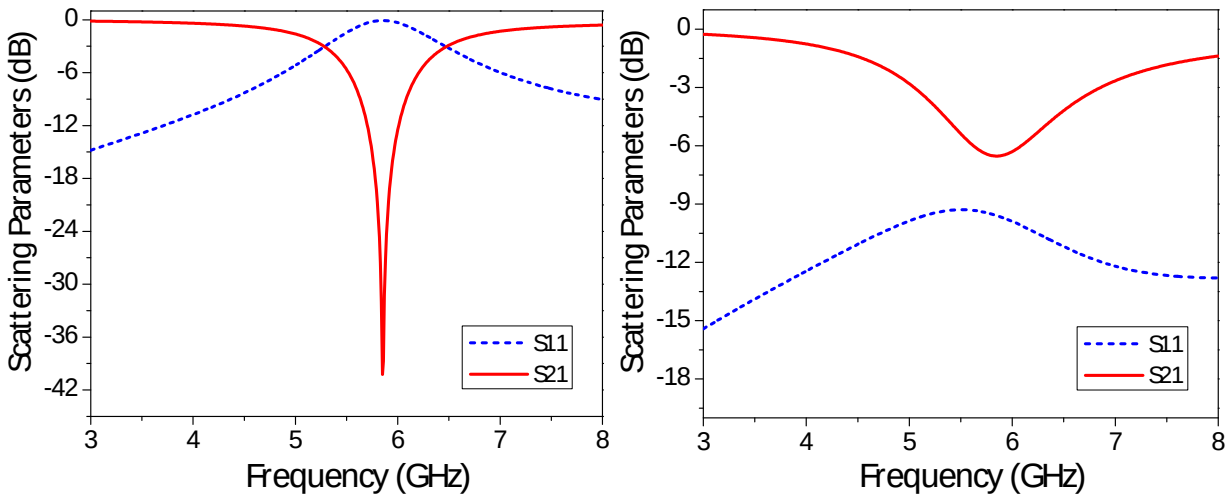

Figure 3.6: Simulated scattering parameters of the SRR. (a) Without loading and (b) with 2.7k Ω resistive load.

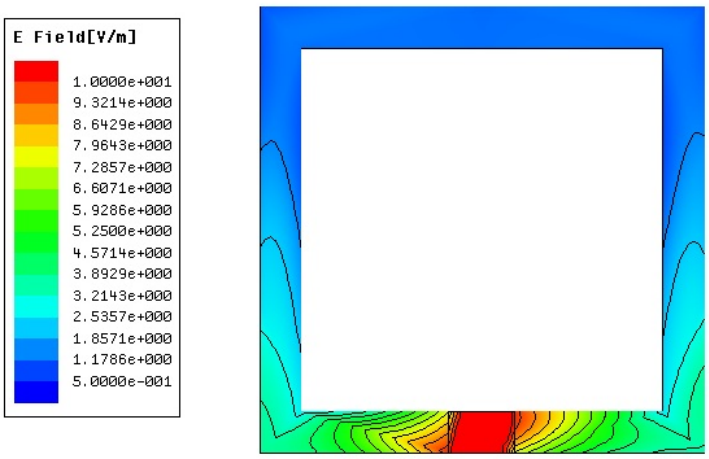

Figure 3.7: Simulation results for the electric field intensity of the SRR

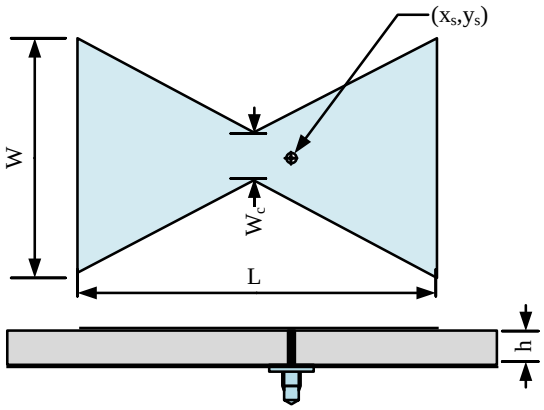

Figure 3.8: Geometry of the designed bow-tie microstrip antenna

vesting capability can be attained. Next, a bow-tie antenna and the SRR are compared to show these efficiency improvements.

A microstrip bow-tie antenna is selected to compare it with SRR due to its low profile. This antenna is designed to operate at the next higher ISM (industrial, scientific and medical) band (5.8 GHz) to miniaturize the aperture size without compromising the element efficiency as claimed in [6]. In [59], a closed-form formula to calculate the resonance frequency, which is based on the bow-tie antenna geometry is developed as follows:

$$\begin{aligned} f_r &= \frac{c \times k_1}{2\pi\sqrt{\varepsilon_e}} \\ \varepsilon_e &= (\frac{\varepsilon_r + 1}{2}) + (\frac{\varepsilon_r - 1}{2})(1 + \frac{12h}{W_e})^{1/2} \end{aligned} \tag{3.4}$$

$$W_e = \frac{W + W_c}{2} \tag{3.5}$$

where ε_e is the effective permittivity, W_e is the effective bow-tie side width, and k_1 is the eigenvalue and obtained by using the Rayleigh-Ritz method as

$$k_1 = 2\sqrt{\delta_1(W + W_c)/(L^2(3W + W_c))} \tag{3.6}$$

where δ_1 is a coefficient and chosen as δ_1= 3.45. The calculated dimensions of the bow-tie antenna are as follows: $W = 9\,mm$, $W_c = 3\,mm$, and $L = 13.81\,mm$, a Rogers 5880 substrate with dielectric constant (ε_r) of 2.2 and thickness (h) of 0.787 mm is used in this

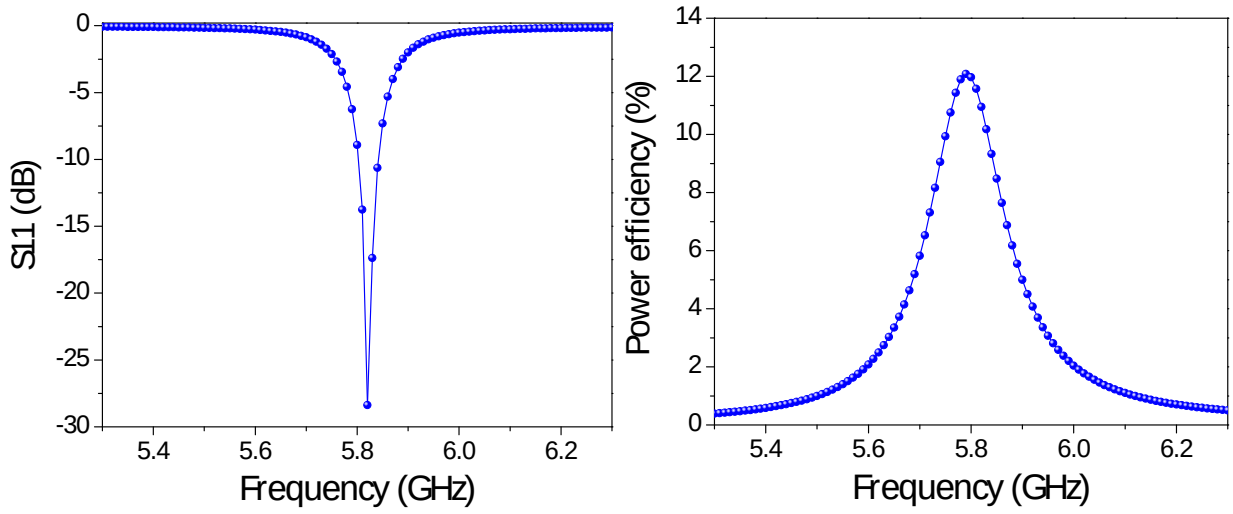

(a) (b)

Figure 3.9: Simulation results of the bow-tie antenna. (a) The reflection coefficient and (b) the bow-tie antenna power efficiency loaded by 50 Ω.

design. A 50 Ω coaxial line probe feeding located at $x_s = 0\,mm$ and $y_s = 0.75\,mm$ is utilized to excite the antenna, and the structure geometry is shown in Figure 3.8. The reflection coefficient S_{11} of the designed bow-tie antenna is illustrated in Figure 3.9a. It is shown that the antenna operates at 5.8 GHz and its bandwidth, which is determined at the 10 dB return loss, is 1.1%. This narrow bandwidth may be attributed to the thin substrate and compact size of the antenna.

After designing both the SRR and bow-tie antenna at 5.8 GHz using the same substrate, a comparison of power efficiency for the two structures are conducted to show the power harvesting improvement using the SRR structure. First, a 50 Ω resistive load is placed over the coaxial line feeding port of the bow-tie antenna, then, a plane-wave perpendicular to the mictrostrip plane is shone to excite the antenna. By applying the Poynting vector, the time-average power is expressed as

$$P = \frac{1}{2} \oint \mathbf{S_{av}}.ds = \frac{1}{2} \oint Re[\mathbf{E} \times \mathbf{H}^*].ds \tag{3.7}$$

where $\mathbf{S_{av}}$ is the average power density, and for an electric field of a uniform plane wave $\mathbf{E}$, the average power density can be calculated as

$$P_D = \frac{|\mathbf{E}^2|}{2\eta} \tag{3.8}$$

The power harvesting efficiency of the bow tie antenna loaded by a 50 Ω resistance is plotted in Figure 3.9b. The power efficiency is computed using the ANSYS® HFSS™ calculator by dividing the power dissipated on the resistive load surface over the power density (P_D) multiplied by the cross-sectional area (A) of the air box, thus:

$$\eta_{eff} = \frac{P_{diss}}{P_D \times A} \tag{3.9}$$

Although the maximum power efficiency occurs at the resonance frequency (5.8 GHz) as is expected, this antenna, which has been used in rectenna systems, shows a low power harvesting capability. In other words, the highest efficiency that can be achieved by this bow-tie antenna is only about 13%.

The same previous steps are applied for the SRR structure to prove the power harvesting enhancement, however, the SRR has a different characteristic impedance. This impedance is much higher than 50 Ω, since it depends on the SRR geometry, such as, the arm length and the gap width. Thus, to achieve the highest possible power efficiency, the resonator should be loaded with a resistance that matches the characteristic impedance. Hence, *it is found that the optimal resistance value of the SRR designed at 5.8 GHz is 2.3kΩ, at which the highest possible harvesting efficiency is achieved at the designed resonance frequency.* A resistive sheet is placed over the SRR gap, where the highest electric field intensity is observed. A substantial power efficiency improvement is realized using the SRR, in which, more than 37% power efficiency is achieved. In other words, the SRR efficiency improvement is more than double that of the bow-tie antenna. Basically, the same picture of bow-tie antenna efficiency holds for SRR, since the highest efficiency happens at the resonance frequency. Figure 3.10 shows the harvesting power efficiency by using the SRR resonator structures SRR loaded by different resistance values.

3.4 Measurement of Power Harvested using SRR

Figure 3.11 illustrates the fabricated SRR utilizing Rogers 5880 board material with dielectric constant (ε_r) of 2.2 and thickness (h) of 0.787 mm. A surface-mounted resistor with an optimal value of (2.7k Ω) is placed across the gap to measure the power dissipated by this load. The block diagram in Figure 3.12 presents the setup for measuring the voltage

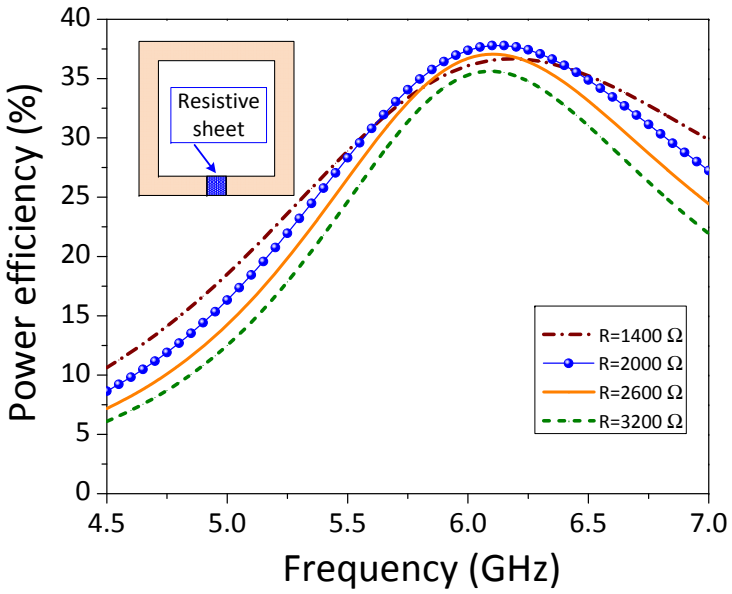

Figure 3.10: Power efficiency of the SRR loaded by different resistances

across the loaded gap. An Agilent Infiniium 12 GHz oscilloscope and Agilent PSG vector signal generator are employed in this measurement. The signal generator is connected to a directional flat patch antenna with an approximate gain of 19 dBi (according to manufacturer data sheet) at 5.8 GHz. The input power of the antenna, which used to excite the SRR, is 24 dBm, and the transmission distance (r) between the antenna and SRR is 10 cm. The voltage across the surface-mounted resistor at 5.8 GHz is measured by means of a single-ended probe and read at 611.5 mV as displayed in Figure 3.13.

To prevent the probe/oscilloscope from affecting the measured value, an important step during the measurement setup was carried out. Precisely, an offset calibration was first performed for the probe to remove unwanted/offset signals rather than the one measured between the two leads of the resistor. In addition, the probe resistance (50k Ω) is much higher than that of the surface-mount resistor (2.7k Ω), so any loading error was negligible.

3.5 Power Harvesting Efficiency per Unit Area

In the preceding section, a harvesting efficiency enhancement using a metamaterial unit cell is introduced. In addition, the proposed idea also provides a footprint miniaturization,

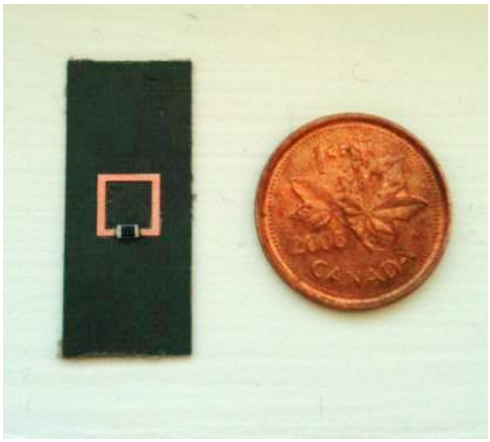

Figure 3.11: 5.8 GHz SRR fabricated on Rogers 5880 board material

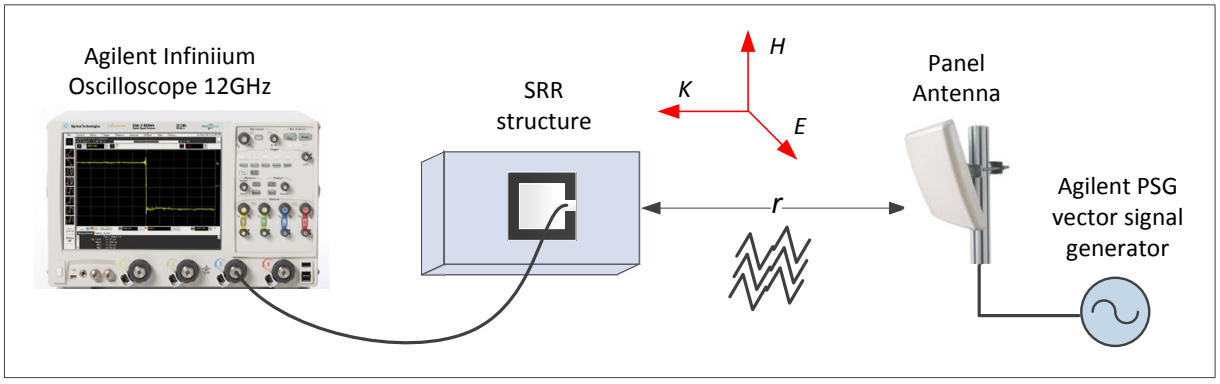

Figure 3.12: Experimental setup to measure the harvested power using SRR

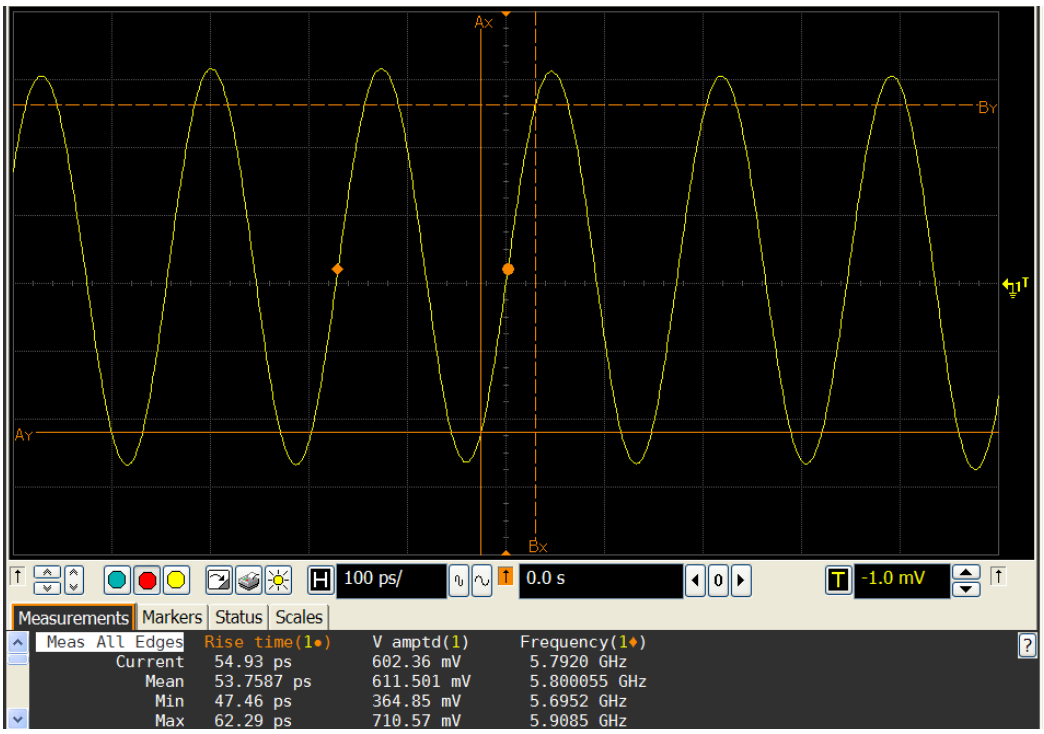

Figure 3.13: AC voltage signal across the loaded gap at 5.8 GHz

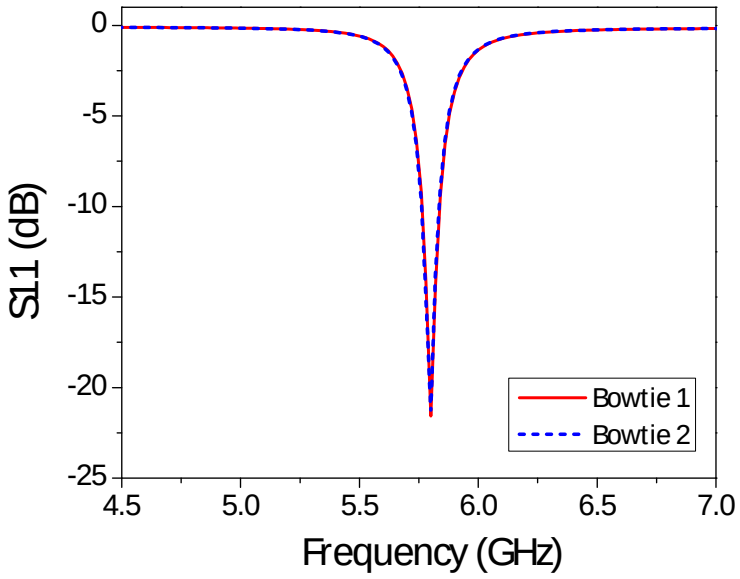

Figure 3.14: Simulated reflection coefficient for the two bow-tie microstrip antennas

thus, a new efficiency term is proposed to take into account the size reduction as well. For that reason, two comparable arrays of SRRs and bow-tie antennas are made to show that miniaturization and efficiency advancement by exploiting SRRs can be gained.

For the first case, an array composed of two bow-tie antennas is designed at ISM band 5.8 GHz. In order to prevent any coupling or cross talking between the two antennas, a separation between them is varied until the coupling becomes suppressed. It is found that the minimum separation is about $\lambda_o/2$, at which, the coupling effect is negligible. To prove the coupling abolition, both of the bow-tie antennas are fed using a coaxial line probe with $50\,\Omega$ characteristic impedance, then, the reflection coefficients S_{11} are calculated. Clearly from Figure 3.14, S_{11} for the two antennas are identical and overlapped, which indicates that cross coupling is almost negligible. The geometry and dielectric material of the two bow-tie antennas used in that array, are similar to the individual one which has been designed earlier in Section 3.3.

Secondly, with the same dimensions of the previous array, another array is made of 21 SRRs. Considering these resonators are electrically small, results in a very compact size compared to the antenna array. Figure 3.15 depicts the two arrays of the bow-tie and SRRs occupying the same area A, in which, $L \times W = 80\,mm \times 30\,mm$.

The two arrays shown in Figure 3.15 are excited by two different orientations of a plane-wave, depending on the array that is excited. For the bow-tie array, an orthogonal plane-

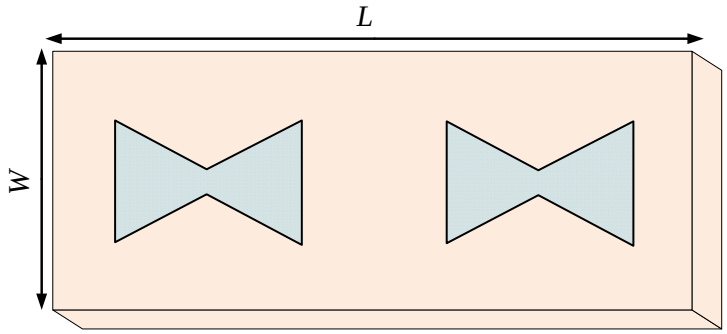

(a) Array of bow-tie microstrip antenna

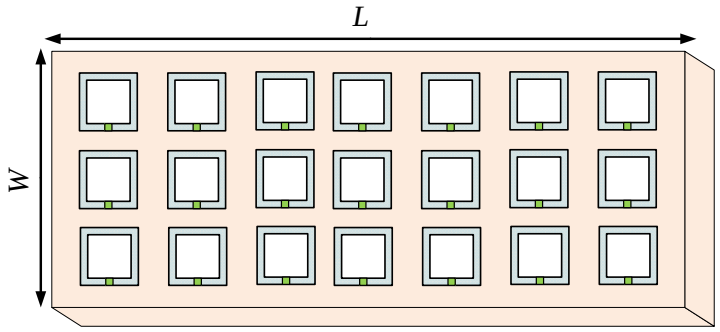

(b) Array of SRR resonator

Figure 3.15: Arrays of the designed bow-tie microstrip antenna and SRR resonator

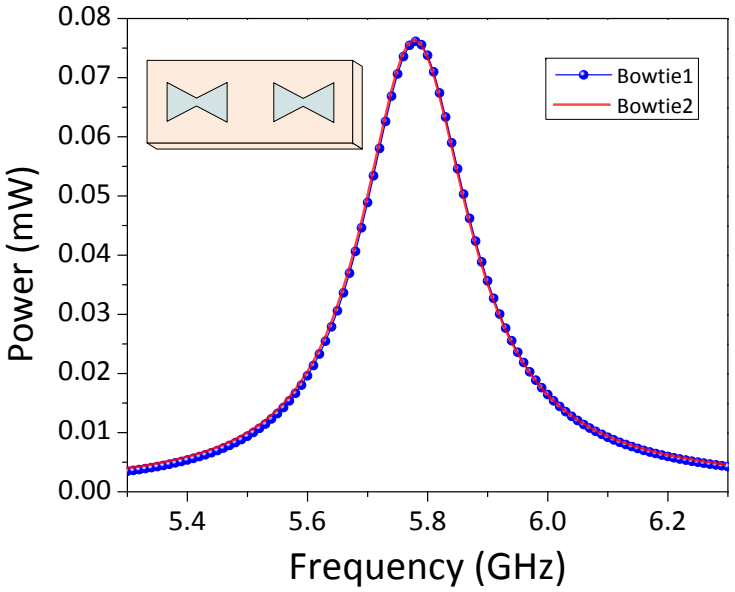

Figure 3.16: Power collected by the array of bow-tie antennas loaded by 50 Ω

wave (direction of propagation k perpendicular to the antenna plane (xy-plane) is shone, then, a power dissipated on the loaded resistance (50 Ω) for the two antennas are calculated. As illustrated in Figure 3.16, about 15% power efficiency is achieved, which is basically identical for the single bow-tie antenna, at the resonance frequency (5.8 GHz). With the same area of the previous array, 21 SRRs occupy this array and each resonator loaded by a 2.3k Ω, which is an optimal resistance as introduced before. Instead of calculating the power efficiency, the harvested power amount is computed since it is difficult to estimate the exact amount of incident power on each SRR, due to the mutual coupling among them. Figure 3.17 shows the potential power that can be collected by a single SRR if $1\,mW$ is shone over the array. Figure 3.17a represents the power collected by the first row in the array, while Figure 3.17b and Figure 3.17c represent the second and the third rows respectively.

However, the proposed structure can substantially provide more power harvesting efficiency compared to the antennas. Table 3.1 also summarizes the potential power that can be harvested for the two arrays. If a plane-wave carrying $1\,mW$ is applied on each array, the total amount of power collected at resonance frequency is $0.632\,mW$ and $0.153\,mW$ for SRRs and bow-tie arrays, respectively.

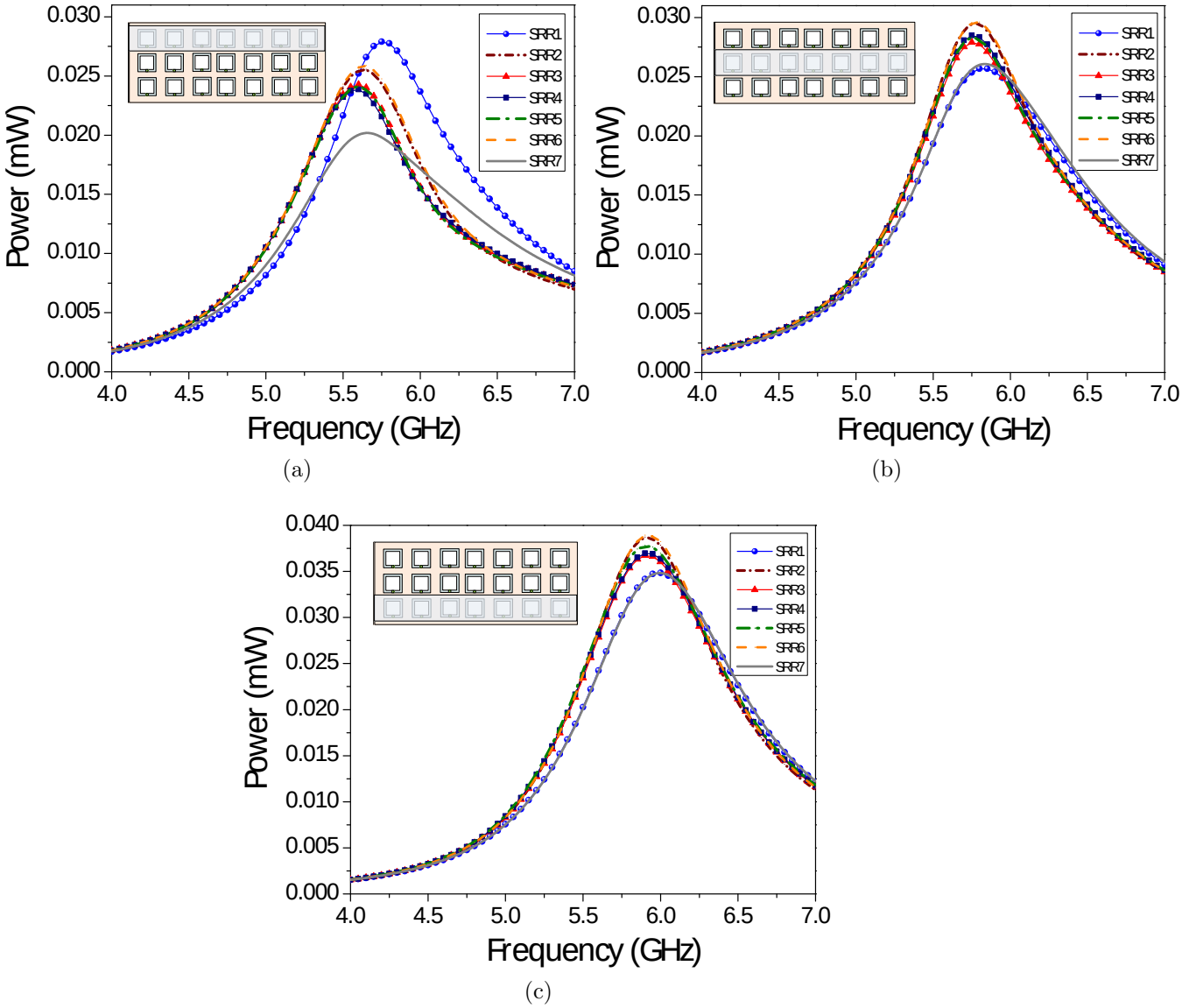

Figure 3.17: Power collected by the array of SRRs loaded by 2.3k Ω. (a) First row, (b) second row and (c) third row.

Table 3.1: The amount of power harvested for bow-tie and SRR arrays.

Array Type	Average Power(mW)	No. of Structures	Total Power(mW)
Bow-tie	0.0763	2	0.153
SRR	0.03	21	0.63

3.6 Conclusion

A comparison between a bow-tie antenna and SRR was made to show the efficiency improvement in power harvesting. SRR showed a substantial power efficiency improvement over that of the classical antenna. The bow-tie antenna achieved about 12% power efficiency, whereas the SRR achieved more than 37%. Moreover, a new efficiency definition was proposed to take into account the size reduction achieved by utilizing the electrically small resonators, which in turn, increases the total power efficiency. Therefore, two arrays having the same area, both designed at 5.8 GHz, produce $0.152\,mW$ and $0.597\,mW$, as power harvested for the bow-tie antennas and SRRs, respectively.

Chapter 4

Flower-Like Particles for Microwave Energy Harvesting

4.1 Introduction

It has been shown in Chapter 1 that different designs and configurations of rectennas have been suggested for energy harvesting to improve, in general, the RF-to-DC conversion efficiency [17, 23, 24, 60, 61]. Conventional antennas which act as a collecting source in a rectenna system generally have dimensions comparable to a half free-space wavelength. Moreover, the interaction behavior of antennas in arrays and restriction on the total antenna array footprint require certain antenna separation be maintained to avoid destructive coupling between the array elements [22, 25–27]. An empirical study showed that approximately 33% of harvesting efficiency from the source to the load was reported utilizing an array of 400 microstrip patch antennas [26].

In Chapter 3, the metamaterial elements were used to harvest electromagnetic energy in the microwaves regime by converting incident microwave energy into an AC signal. These metameterial elements showed the ability to collect microwave energy when a resistive load is inserted within the elements gap. In this chapter, electrically small particles whose largest dimension is less than $\lambda_o/10$ were proposed. In comparison to the previous work in Chapter 3 and [62], the proposed configuration allows higher suppression of dielectric loss, which in turn improves the harvesting efficiency. In addition, a microstrip line that serves as a power channeling mechanism is proposed and placed in the middle of the particles arrangement, whose gap opening is sharp allowing to coupling enhancement [63]. *The main roles of the proposed microstrip line are, first, to couple the energy from each*

excited circular SRR without the need for any physical connection between the elements, and second, to deliver the collected energy to a load, which is then consumed by a potential system. The proposed configuration achieves the highest energy harvesting efficiency when it is excited by a plane-wave perpendicular to the structure surface and with a linearly polarized electric field. *Emphasizing on not having a physical connection between the SRRs and microstrip line, this technique is to avoid intricate network matching issues for a large scale configurations and undesirable connection loss.*

4.2 Numerical Modeling

Two configurations proposed here, one with two and the other with four circular SRRs, consist of SRRs positioned symmetrically as shown in Figures 4.1a and 4.1b. The SRRs used here have much wider splits unlike the most common SRRs discussed in the literature. The proposed structures is intended not only to harvest the impinging electromagnetic waves, but also to channel the collected energy. A second proposed configuration (Figure 4.1b) is designed such that even- and odd-mode currents can be induced within the SRRs at the resonance frequency of the SRRs, leading to an improvement of harvesting efficiency as will be discussed below.

The flower-like array is etched on a one side of a Rogers substrate with a dielectric constant (ε_r) of 2.94, tangent loss (δ) of 0.0012, and thickness (h) of 1.524 mm, while the other side is left metalized. The array structure is simulated using ANSYS® HFSS™. The geometric dimensions of the whole element, including the microstrip line, are optimized such that its resonance frequency, at which maximum energy harvesting can occur, occurs at approximately 5.8 GHz. Optimization yields an outer radius $r_o = 2.5\,mm$, inner radius $r_i = 1.875\,mm$, the two openings of the gap $g_1 = 1.562\,mm$ and $g_2 = 2.4\,mm$, the microstrip length $l = 7\,mm$ and the microstrip width $w = 1.2\,mm$, as illustrated in Figure 4.1c.

Depending on the mechanism of harnessing the ambient energy either in the microwave or optical spectra, the proposed structure should generally enhance the interaction between the incident wave and the harvester. The configuration proposed here collects the incident microwave energy and channels it to the metallic traces (here, made of copper) rather than absorbing the energy in the dielectric substrate. The two configurations shown in Figure 4.1 were first examined numerically inside a radiation box filled with air while the array was positioned at the center of the box. A plane wave with different incidence angles is shone at the two arrays. Since this structure aims to collect the incident power and channel it through the transmission line, a resistive load is needed to measure the received power. This structure resembles the case of a full system incorporating a harvester and a

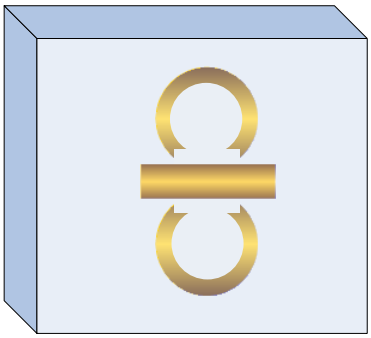

(a)

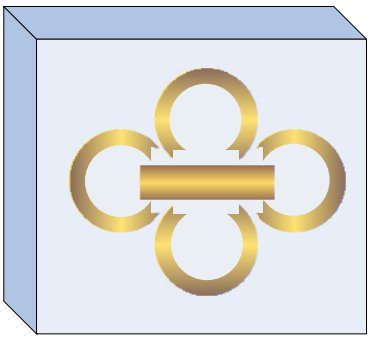

(b)

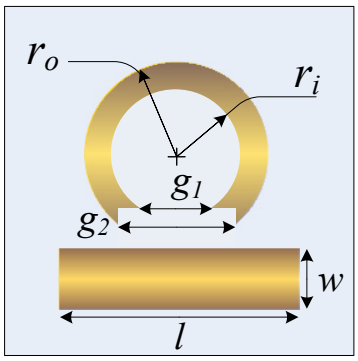

(c)

Figure 4.1: Two configurations of the proposed energy collector arrays. (a) array with two, (b) four resonators and (c) the dimensions of the circular split-ring resonator and microstrip line

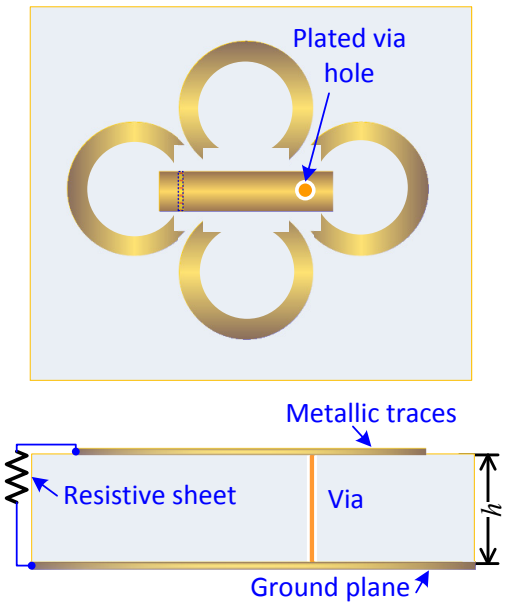

Figure 4.2: Layout of the flower-like energy harvester, top and side view.

rectification circuit. At one terminal of the microstrip line, a resistive sheet is connected to the ground plane, while the other terminal is shorted to the ground, as shown in Figure 4.2. The resistive sheet value was varied until the highest power efficiency was achieved (while keeping the frequency fixed at resonance). The optimal resistance was found to be 12k Ω. Two ports are realized by defining two sheets on the left and right of the examined structure. Then, the scattering parameters were extracted from the calculated electric field intensities (E_y) at the two ports (two defined sheets), where the extraction implemented here is based on the method described in [64–66].

4.3 Mechanism of the Energy Harvester

Figure 4.3 shows the volume current distributions in the dielectric substrate for the two harvesters shown in Figures 4.1a and 4.1b. As shown in the left side of Figure 4.3, the array with only two resonators results in higher dielectric losses. The interpretation of this increment in dielectric loss between the two structures can be explained by Figure 4.4, where at resonance the two resonators on the left and right sides of the microstrip line create currents at the edges of their gaps that oppose the out-of-phase currents induced by the other two resonators. The microstrip line setting in the middle arrangement of the

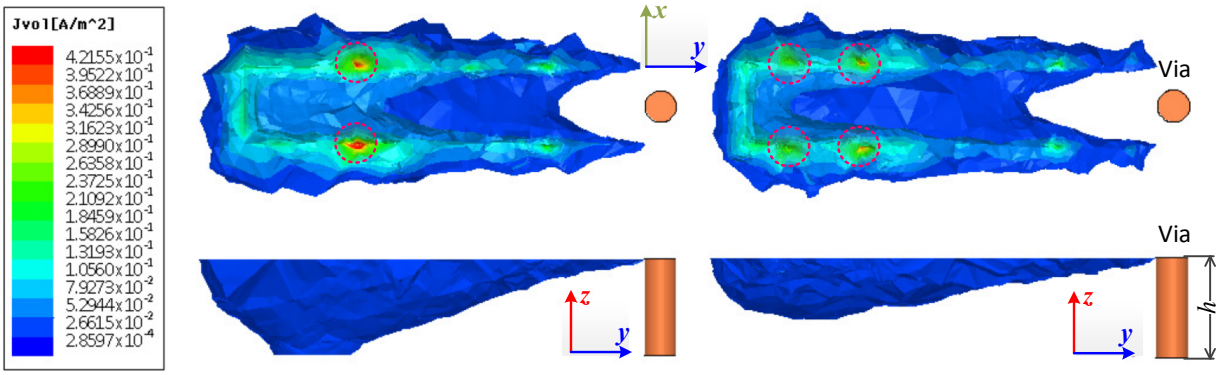

Figure 4.3: Simulation results for the volume current distributions (dielectric losses) in the dielectric substrate at resonance for the flower-like energy harvester with (left) two circular SRRs (top and side views), and (right) four circular SRRs (top and side views). The losses are nil except beneath the transmission line as shown above, and the dotted circles represent the contact spots of the sharp gap opening.

array does the following jobs: first, it couples the energy from each excited resonator by a linearly polarized incident field and second, it channels the collected power to the resistive sheet. Therefore, it is of a high importance in terms of power harvesting to increase the current flow through the microstrip line. *Eliminating the out-of-phase currents by adding the two lateral resonators improves current flow on the microstrip line (the channeling route) and yields more power efficiency and less dielectric loss.*

Figures 4.5 and 4.6 show the scattering parameters for the arrays with two and four circular resonators, respectively. By considering the cases without resistive loads and at normal incidence (Figures 4.5b and 4.6b), a one dB difference in transmission and reflection coefficients between the two arrays can be observed. This implies that more than 11% of confinement occurs in the four-array structure compared with the two resonators case. After loading the two structures with a 12k Ω resistive sheet at one port as discussed above, a slight shift in the resonance frequency appears; however, the array with four resonators achieves better power confinement than the array with two resonators, even with the resistive loading. Both S_{21} and S_{11} have dips at resonance frequency as presented in Figures 4.5b and 4.6b; this indicates that *low reflection and low transmission occur at the same time, resulting in energy confinement in the harvester.*

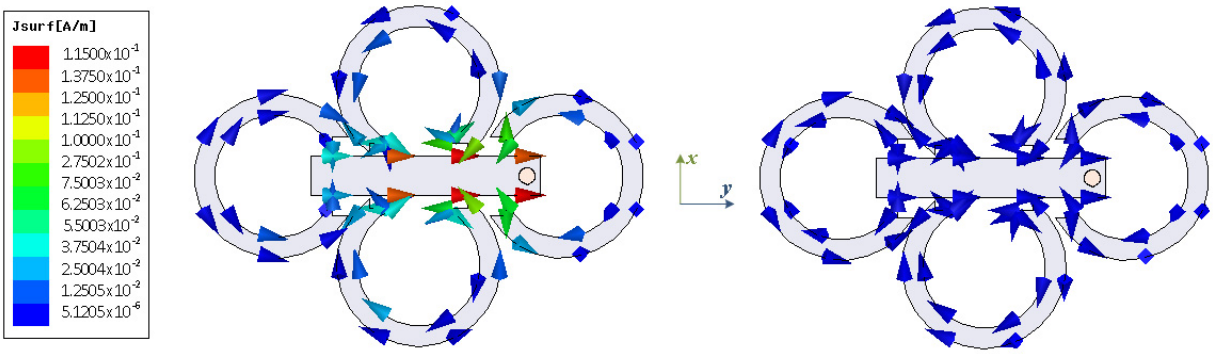

Figure 4.4: Simulated current distributions of the flower-like energy harvester with four circular SRRs at resonance (left) and off resonance (right) with the electric field (**E**) polarized in y direction. The arrows indicate to the current direction.

4.4 Simulation and Experimental Results

The fabricated flower-like array was etched on RT/duroid 6002 board material with a dielectric constant (ε_r) of 2.94 and thickness (h) of 1.524 mm. The fabricated structure is shown in Figure 4.7. To measure the harvested power, a surface mount resistor with an optimal value of 12k Ω is placed on the backside of the array where it connects one end of the microstrip line with the ground plane. The picture in Figure 4.8 shows the setup for measuring the voltage across the mounted resistor. An Agilent Infiniium 13 GHz oscilloscope and Agilent PSG vector signal generator are used in this measurement. The signal generator is connected to a standard 18 dBi gain horn antenna at 5.8 GHz. The array was excited by the horn antenna with 19 dBm input power. The array was placed at a distance (r) of 30 cm from the horn antenna, such that the array was centered on a line perpendicular to the plane of the horn antenna. Then, the voltage across the surface mount resistor at 5.67 GHz was measured using a single-ended probe and was 121 mV, while the available voltage at the front of the harvester was 193 mV.

ANSYS® HFSS™ numerical full-wave simulation tool is used to compute the power harvesting efficiencies for both arrays presented in Figures 4.1a and 4.1b, by applying the following formula:

$$\eta = \frac{P_{received}}{P_{incident}} \tag{4.1}$$

where $P_{incident}$ is the total microwave power incident on the footprint of the array, and $P_{received}$ is the microwave power received by the array (dissipated by the resistive load at one end of the microstrip line) [67]. Figure 4.9 depicts the harvesting power efficiencies of

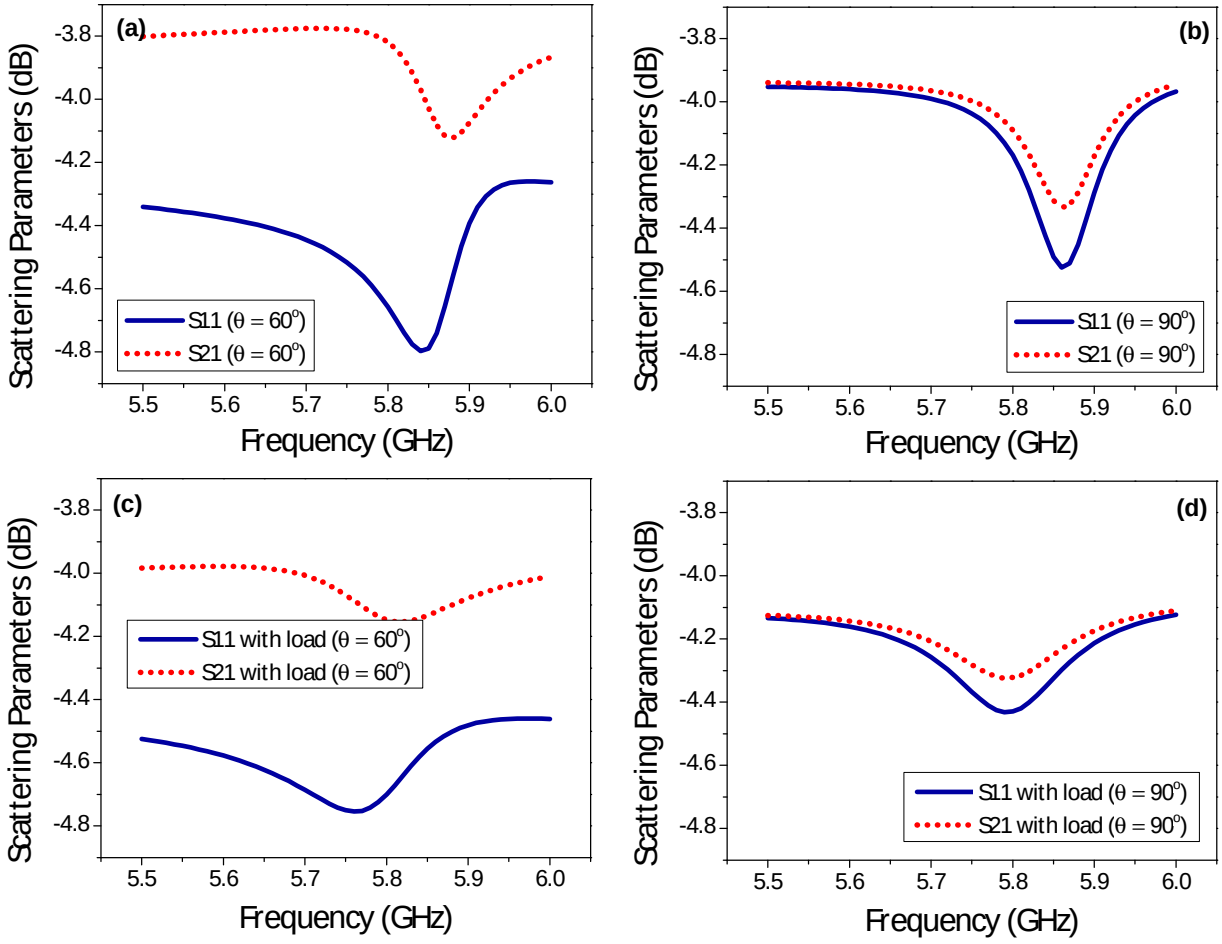

Figure 4.5: Simulated scattering parameters for the the flower-like energy harvester with *two circular resonators*. (a) without resistive load and at incidence angle $\theta = 60^o$, (b) without resistive load and at incidence angle $\theta = 90^o$, (c) with resistive load and at incidence angle $\theta = 60^o$ and (d) with resistive load and at incidence angle $\theta = 90^o$.

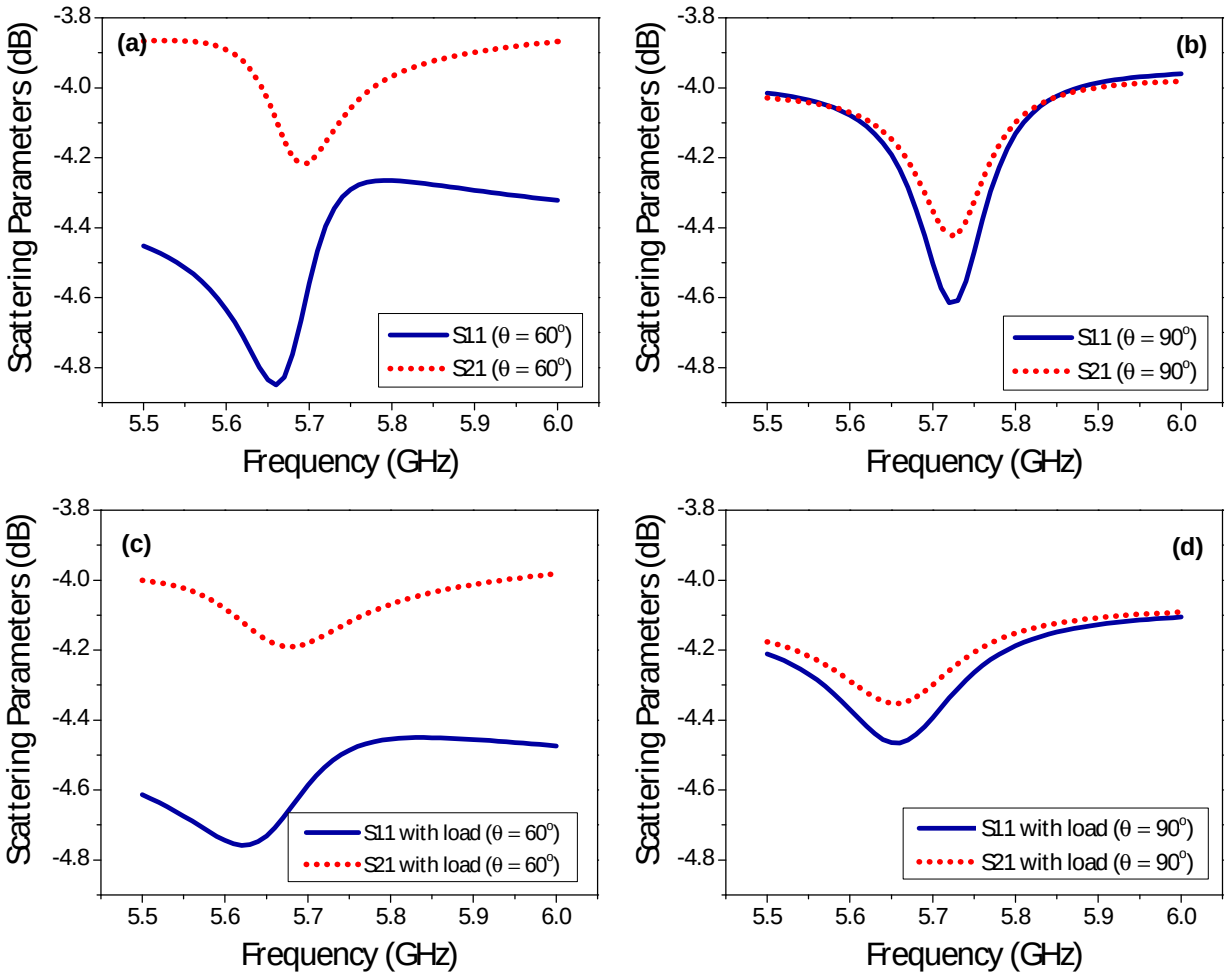

Figure 4.6: Simulated scattering parameters for the the flower-like energy harvester with *four circular resonators*. (a) without resistive load and at incidence angle $\theta = 60^o$, (b) without resistive load and at incidence angle $\theta = 90^o$, (c) with resistive load and at incidence angle $\theta = 60^o$ and (d) with resistive load and at incidence angle $\theta = 90^o$.

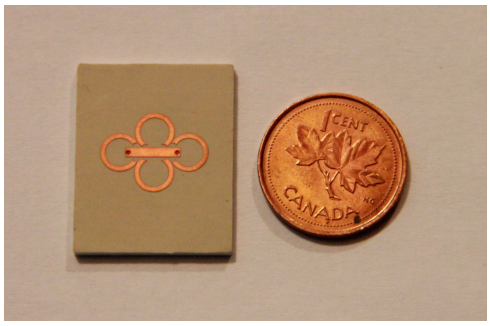

Figure 4.7: Fabricated flower-like array on RT/duroid 6002 board material.

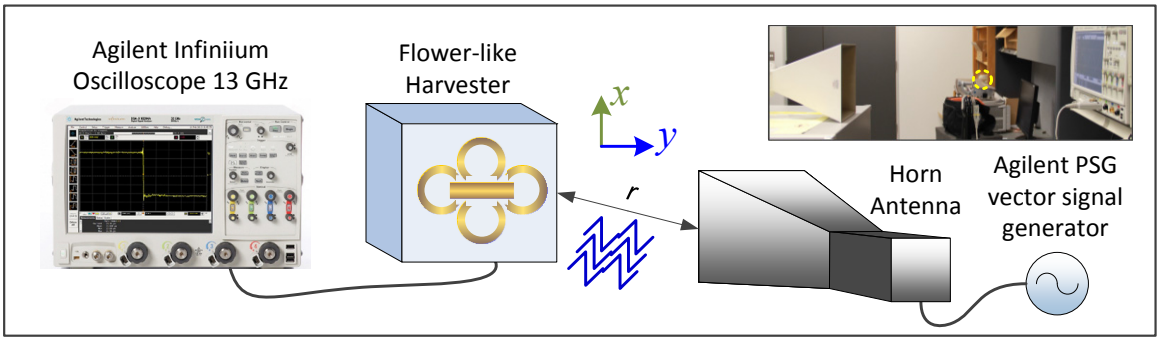

Figure 4.8: Lateral view of the experimental setup to measure the receipted voltage across the resistive load.

the two arrays at different incidence angles (θ). For the array with four circular SRRs, the highest efficiency, of approximately 44%, occurs at the resonance frequency with a perpendicular incidence angle $\theta = 90^o$ and a magnetic field horizontal to the inclusion's surface. Such change in excitation condition (horizontal magnetic field) is attributed to presence of the transmission line since the current distribution over the transmission (microstrip) line as presented earlier in Figure 4.4 is dominant. Although the second plot (Figure 4.9b) presents the same view as Figure 4.9a, except for a slight frequency shift, the power harvesting efficiency of the array with two SRRs is less than that of the array with four SRRs by approximately 6%. This degradation is related to the dielectric loss shown in Figure 4.3. Moreover, a shift by 100 MHz in resonance frequency occurs when two of the SRRs are removed.

The ability of the flower-like energy harvester with four circular SRRs has been demonstrated to harvest and channel the incident electromagnetic waves, numerically and experimentally. However, for practical scenario, multiple arrays are needed to provide adequate power for a potential system. Therefore, a set of 3×3 flower-like energy harvester array (see Figure 4.10), each array is composed of four circular SRRs and a transmission line, has been simulated to calculate the overall harvesting efficiency. The horizontal and vertical spacing between any two adjacent arrays are $s = 0.8\,mm$ and $v = 0.6\,mm$, respectively, where the two distances, s and v, represent less than $\lambda_o/67$ and $\lambda_o/89$, respectively. More than 55% power harvesting efficiency at 5.56 GHz is achieved with the configuration of 3×3 array as depicted in Figure 4.11. This finding indicates efficiency improvement is possible by increasing the footprint area and placing the elements in a close proximity. *Taking advantage of the constructive coupling among the electrically small particles, an enhancement of 11% power harvesting efficiency is realized by utilizing closely-spaced multiple arrays compared with only one array consisting of four SRRs.*

4.5 Conclusion

An array composed of electrically small resonators to harvest electromagnetic energy in the microwave regime was designed and fabricated. The proposed configuration creates in- and out-of-phase currents, which in turn increases the current flow on the microstrip line and concurrently limits the dielectric loss in the substrate. Approximately 44% at 5.67 GHz and 38% at 5.77 GHz power harvesting efficiencies were achieved with the four and two circular SRRs arrays, respectively, at a normal incidence angle. The concept of power harvesting with the proposed configuration was also validated by measuring the voltage across the resistive load. Moreover, it was shown that positioning any two elements

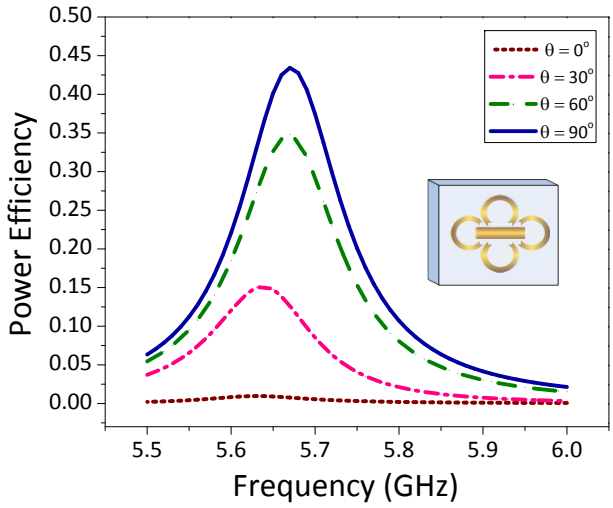

(a)

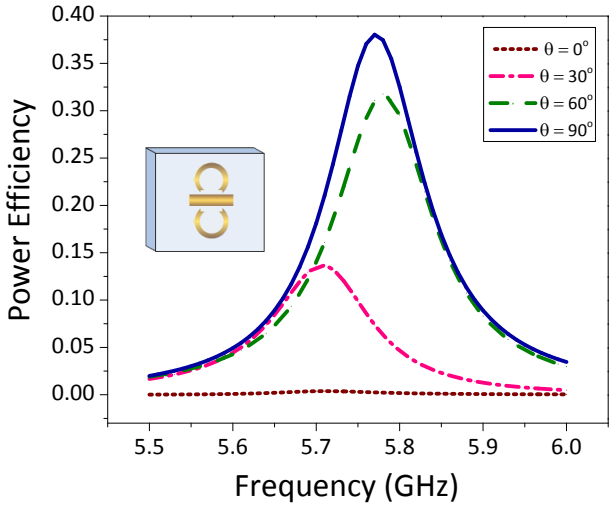

(b)

Figure 4.9: Calculated power efficiencies of the flower-like energy harvesters loaded by 12k Ω at different incidence angles. (a) array with four and (b) two circular resonators

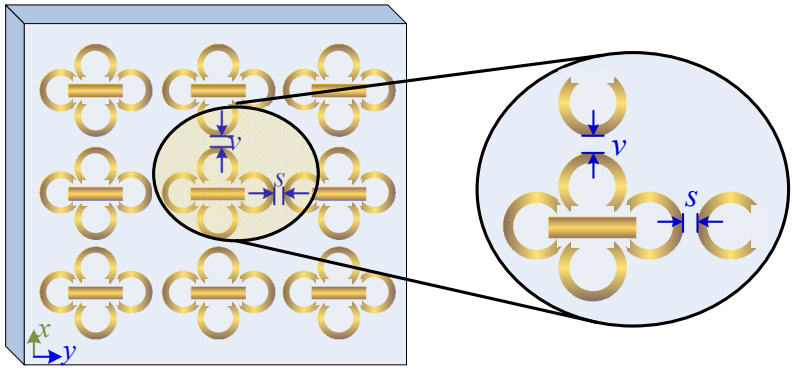

Figure 4.10: Top view of 3×3 flower-like energy harvester with four circular SRRs spaced at $s = 0.8\,mm$ and $v = 0.6\,mm$.

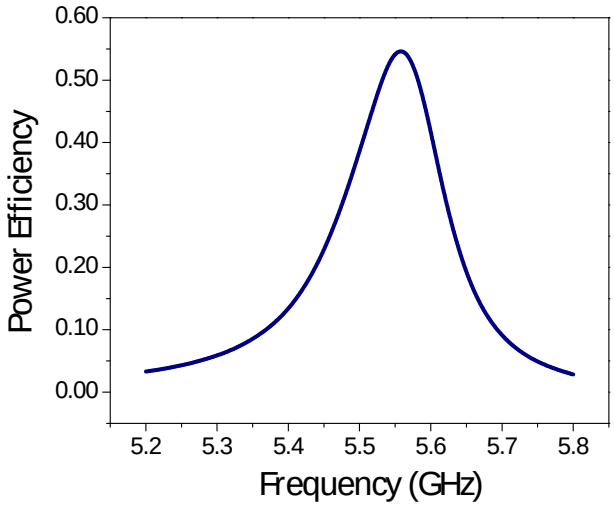

Figure 4.11: The calculated power efficiency of 3×3 flower-like energy harvester with four circular SRRs excited by a normal incident plane wave, and each array is loaded by $12\mathrm{k}\,\Omega$.

of the proposed configuration in a closely-adjacent manner, contributes to improving the overall harvesting efficiency. In the next chapter, the concept of using metamaterial for electromagnetic energy harvesting is applied to harvest infrared energy where an ensemble of six square SRRs and a microstrip transmission line are shown to convert electromagnetic waves to AC current with an efficiency of more than 80%.

Chapter 5

Power Harvesting in the Infrared Regime

5.1 Introduction

The Earth receives more than 100 petawatts (100×10^{15} watts) of solar power that cover different spectrums ranging from infrared to visible waves [68]. Around the clock, a massive amount of that power penetrates the atmosphere in forms of infrared energy. More specifically, electromagnetic radiation of over one kilowatt per square meter reaches sea level, approximately half of which is infrared radiation. As illustrated in Figure 5.1, infrared spectrum that extends from 1 mm to 1 μm is located between the radio and visible regimes. The infrared region is zoomed-in, showing different windows based on the atmospheric transmittance. At 10 μm wavelength, the atmospheric transmittancy reaches approximately 80%, which means a lot of infrared radiation reaches to earth at sea level. This part of the solar spectrum has not been exploited well, since the photovoltaic technology is only able to harvest the visible sunlight. Besides that, most of the current technologies to harness infrared irradiation are based on antenna concept as discussed in Chapter 2. Indeed, maximizing power efficiency in electromagnetic energy harvesting systems and utilizing all transducer footprint areas are critical objectives, since the overall footprint of the harvesting system contributes directly to the cost and efficiency calculations.

In this chapter, the concept of using electrically small resonators to harvest microwaves energy is extended to the infrared frequency regime. While the initial conjecture diminished enthusiasm for such extension due to the dispersion behavior of metals at higher frequencies, the achieved results are encouraging. Secondly, a mechanism by which the energy

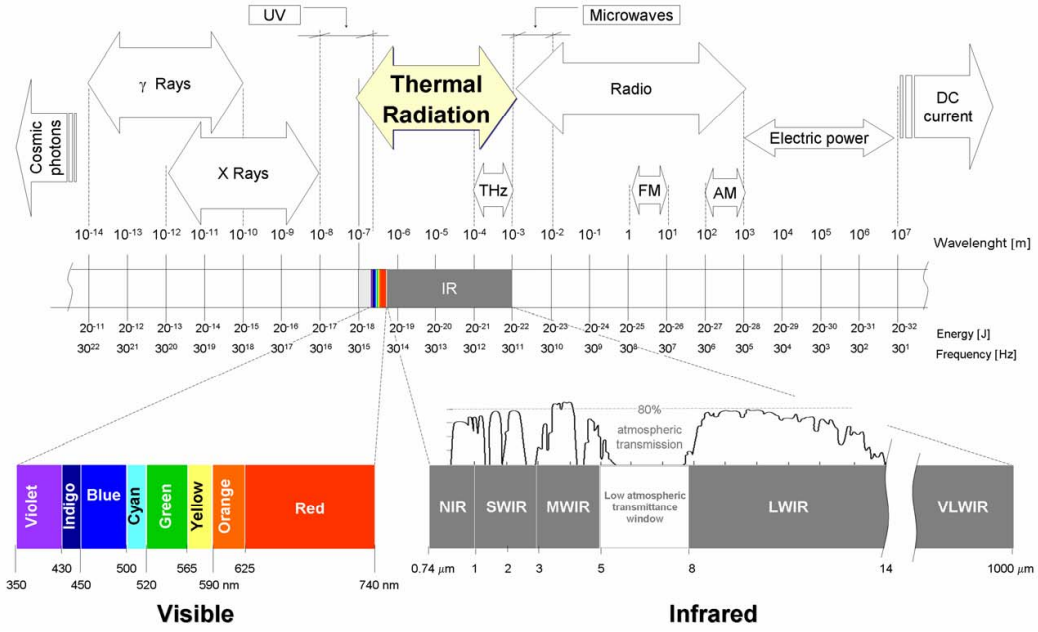

Figure 5.1: The electromagnetic spectrum with detailed infrared bands [9].

collected by an array of electrically small resonators is channeled through a transmission line, is proposed. Fabrication using nano-technology tools followed by a THz time-domain spectroscopy (THZ-TDS) measurement, are conducted to validate the numerical findings experimentally.

5.2 Split Ring Resonators (SRRs) for Energy Harvesting

To test the SRR ability for energy harvesting in the far-infrared regime, the SRR is modeled such that dispersion of its material properties (metal and substrate) correspond to the target frequency of interest of approximately 0.5 THz. Although many dielectric materials are frequency dependent, some of which have a relatively constant permittivity over a wide range of frequencies extending to the far-infrared spectrum. Silicon (S_i) substrate with dielectric constant (ε_r) of 11.9, posses such property. The Drude model is selected to characterize the dispersion effect of the dielectric constant of Silver. The Drude model is used in this design due to its accurate parametrization of the dielectric function in the far

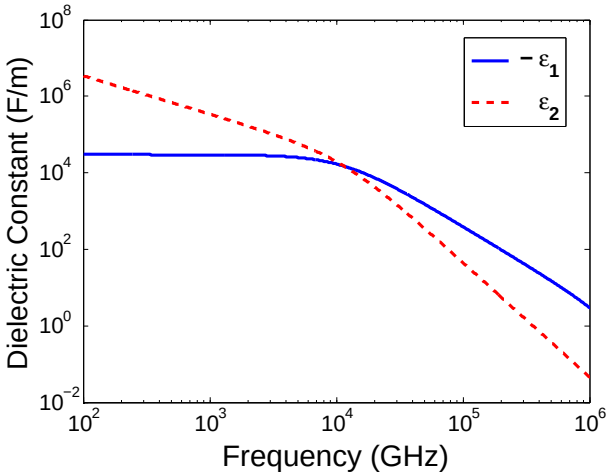

Figure 5.2: The real and imaginary dielectric constants of Silver (Ag)

infrared for Silver and other metals [69].

The complex dielectric function (ε_c) of the Drude model is expressed as [70, 71]:

$$\varepsilon_c = \varepsilon_\infty - \frac{\omega_p^2}{\omega^2 + i\omega\omega_\tau} \tag{5.1}$$

where ε_∞ is the high frequency dielectric constant, ω_p is the plasma frequency and ω_τ is the damping frequency, and these two frequencies are expressed in cm^{-1} according to centimetre-gram-second (CGS) system. The plasma frequency ω_p is defined as [72]:

$$\omega_p = \frac{1}{2\pi c}\left(\frac{4\pi N e^2}{m^* \varepsilon_\infty}\right)^{1/2} \tag{5.2}$$

where e is the electron charge, N is the free electron density and m^* is the effective mass of the electron. The damping frequency ω_τ is:

$$\omega_\tau = \frac{1}{2\pi c\tau} \tag{5.3}$$

where c is the speed of light and τ is the electron lifetime in seconds. Silver is the metal of choice for this design, due to its low absorption losses compared to other metals [15]. The real and imaginary dielectric constants of Silver extending from millimeter until the ultraviolet waves are both illustrated in Figure 5.2.

The commercial full-wave simulation tool ANSYS® HFSS™ [73], which is based on the finite-element method is used throughout this work. In order to numerically examine the

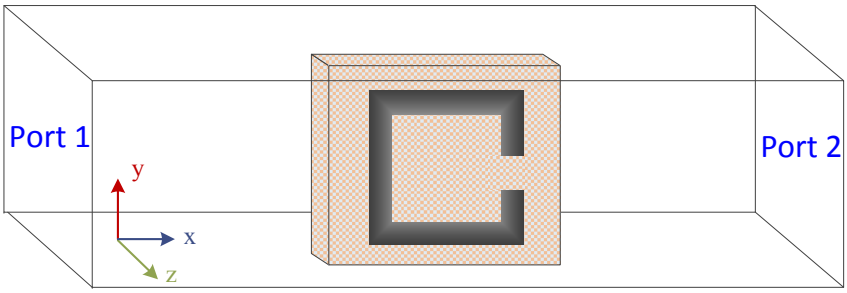

Figure 5.3: The numerical waveguide model with a single SRR at the center. The boundaries in the xy plane are assigned as perfect magnetic conductor and boundaries in the xz plane are perfect electric conductor

behavior of the SRR operating in the infrared regime, a waveguide with the SRR centered in the waveguide, as shown in Figure 5.3, is used to calculate the amount of energy that is transmitted or reflected from the SRR element; thus, the difference between the transmitted and reflected energies represents the absorbed energy by the SRR. The model is excited by two wave ports and appropriate boundary conditions are applied to force the magnetic field to be perpendicular to the inclusion's surface. The assigned boundary conditions resemble a vertical plane wave shining on the inclusion. This numerical experiment is intended primarily to verify whether or not the SRR has the potential to harvest energy. The geometric dimensions of the SRR are heuristically optimized to obtain its resonance frequency at around 500 GHz. The resulting design parameters are (see Figure 5.4a): arm length $L = 40\,\mu m$, arm width $W = 10\,\mu m$ and gap width $g = 10\,\mu m$. This metallic inclusion is etched on a Silicon (S_i) slab with a dielectric constant ($\varepsilon_r = 11.9$) and thickness of ($h = 50\,\mu m$). Figure 5.5 represents the reflection and transmission coefficients S_{11} and S_{21} of the SRR, which resonates at 495 GHz. By applying the unitary matrix equation of the two-port waveguide depicted in Figure 5.3 at 495 GHz.:

$$|S_{11}|^2 + |S_{21}|^2 = \delta \tag{5.4}$$

The S_{11} and S_{21} parameters were extracted according to the procedure outlined in [64–66], with $S_{11} = 0.94$ and $S_{21} = 0.15$. This gives $\delta = 0.9$, implying that the resonator exhibits almost full reflection with very little power transferred through at resonance. This behavior is consistent with previous works [74] where a medium composed of an array of SRRs behaves as a full reflector. The fact that δ is not unity indicates losses in the metal and substrate and possibly scattering effects. By plotting the electric field intensity at the resonance frequency in the y direction (E_y) over the resonator surface, one can observe that high E_y is concentrated in the SRR gap as depicted in Figure 5.7.

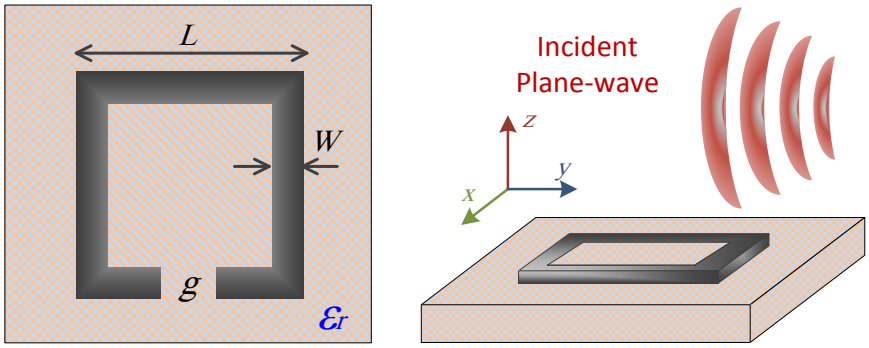

(a) (b)

Figure 5.4: Split ring resonator unit cell with its dimensions. (a) top view and (b) perspective view. (note that schematic is not drawn to scale)

Based on the above numerical analysis, loading an optimum impedance within the SRR gap would most probably facilitate maximum power absorbtion by the metallic inclusion. To this end, a resistive sheet was placed across the SRR gap and its resistance value was swept over a wide range of values to determine the value at which maximum power efficiency occurs. However, only resistive values from 1k to 3k Ω are presented for illustration purpose. It is found that a resistance of 2k Ω yields maximum power absorption in the gap. The scattering parameters S_{11} and S_{21} are then computed again to show the effect of placing the resistive load.

As illustrated in Figure 5.6, after applying the resistive load, the scattering parameters change significantly. In fact the new values are $S_{11} = 0.78$ and $S_{21} = 0.46$, yielding $\delta = 0.82$, thus indicating additional energy being absorbed within the SRR in comparison to the case without the load.

Having validated the ability of the SRR to absorb part of the electromagnetic energy of the incident wave, we test the SRR in a stand-alone arrangement as shown in Figure 5.4b, where a plane wave is incident in free space and propagating in a direction parallel to the plane of the SRR. With the aim of calculating energy harvesting efficiency of the SRR, a footprint in square meters occupied by the SRR system is defined. Therefore, the harvester system efficiency can be calculated as:

$$\eta = \frac{P_{received}}{P_{incident}} \tag{5.5}$$

where $P_{incident}$ is the total infrared power that strikes the defined footprint (or alternatively

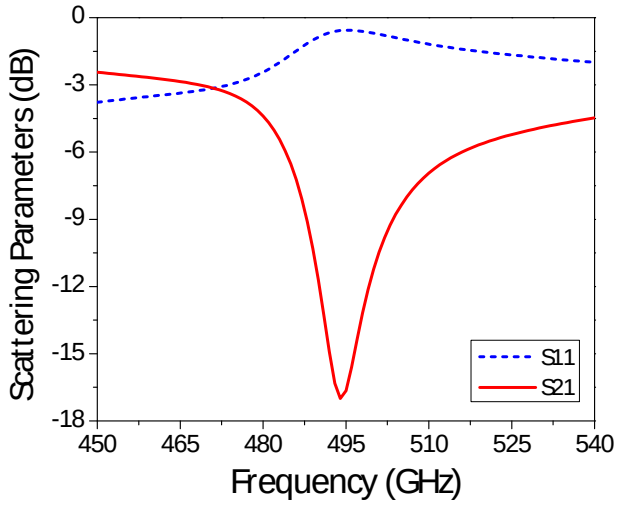

Figure 5.5: Simulated scattering parameters of the SRR without resistive load

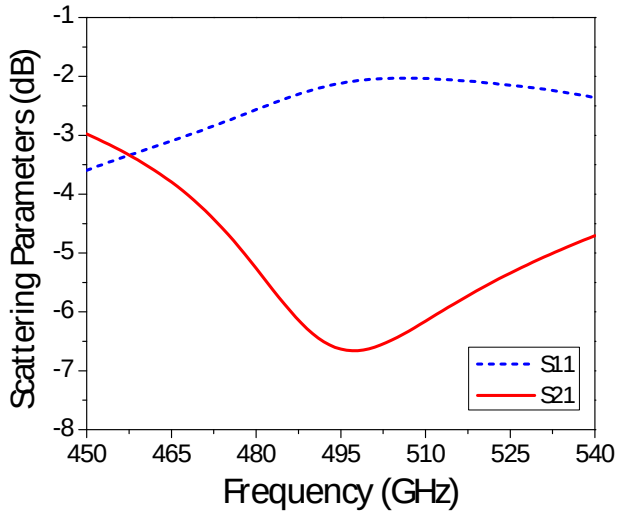

Figure 5.6: Simulated scattering parameters of the SRR loaded with a resistive load of $2\mathrm{k}\,\Omega$

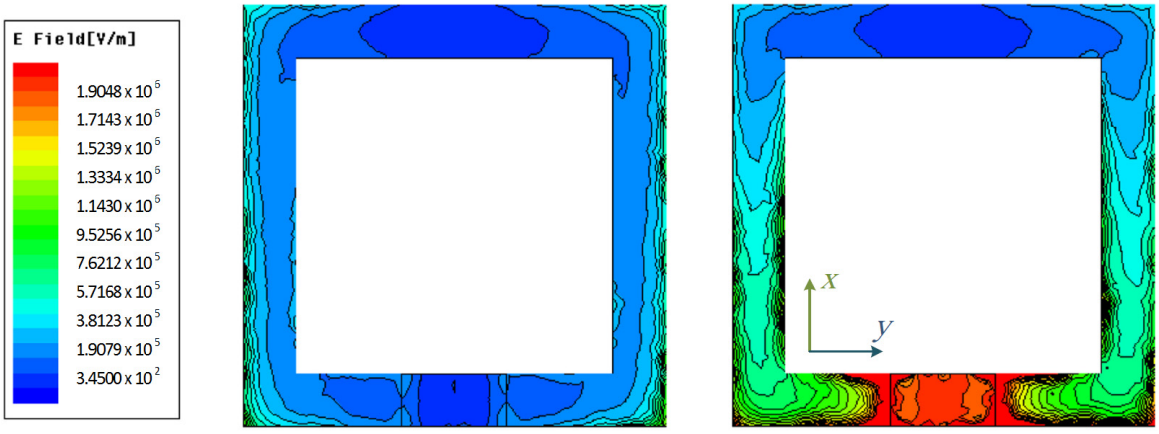

Figure 5.7: Simulation results for the electric field intensity in y direction (E_y) of the SRR (left) out of resonance region, (right) at the resonance frequency with the magnetic field ($\mathbf{H}$) perpendicular to the inclusion's surface

that is available at the defined footprint), and $P_{received}$ is the maximum infrared power received by the SRR (dissipated by the SRR resistive load). Figure 5.8 shows the harvesting power efficiency by using the SRR loaded by different resistance values. The highest efficiency of approximately 30% occurs at the resonance frequency.

5.3 Channelling Energy for Array Structures

To supply practical systems with feasible amount of power, an array composed of multiple harvesters is needed. Here, we experiment with two types of 3×3 arrays. The first is a periodic array with symmetry about a vertical axis (in the x direction) positioned at the center of the array (henceforth referred to as the symmetric array), whereas for the second array, each two adjacent elements are symmetric with respect to a y-directed dividing line between them (henceforth referred to as the asymmetric array). The two arrays are shown in Figure 5.9. The arrays are designed using a silicon substrate with the same thicknesses and geometric features used for the single SRR. Each resonator is loaded with a $2\,\mathrm{k}\,\Omega$ resistor, which was found to be the optimal resistance for the single SRR. Figure 5.10 shows the harvested power efficiencies achieved by the two arrays.

The first observation we make is that the array of SRR cells results in higher efficiency (per unit area) than a single SRR cell. This is due to capacitive and inductive mutual coupling between adjacent cells that even affects the angle of incidence at which optimal

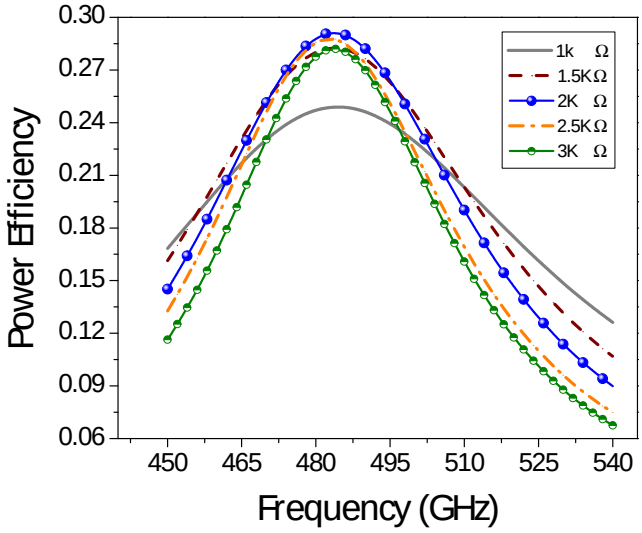

Figure 5.8: Calculated power efficiency of the SRR loaded by different resistances

energy absorption is achieved. The second observation we make is that the asymmetric SRR array resulted in significantly higher efficiency than in the case of the symmetric one. For better understanding of the variance in efficiency between the two arrays, in Figure 5.11 we show the simulated current distributions at the resonance frequencies of the 3×3 symmetric and asymmetric SRR arrays. *For the asymmetric array, most of the current circulating through each SRR is in-phase with the adjacent SRR's current. The adjacent currents induce a stronger electric field across the SRR gap, which in turn increases the absorbed power across this gap. On the other hand, for the symmetric array, most of the currents flowing through each SRRs are out-of-phase with the closely spaced SRR current, resulting in a less mutual coupling compared to the asymmetric array.*

Next, a routing mechanism to channel the collected energy from each individual harvester in an SRR array environment is proposed. Although collectors can be schemed in unlimited ways, many challenges, such as footprint size, losses and power matching complexities arise. The structure proposed here utilizing a Silicon substrate with thickness of $h = 50\,\mu m$ and dielectric constant of $\varepsilon_r = 11.9$ is intended for operation over the 400-480 GHz frequency range. Figure 5.12 depicts the layout of the proposed array structure. A microstrip transmission line that is positioned as shown works to couple and route the energy to a resistive load placed at one end of the line.

The array was tested using radiation boundary conditions excited with a plane wave to mimic a real environment. Figures 5.13 and 5.14 represent the scattering parameters of the

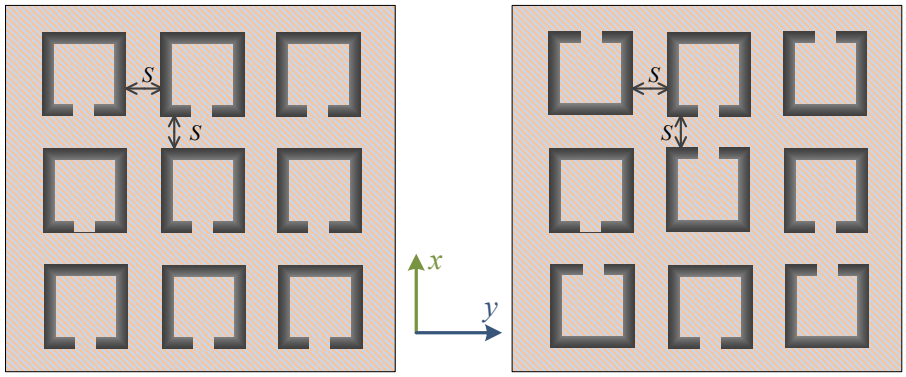

Figure 5.9: Top view of 3×3 symmetric (left) and asymmetric (right) SRR arrays with a separation $s = 20\,\mu m$

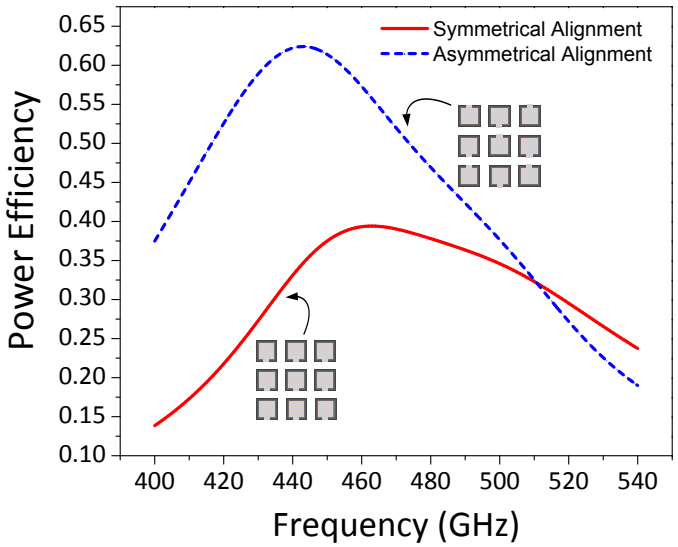

Figure 5.10: Power efficiencies of the 3×3 symmetric and asymmetric SRR arrays loaded by a $2\mathrm{k}\,\Omega$

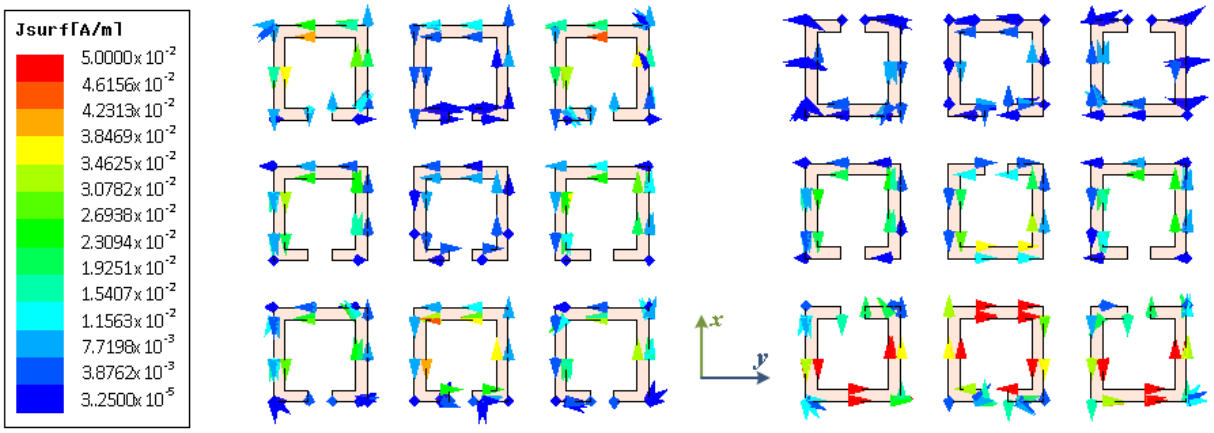

Figure 5.11: Simulated current distributions at resonance frequencies of the 3×3 symmetric (left) and asymmetric (right) SRR arrays with the electric field ($\mathbf{E}$) polarized in y direction. The arrows indicate to the current direction

array structure before and after placing a $100\,\Omega$ resistive sheet. The value of the resistive sheet is chosen to achieve maximum power transfer from the incident wave to the resistive load. The resistive sheet connects one terminal of the microstrip line to the ground plane. For optimal matching between the load and microstrip line, the characteristic impedance of the line was chosen to be equal to the load.

The scattering parameters corresponding to the array with and without the resistive load placed at the end of the microstrip transmission lines are shown in Figures 5.13 and 5.14, respectively, showing that 30% of the incident power is reflected. Notice that the power passing through the array accounts for more than 50% of the transmitted waves at 408 GHz. These numerical experiments indicate that the array harvester can act as a power absorber or a collector. After loading the array with 100Ω resistance connected at one terminal of the microstrip line, and by substituting the scattering parameters from Figure 5.14 in equation 5.4 and at frequency 408 GHz., leads to $S_{11} = 0.116$ and $S_{21} = 0.462$ with $\delta = 0.227$.

Under the previous simulation settings, the magnitude of the electric field (E_y) on the metallic inclusions of the resonators and transmission line is depicted in Figure 5.15. This simulation shows that the front parts of the SRRs, in which the SRRs gaps are placed, contribute remarkably to both collecting and coupling the energy to the microstrip line. One can perceive that the electric field magnitude is quite low within the the microstrip line, which is attributed to non-perfect coupling between the vis-à-vis SRRs and the channeling

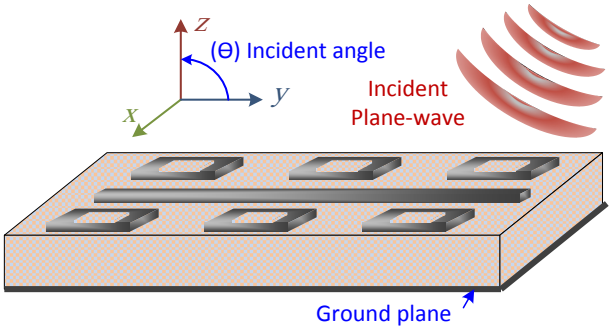

(a)

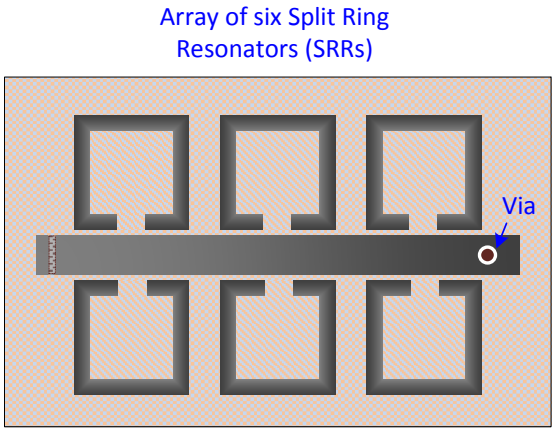

(b)

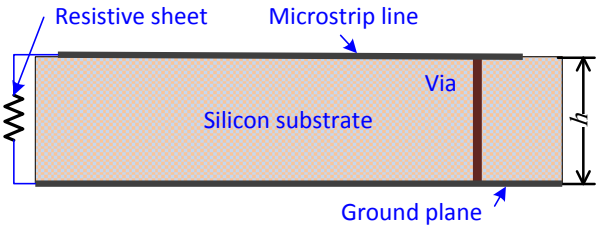

(c)

Figure 5.12: Schematic of the far-infrared array energy harvester.(a) perspective view (b) top view and (c) side view. (note that schematic is not drawn to scale)

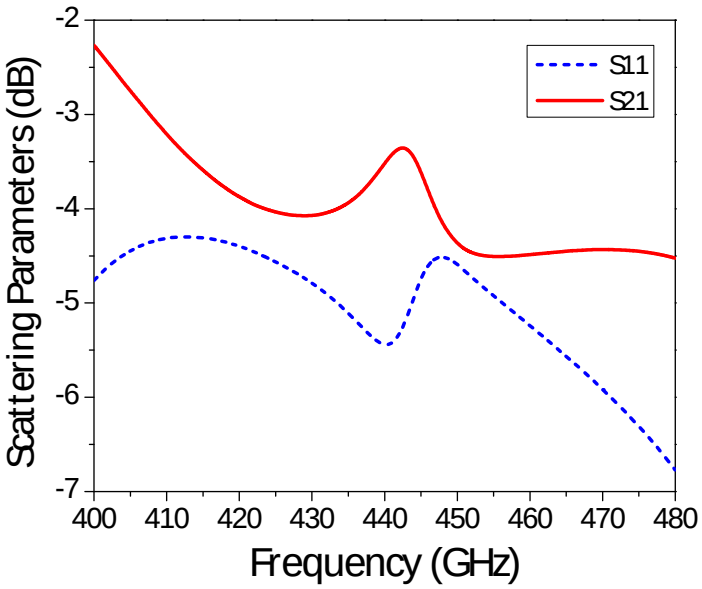

Figure 5.13: Simulated scattering parameters for the far-infrared array without resistive load

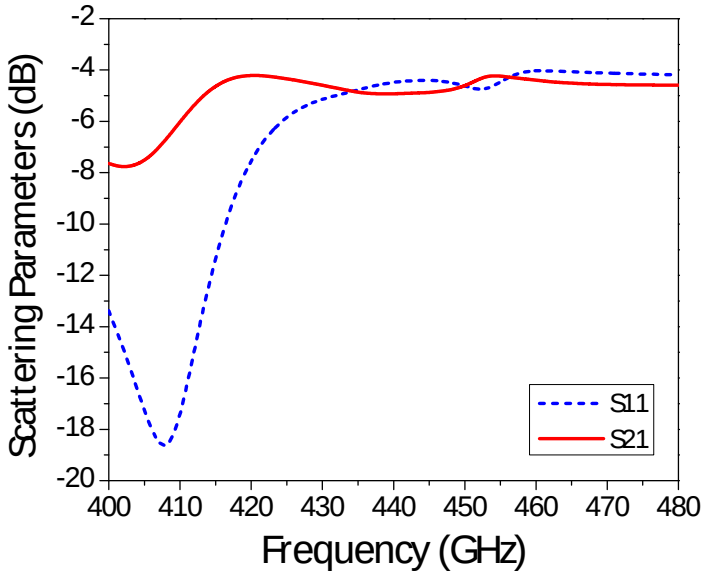

Figure 5.14: Simulated scattering parameters for the far-infrared array with resistive load

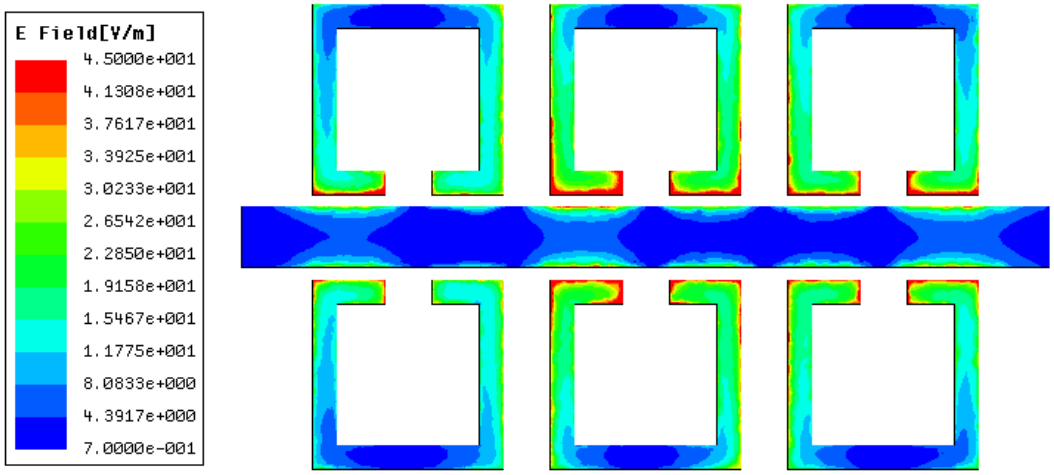

Figure 5.15: Simulation results of the electric field magnitude in y direction (E_y) and on top of the metallic inclusions of the proposed harvester.

route. However, more advancement on the coupling mechanism is proposed in Chapters 4 and 6.

The power efficiency of the array is calculated by shining a plane wave at different incidence angles θ on a stand-alone array structure. Figure 5.16 shows that the highest power efficiency of approximately 80% occurs when the frequency is close to 410 GHz at an incidence angle $\theta = 60^o$ (see Figure 5.12a for the definition of θ). Approximately 45% and 20% harvesting efficiencies are achieved at the resonance frequency with incidence angles of $\theta = 30^o$ and $\theta = 0^o$, respectively. In the SRR-only array case, the highest efficiency demanded that the incident magnetic field be perpendicular to the structure surface to maximize the SRR's magnetic dipole resonance. However, in this particular study, we introduced the microstrip transmission line to channel the energy. The interaction of an incident plane wave with the microstrip transmission line, in the presence of the SRR array, is complex, however, if the transmission line mode is excited on the line, then high edge currents on the line can exist giving rise to enhanced magnetic field within the SRRs. While the microstrip line was used in this work, it is conceivable that optimum energy harvesting can be achieved using other waveguiding structures.

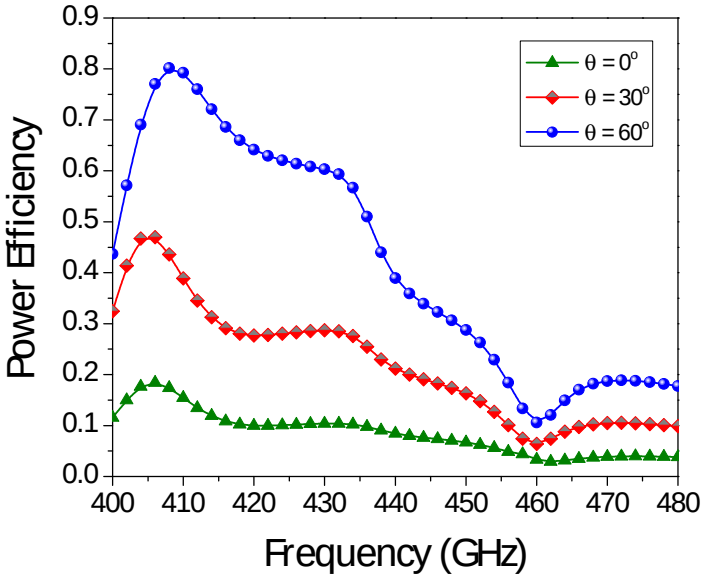

Figure 5.16: Calculated power efficiency of the array loaded by 100 Ω at different incident angles θ

5.4 Fabrication Results

Moving a step further to fabrication processes will definitely bring some challenges that need to be tackled properly to maintain the proposed harvester performance. One of the challenges that have been faced during the fabrication process was the silver weak boundary adhesion to silicon material as will be discussed below. Therefore, deposition of another material is necessary to improve feature robustness. A titanium layer is selected to be deposited underneath the silver layer owing to its low losses at high frequencies and due to its strong adhesion property to silicon substrate. The dispersion effect of the dielectric constant of titanium is also considered by using the Drude model [70, 71]. Figure 5.17 presents the dielectric constants of titanium material.

Adding another metallic layer to the structure proposed above will not only change the mechanical properties, but it will also change the resonance response. Hence, the power harvesting efficiency of the array after adding the titanium layer is recalculated in the same manner introduced in Section 5.3. Desirably, it is found that the new structure yields more than 80% harvesting efficiency at a normal incidence angle and with optimal load of 50 Ω, as shown in Figure 5.18. However, there is a slight frequency shift of approximately 5 GHz after adding the titanium thin film, which is attributed to the change in the electrical

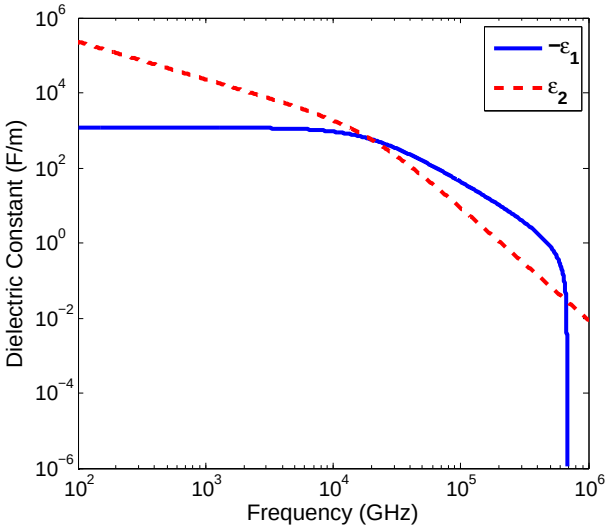

Figure 5.17: The real and imaginary dielectric constants of titanium.

properties of the harvester.

The structure is fabricated on an intrinsic double-side polished silicon wafer, with a high resistivity and low losses at the operating frequency ($< 100 >$ oriented, undoped, $\rho > 10,000\,\Omega.cm, 180\,\mu m$ thick), to minimize potential measurement errors. The first step in the fabrication process was to coat Polymethylmethacrylate (PMMA) resist, a positive electron-beam resist, on top of the silicon wafer at 3200 rpm giving a relatively thick PMMA film (approximately 600 nm). Then, the wafer was baked at 180^{o}C on a hotplate for 20 minutes. Next, the resist was exposed to electron-beam lithography (EBL) at 20 keV with area dose of 200 $\mu\, C/cm^2$, using Raith 150$^{\text{TWO}}$ EBL system. Afterwards, the exposed resist was developed using MIBK:IPA 1:3 solvent and rinsed in 2-propanol (IPA). Use of IPA, which has lower surface energy than water, resulted in less peel off. Finally, the sample was dried by Nitrogen spray gun.

A silver layer with a thickness of 200 nm is then deposited onto the resist pattern by electron-beam evaporation at an evaporation rate of 1.5 Å/sec. Finally, the PMMA resist is lifted off using PG remover. The resist is dissolved in a heated beaker at 90^{o}C, whereby, the metal layer on top of the resist is lifted off. Since the PMMA resist used in this structure is quite thick, the resist was left in the PG remover for three days until the resist was completely dissolved. A schematic of the liftoff process used in this work is illustrated in Figure 5.19. Scanning Electron Microscope (SEM) images of the patterned array harvester and its zoom-in scan are depicted in Figures 5.20 and 5.21, respectively.

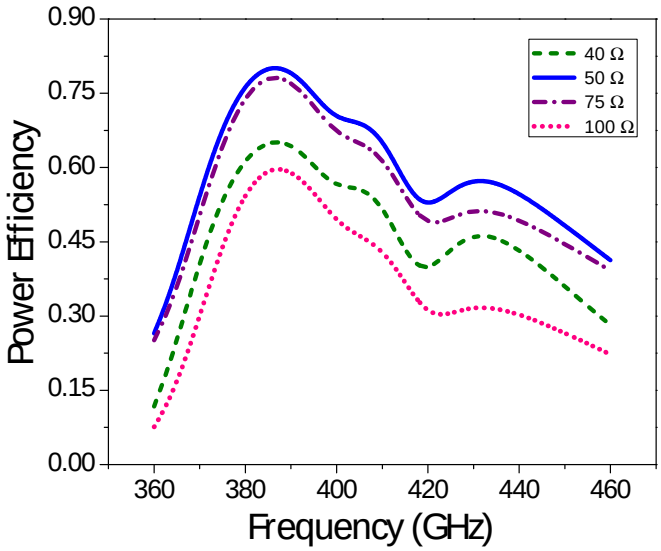

Figure 5.18: Calculated power efficiency of the array after adding Ti layer and loaded by varying resistive sheet.

As discussed above, silver metal is not a good candidate for direct contact with silicon material, since it is only weakly adhesive to silicon. As shown in Figure 5.22b, some parts of the proposed structure were undesirably detached and parts of the PMMA resist inside the SRRs remained after the dissolving process. Therefore, a thin film (5 nm) of titanium was first deposited underneath the top silver layer, with a slow evaporation rate (0.5 Å/sec) and without breaking the vacuum, to enhance the silver adhesion. The silver thickness was decreased to 195 nm to maintain the total metallic thickness of 200 nm. Figure 5.22 illustrates the fabricated sample with and without adding a titanium layer.

5.5 Experimental Results

To validate the numerical findings revealed earlier in this chapter, THz time-domain spectroscopy (THz-TDS) technique is conducted. Transmission mode THz-TDS is chosen over other measurement techniques due to its high reliability and availability of facility issues. The proposed infrared harvester, however, is modified slightly to be compatible with the THz-TDS experiment setup in the transmission mode. Therefore, the eventual structure is fabricated without the ground plane and resistive sheet, and only the top metallic structure with the silicon wafer are considered. In addition, to allow enough THz beam interaction

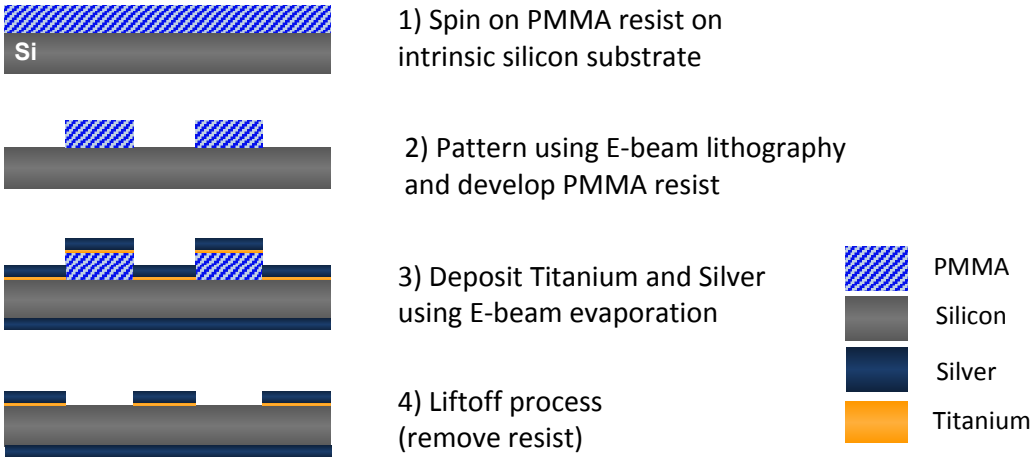

Figure 5.19: Schematic liftoff process used in this work.

with the intended structure, an adequate patch size of the sample is necessary to ensure accurate measured results. To accommodate this need, an array composed of 3000 energy harvesters was fabricated resulting in a $7\,mm \times 7\,mm$ sample size. Because of relatively large and condense sample, the array was fabricated using Vistec EBPG5000plus EBL system.

Transmission mode THz-TDS experimental setup similar to what have been used in [75], was applied. This setup mainly consisted of Ti:sapphire femtosecond laser, transmitter and receiver photoconductive antennas and four off-axis mirrors as illustrated in Figure 5.23. First, the femtosecond laser pulses excite the THz emitter (transmitter antenna) which in turns generate THz pulses. The THz pulses are then collimated by the first off-axis mirror followed by focusing the beam on the sample with aid of the second off-axis mirror. The transmitted THz beam that passes through the sample is collimated again by the third off-axis mirror and then focused by the fourth off-axis mirror on the THz detector. After that, the data of THz pulses is acquired by LabVIEW^{TM} software and Lock-in amplifier.

To measure the sample transmission magnitude, the silicon wafer with and without the metallic structure were at the focus of THz beam. The measured THz temporal pulses, in transient mode, of the sample (shown in Figure 5.24a) and the reference (pure silicon) were fourier transformed to THz spectrums. Figure 5.24b depicts the power spectrum of the transformed THz pulses. Next, the transmission was obtained from the ratio between the sample and reference spectrums. It is worth noting that the float zone silicon used in the structure behaves linearly in THz-TDS [76]. Also, the vapor absorption effect is very weak under frequency of 0.6 THz [77].

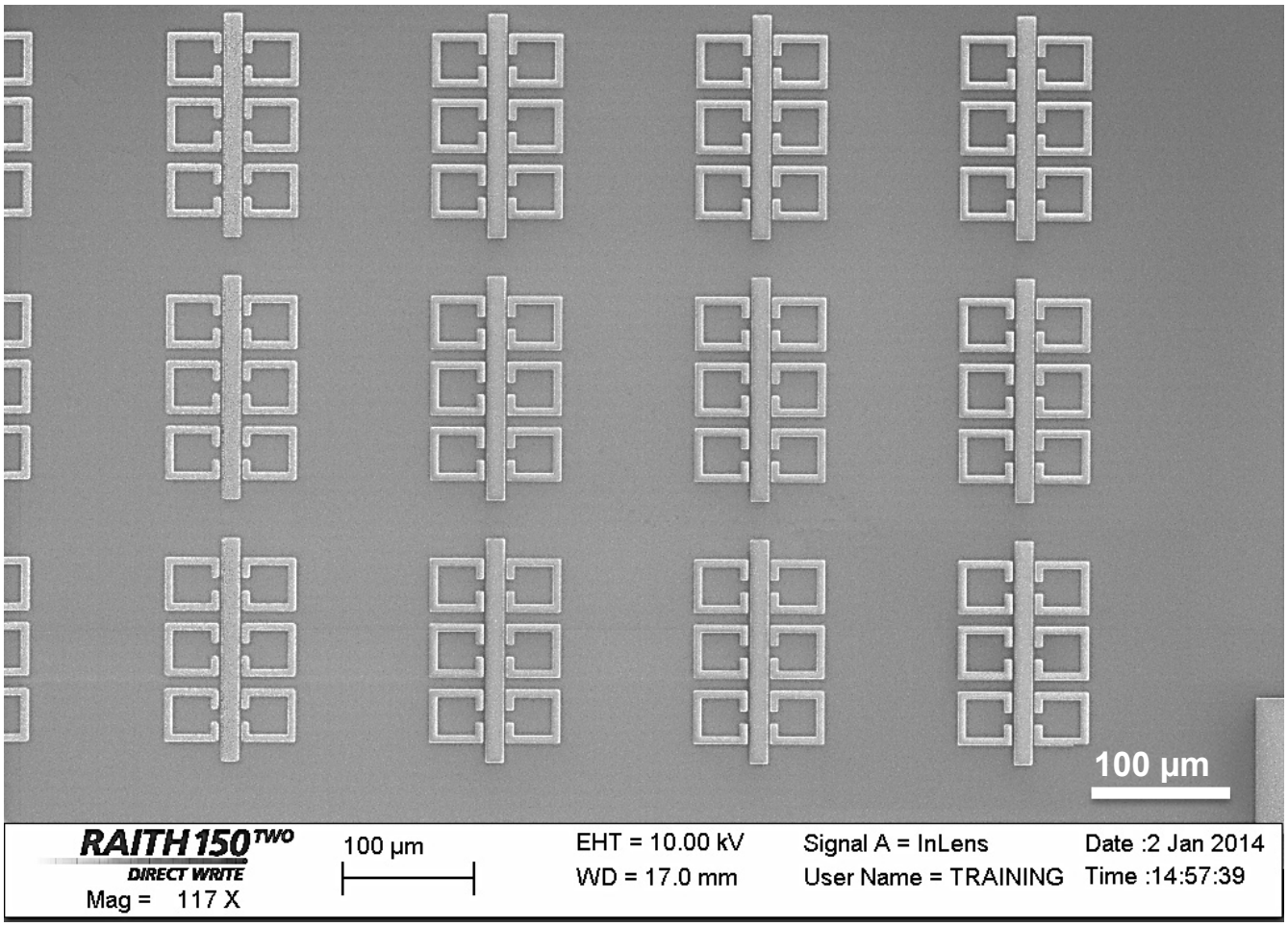

Figure 5.20: SEM image of the patterned PMMA resist of 4×3 square SRRs array.

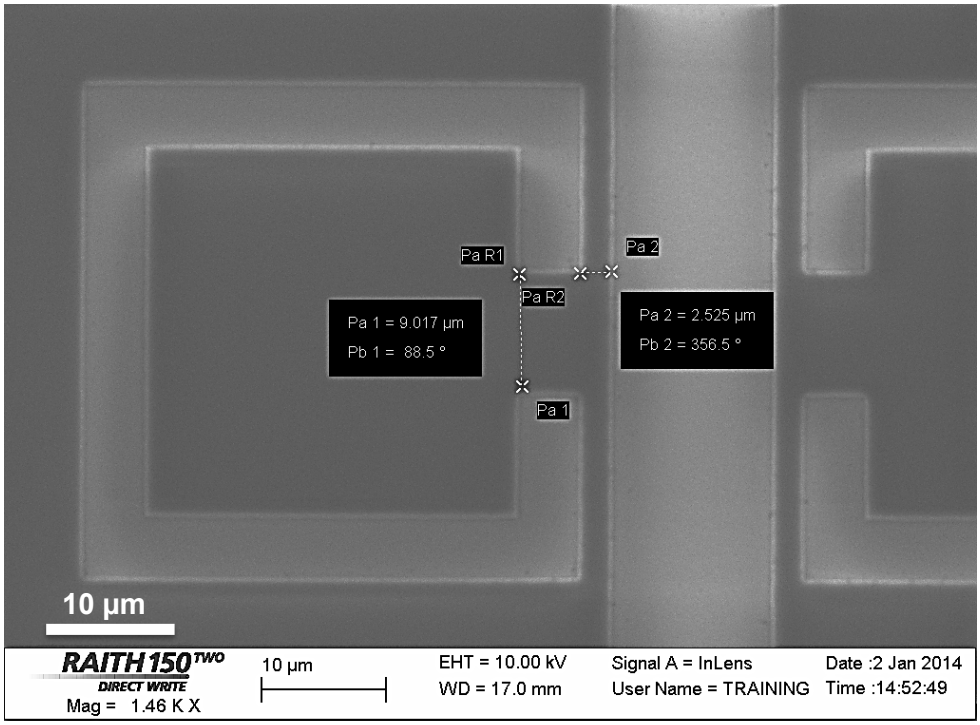

Figure 5.21: Zoom-in scan of the patterned PMMA resist of one of the square SRR.

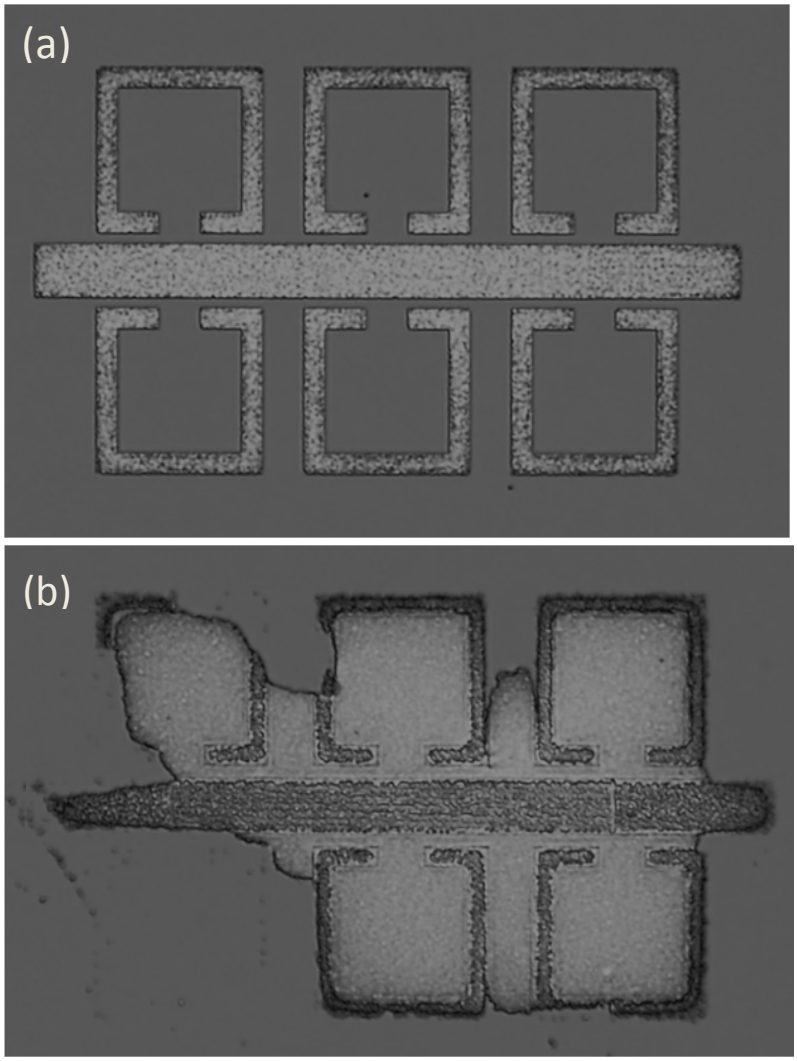

Figure 5.22: Microscopic images of the fabricated structure. (a) After adding adhesive metal layer, (b) without adding adhesive metal layer.

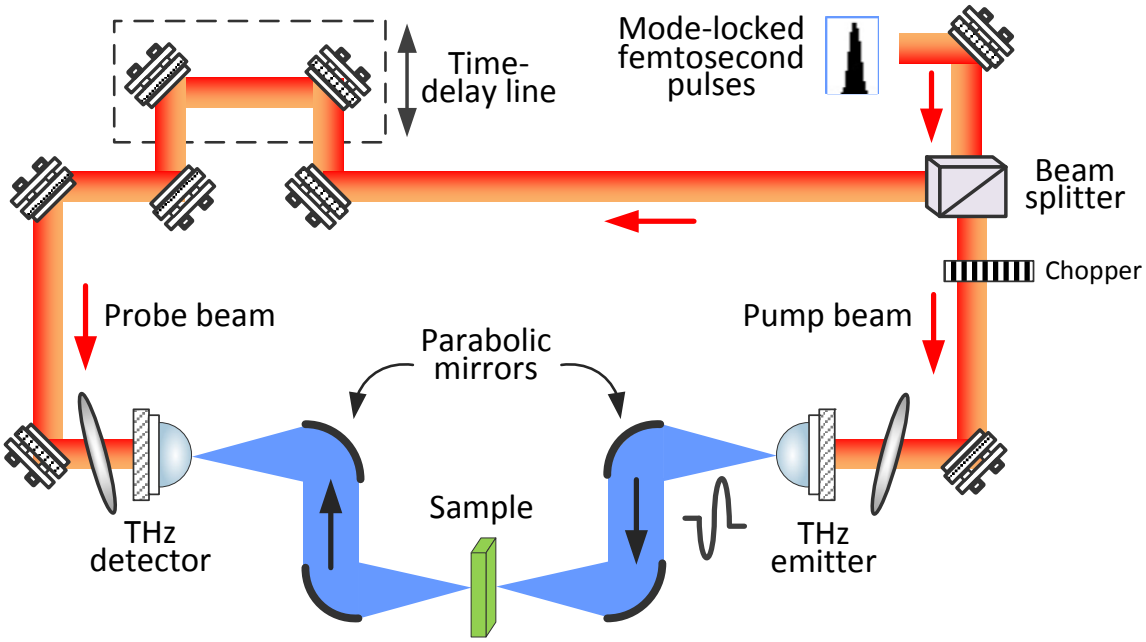

Figure 5.23: Experimental setup for THz-time domain spectroscopy

From Figure 5.25, the energy harvester shows a resonance behaviour approximately at 0.41 THz which is in a good match with resonance frequency shown in Figure 5.16. However, an extra-ordinary transmission was observed at the resonance frequency in lieu of absorption. This phenomenon is attributed mainly to the periodic structure composed of the subwavelength unit cells and to the absence of the ground plane. So at the resonance frequency, more interactions and coupling between the metallic elements were pronounced compared at other frequencies.

For more certainty, the proposed structure was amended by removing the ground plane and forcing the structure periodicity, so both the simulated and fabricated structures are quite similar. The calculated transmission coefficient of the modified structure, as illustrated in Figure 5.26, showed that this periodic structure with the obviation of the ground plane has the same profile of the plot depicted in Figure 5.25. More specifically, a high transmission can be observed around 0.43 THz while a very low transmission happens approximately at 0.48 THz. Although the numerical test result is in agreement with the experimental finding, the deviation between the two plots are owing to the different setups and test environments of both the THz-TDS and simulation experiments.

5.6 Conclusion

This work extended the concept of using an SRR as an electromagnetic energy collector to the infrared frequency regime. Initially, the metal of the resonator, assumed silver in this work, was modeled using the Drude dispersion model and demonstrated potential for harvesting electromagnetic energy in the infrared spectrum despite the electric losses of silver at such high frequency. An ensemble of SRR cells was then used to increase the energy harvesting efficiency by employing a microstrip line within the SRR array to collect the power from the SRR elements and channel it to a resistive load. Power harvesting efficiencies of up to 80% were shown to be feasible using the proposed structure. Subsequently, an array of the proposed assembled harvester was fabricated using the conventional liftoff processes and the structure robustness was enhanced by adding a thin layer of titanium. When an experimental demonstration of the proposed structure was carried out using THz-TDS, the measurements were in good agreement with simulation results. This work offers great promise of harvesting infrared energy with efficiencies far higher than what can be achieved using classical antennas operating within the same spectrum.

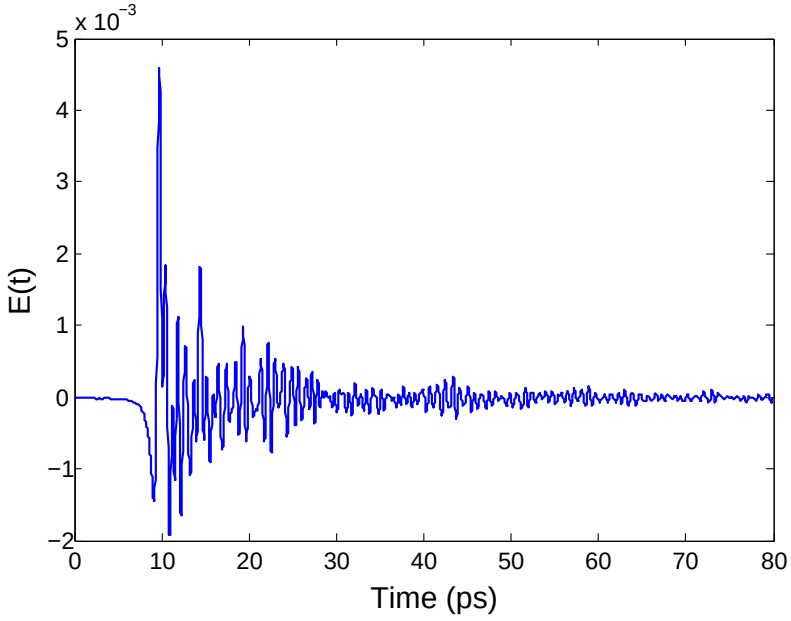

(a)

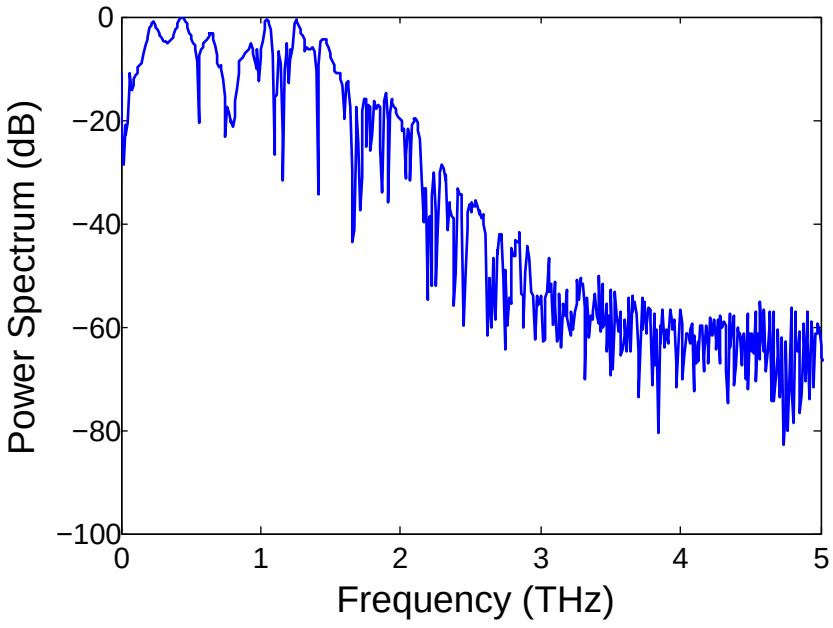

(b)

Figure 5.24: (a) Temporal THz wave and (b) power spectrum of THz wave of the sample

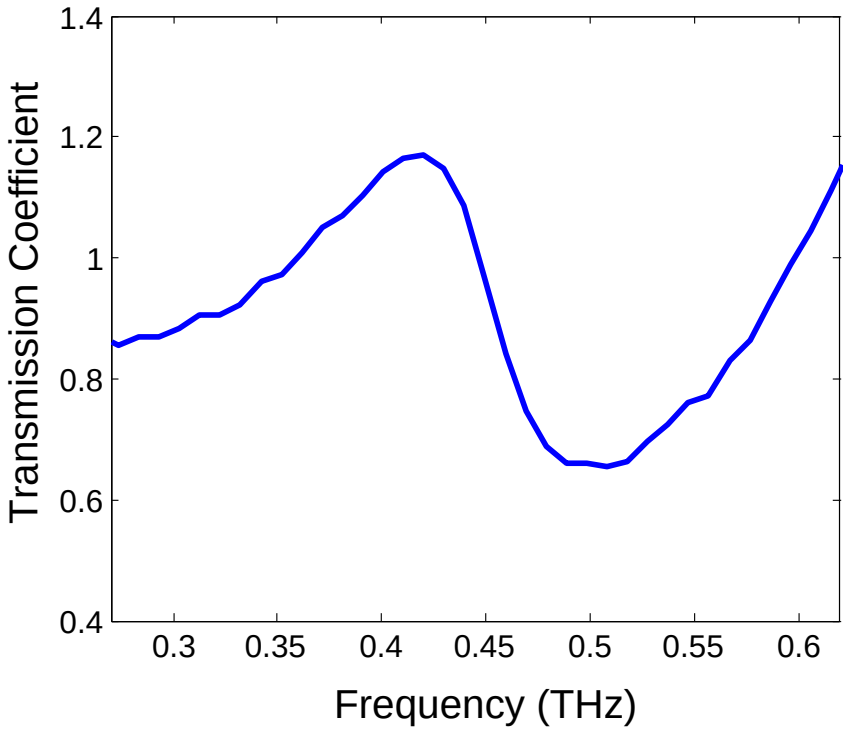

Figure 5.25: Transmission magnitude of the proposed structure

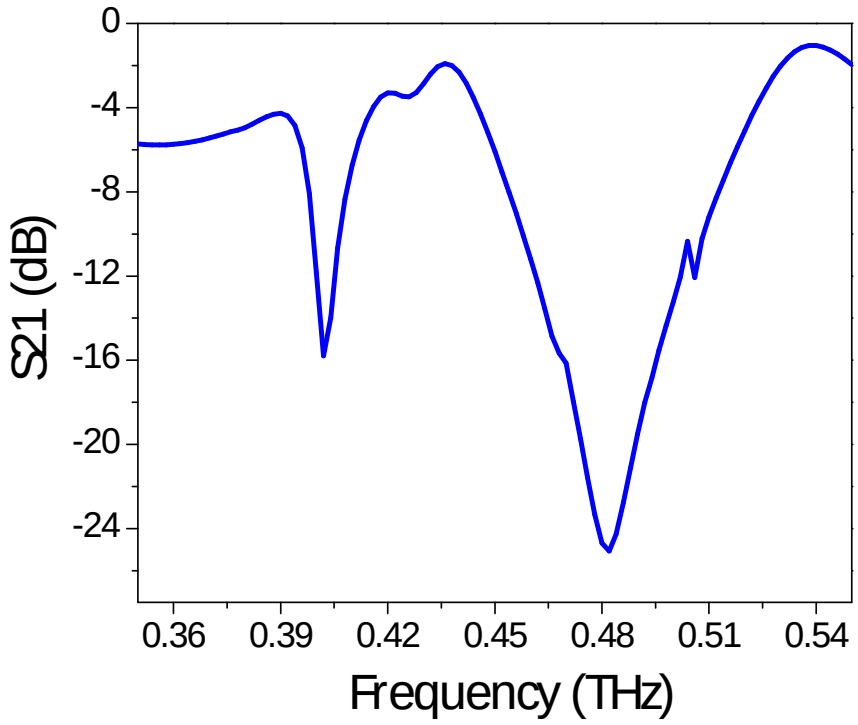

Figure 5.26: The Simulated transmission coefficient of the proposed structure

Chapter 6

Flower-Like Particles for Infrared Energy Harvesting

6.1 Introduction

Benefiting from the ubiquitous infrared energy reaching the earth day and night motivates us to continue increasing the harvesting efficiency, even more than what has been achieved in Chapter 5. Increasing the infrared harnessing efficiency even with a few more percentages will definitely have an eminent impact at mass production level. Since the proposed structure in Chapter 4 shows notable improvements in terms of coupling and dielectric loss suppression, further pursuing is conducted to adopt flower-like design to work at infrared frequency. Of course, appropriate geometric features' modifications and frequency dispersion calculations are needed to fulfil this task.

In this chapter, an electrically small array operating in infrared regime and having the same pattern of the structure presented in Chapter 4 is proposed. The array composed of four circular SRRs and a microstrip line to harvest infrared energy is designed and simulated using 3D electromagnetic simulation tool (ANSYS® HFSS™). The dispersion effect of the metallic layers used in the array are also considered using the Drude model. Moreover, the proposed array is fabricated using conventional liftoff processes and then, experimentally measured using THz-TDS technique.

6.2 Design and Simulation Results

A flower-like array consisting of four circular SRRs arranged in a cruciate pattern around a central microstrip line is proposed. The single resonator is electrically small compared with the free-space wavelength ($diameter < \lambda_o/21$), while the whole array's greatest length is less than $\lambda_o/8$. This configuration is designed to operate in the infrared regime and cover a frequency range from 0.3 THz-0.4 THz. This structure is composed of a silicon (Si) substrate with a thickness (h) of 45 μm and a dielectric constant (ε_r) of 11.9, sandwiched between two silver layers. As shown in Figure 6.1, four SRRs (each with an inner radius of 15 μm and metallic trace width of 5 μm) encircles a microstrip line. The microstrip line is connected to the ground plane through a via and a resistive sheet. Highest power absorption efficiency was observed at a resistive value of 4k Ω. At the resonance frequency, this microstrip line couples and transfers the energy from each excited SRR and then feeds it towards the resistive load at the end of the microstrip line. Since the proposed array operates in the infrared frequency regime, the frequency dependency of the structure is considered by employing the Drude model [69].

The proposed array harvester is simulated using a full-wave simulation tool, ANSYS® HFSS™ [73]. With an electric field ($\mathbf{E}$) polarized in y direction and a normal incidence angle ($\theta = 90^o$), the electric field intensity is simulated at resonance and out of resonance region as shown in Figure 6.2. At resonance frequency, a high electric field intensity develops at the edges of the microstrip line since the edges are the nearest to the resonators gaps. This behavior actually indicates a strong coupling between the resonators and the microstrip line, resulting in an enhancement of current flow through the transmission line towards the resistive load. The electric filed intensity on top of the silicon substrate and immediately underneath the metallic inclusions is also calculated and illustrated in Figure 6.3. The right side of Figure 6.3 shows an oval green spot surrounding the whole array and the electric field magnitude decays outward the array area. This observation indicates to an absorption spot occurring when the structure is shone by an incident wave oscillating at resonance frequency.

The design's power harvesting performance is examined numerically by placing the proposed structure in the middle of a radiation box filled with air, then a plane wave with electric field ($\mathbf{E}$) polarized in y direction set to strike the structure at different incidence angles. Additionally, two sheets are defined on the left and right of the harvester to extract the scattering parameters by the same technique used in Chapter 4. As illustrated in Figure 6.4, the harvester exhibits more confinement tendency at a perpendicular incidence angle compared to an incident wave with zero-azimuth angle. Strictly speaking, from Figures 6.4b and 6.4d, both S_{21} and S_{11} have lower values compared with Figures 6.4a and 6.4c,

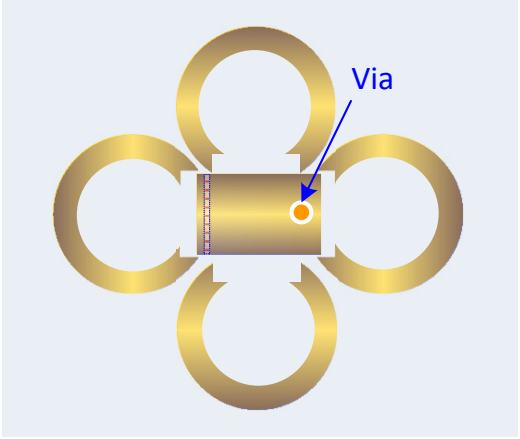

(a)

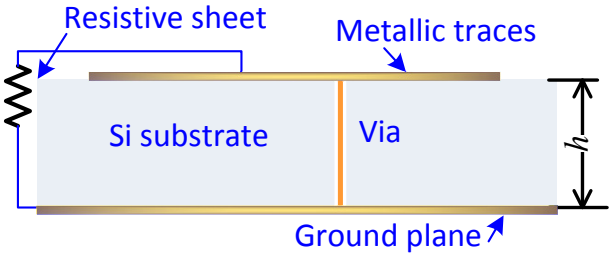

(b)

Figure 6.1: Layout of the flower-like energy harvester. (a) Top view and (b) side view

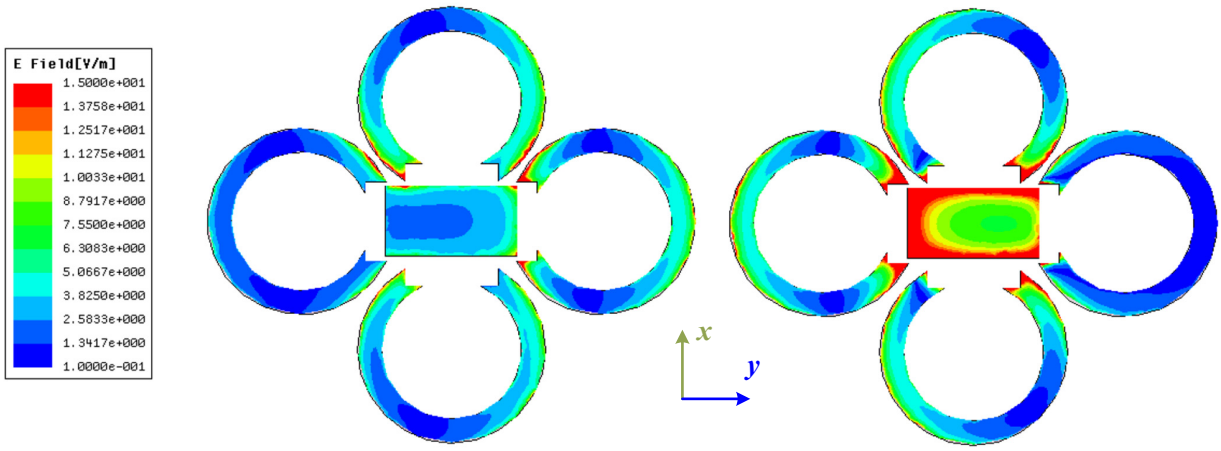

Figure 6.2: Simulation results of the electric field distributions on the metallic elements of the flower-like energy harvester (left) out of resonance region and (right) at resonance frequency with the electric field (**E**) polarized in y direction

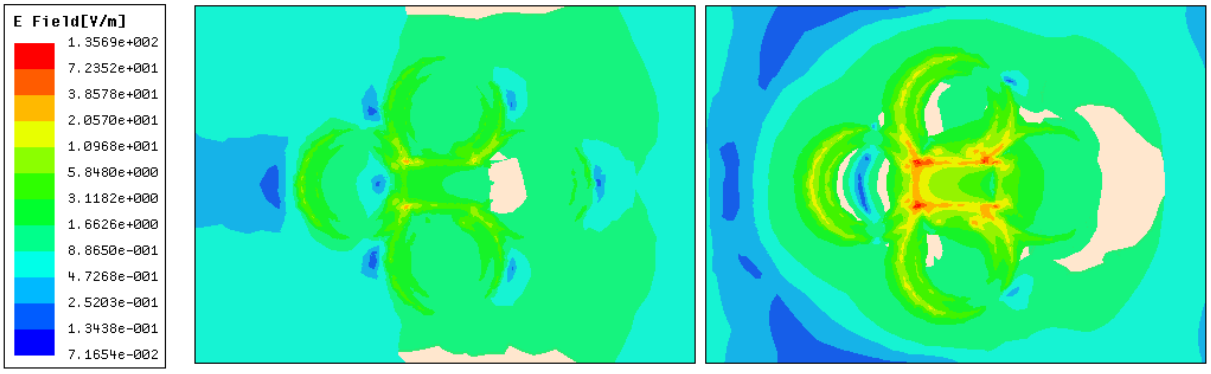

Figure 6.3: Simulated electric field distributions on top of the silicon substrate (left) out of resonance region and (right) at resonance frequency with the electric field (**E**) polarized in y direction. Field variations are illustrated in logarithmic scale

respectively. This observation indicates more energy trapping, which in turn leads to a higher energy harvesting efficiency as will be shown below.

The power harvesting efficiency is calculated in a manner similar to that presented in Chapters 4 and 5 [62, 67]. Figure 6.5 presents the calculated power efficiency of the array with 4k Ω resistive load. More than 85% of power harvesting is achieved by this structure at a resonance frequency of 348 GHz. Furthermore, a bandwidth of 11% where the power harvesting efficiency is equal to or more than 30% is achieved.

In fact, the simulation results show feasible infrared energy harvesting with the aforementioned array. To validate the results experimentally, the proposed configuration has been fabricated using nano-fabrication tools as will be introduced in Section 6.3.

6.3 Fabrication Results

The flower-like energy harvester proposed here falls within the range of the previous infrared energy harvester presented in Chapter 5 in terms of geometric dimensions, where Figure 6.6 shows the dimension of a unit cell of the flower-like harvester. Therefore, the same fabrication procedures adopted in the previous chapter, as shown in Figure 6.7, are followed to bring this design to reality. Briefly, an intrinsic silicon wafer which has a high resistivity and low losses at the operating frequency ($< 100 >$ oriented, undoped, $\rho > 10,000\,\Omega.cm, 180\,\mu m$ thick), is coated by PMMA resist. Then, the array feature is patterned on the coated silicon using EBL at 20 keV with area dose of $200\,\mu C/cm^2$, by means of Raith 150^{TWO} EBL system. After the patterning, the resist was developed using MIBK:IPA 1:3 solvent and followed by rinse in 2-propanol (IPA). After patterning and developing, SEM images of the flower-like harvester and its zoom-in scan are taken and depicted in Figures 6.8 and 6.9, respectively.

As discussed in Section 5.4, weak silver film adhesives to silicon material, so a titanium film was deposited to strengthen the adhesion to the substrate and to protect the structure features during the liftoff process. Proceeding with this step, a metallic layer with thickness of 200 nm composed of titanium and silver films were deposited by electron-beam evaporation. Figure 6.10 presents the effect of adding a titanium layer in strengthening the structure metallic inclusions. In the previous chapter, it has been demonstrated that adding a titanium thin film layer does not degrade the performance, if not improve the harvesting efficiency. A harvesting efficiency after adding the titanium layer is computed with considering the dispersion effects of both silver and titanium. Lastly, the PMMA resist is lifted off using PG remover, where the metal layer on top of the resist is lifted

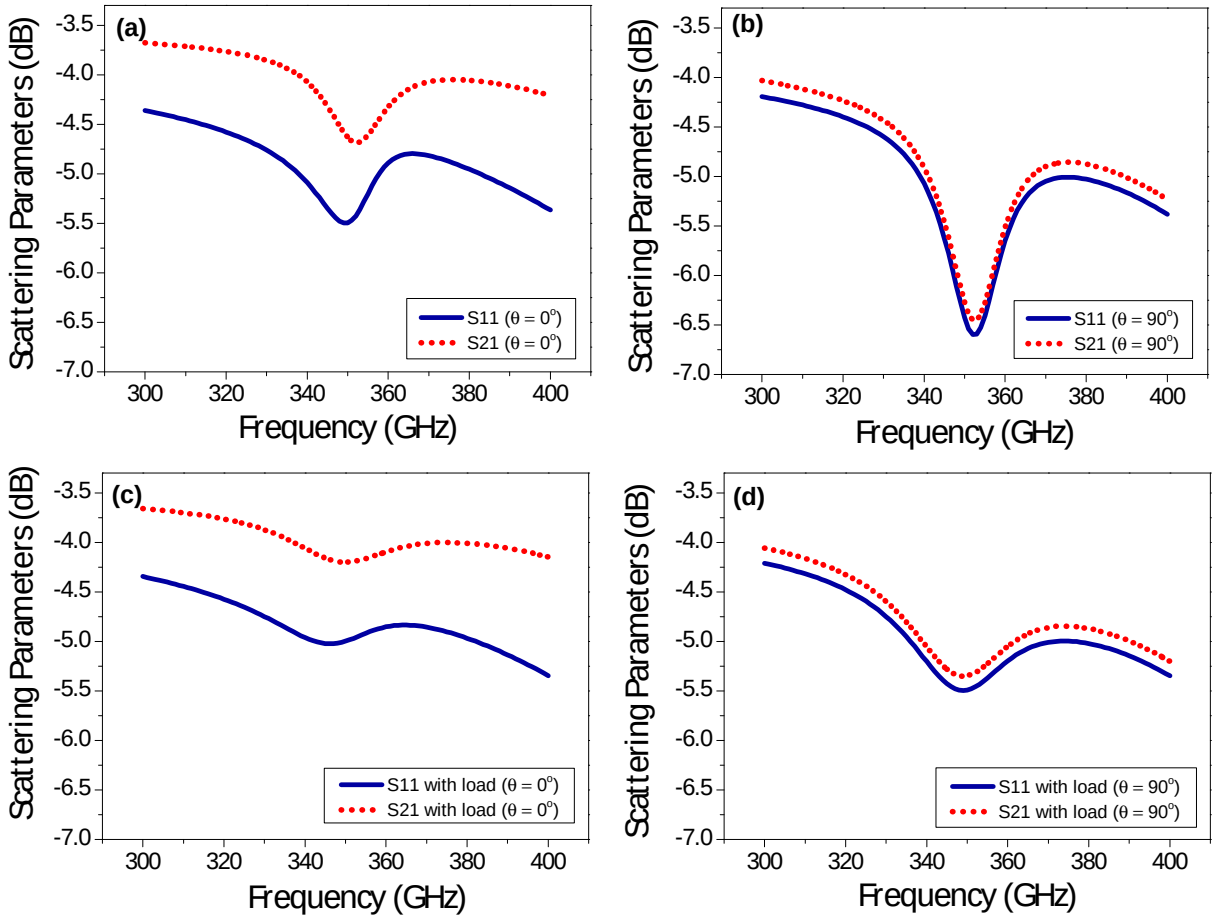

Figure 6.4: Simulated scattering parameters for the the infrared flower-like energy harvester. (a) Without resistive load at incidence angle $\theta = 0^o$, (b) without resistive load at incidence angle $\theta = 90^o$, (c) with resistive load at incidence angle $\theta = 0^o$, (d) with resistive load at incidence angle $\theta = 90^o$

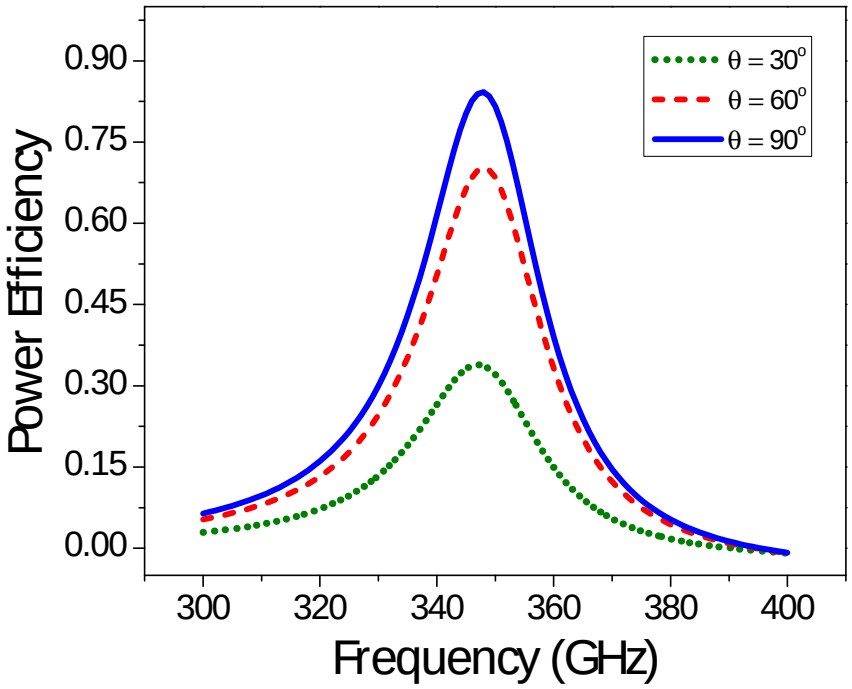

Figure 6.5: Simulation results of the power efficiency of the proposed energy harvester loaded by 4k Ω at different incidence angles

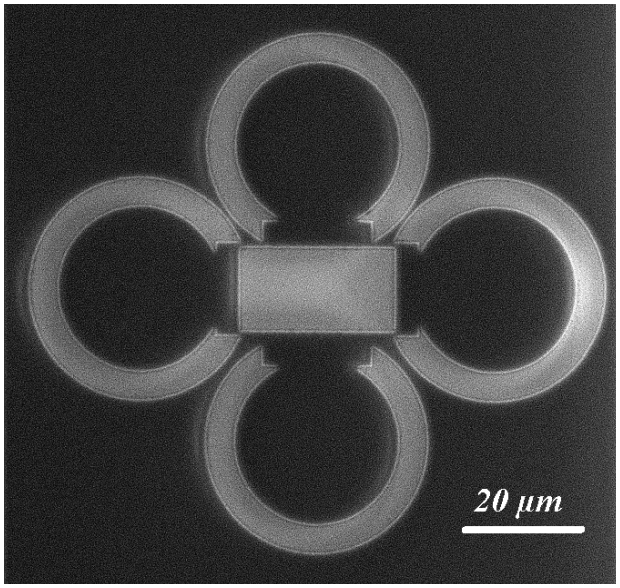

Figure 6.6: SEM image of the fabricated array

off. In regard to the impact of adding a titanium film on harvesting efficiency, Figure 6.11 presents the calculated power efficiency of the flower-like energy harvester after adding titanium thin film at a normal incidence angle and loaded by different resistive sheets. It is found that at $4\mathrm{k}\,\Omega$ resistive load, the highest power occurs which is the case of the same structure but with a silver layer only.

6.4 Experimental Results

With the same procedures used in Section 5.5, the THz-TDS experiment in the transmission mode is conducted to validate the proposed flower-like harvester. So an array comprises 3600 flower-like harvesters was fabricated using Vistec EBPG5000plus EBL system and yielded approximately a $7\,mm \times 7\,mm$ sample size. The spectrums of the silicon wafer (reference) and the patterned structures were generated from the measured THz pulses in time domain. Figure 6.12 presents the measured THz temporal pulses and the power spectrum, both belong to the proposed array.

The transmission magnitude was also extracted from the ratio between the sample and reference spectrums and is shown in Figure 6.13. One can observe that the transmission magnitude for the flower-like harvester holds the same view of the structure proposed earlier

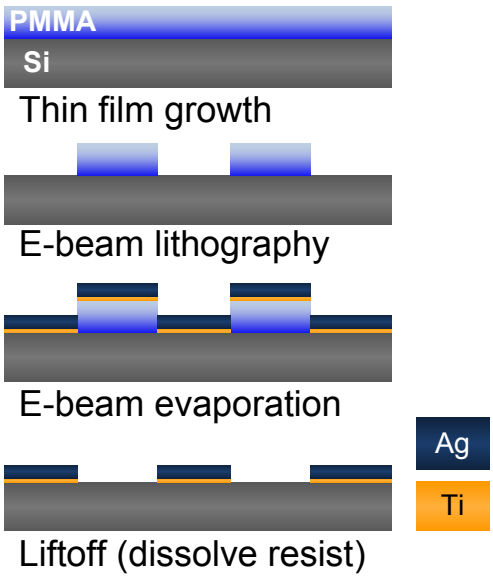

Figure 6.7: Schematic liftoff process used in this work

in Chapter 5. Indeed, the similarity in response in the transmission mode is imputed to the similarity in periodicity, silicon wafer and energy harvesting behaviour of the two structures.

It is important to mention that having a ground plane as introduced before in the simulation work plays an important role in confining and saving the harvested energy from being transmitted. This behaviour can be clearly seen from Figure 6.4b, where both the reflection and transmission waves drop at resonance frequency demonstrating the energy confinement within the structure. In contrast, the structure without a ground plane, which is the case of the conducted experiment, shows a high transmission phenomenon. To elaborate, most of the collected power by the sub-wavelength metallic particles passes through the silicon substrate, implies to a highly pronounced transmission at the resonance frequency, as depicted in Figure 6.13. By bringing these two images of Figures 6.4b and 6.13 together, one can observe the correlation between them as an image and its opposite, since the ground plane is removed from the latter case.

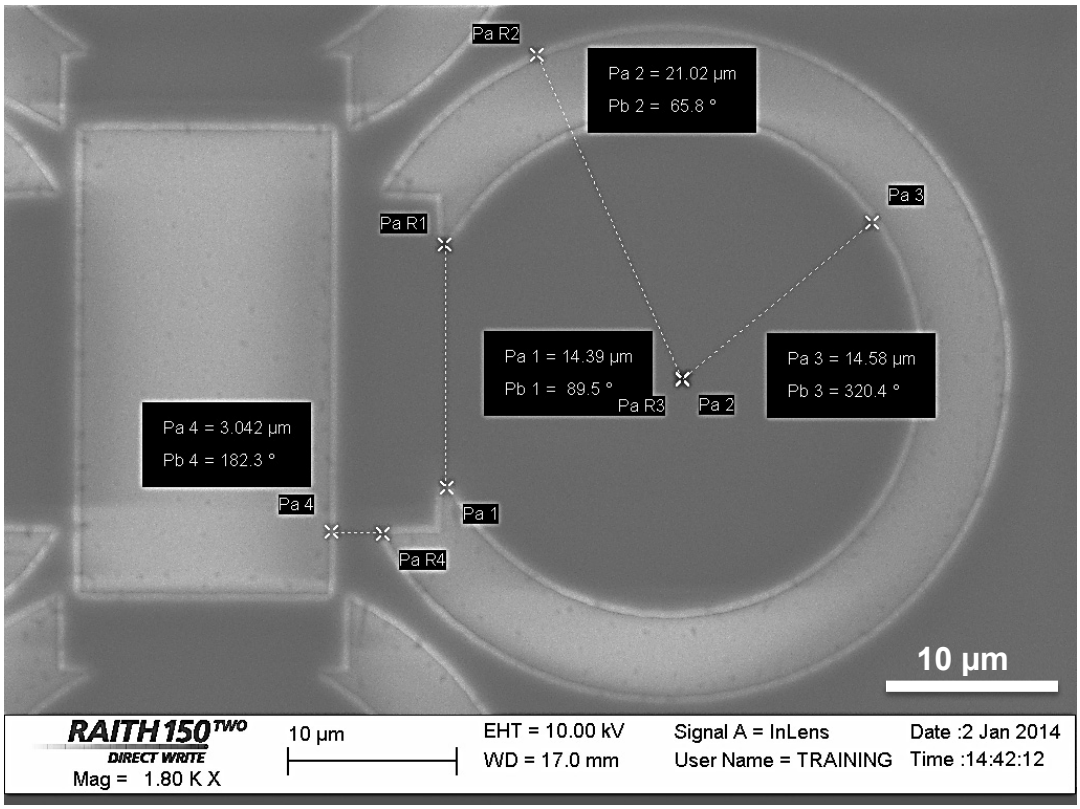

Figure 6.8: Zoom-in scan of the patterned PMMA resist of one flower-like harvester

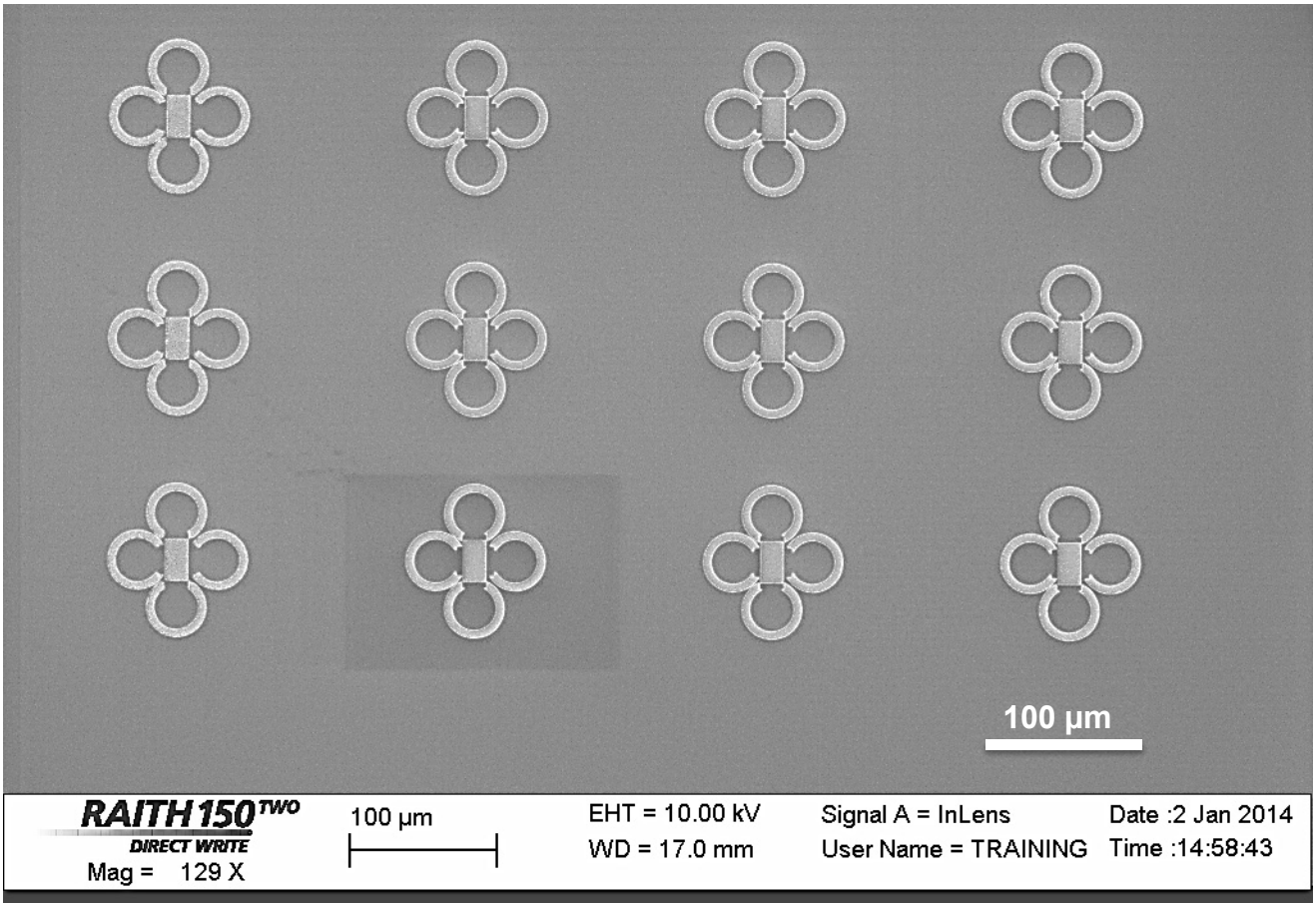

Figure 6.9: SEM image of the patterned PMMA resist of 4×3 flower-like arrays

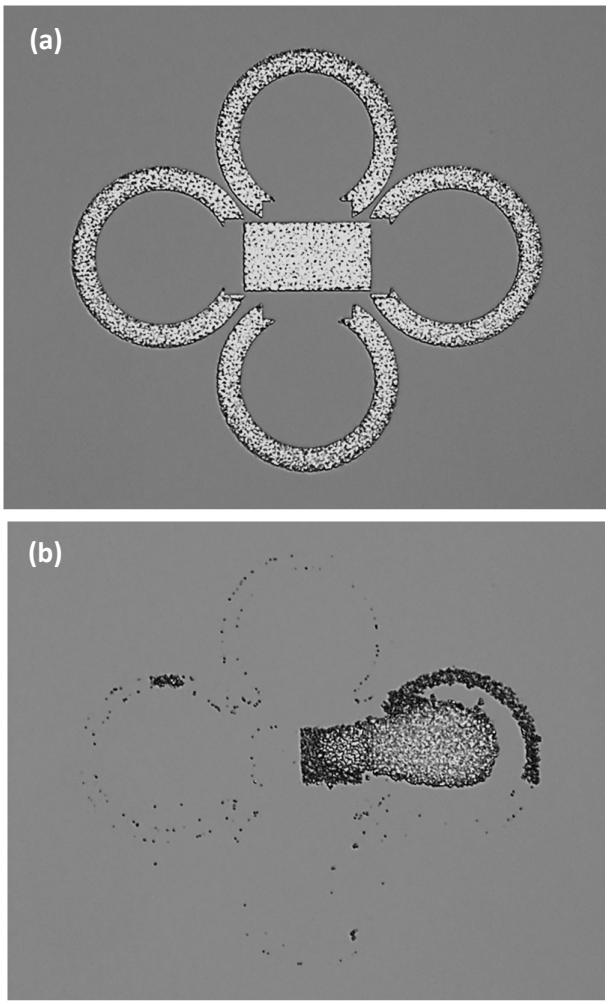

Figure 6.10: Microscopic images of the fabricated flower-like array. (a) After adding adhesive metal layer, (b) without adding adhesive metal layer

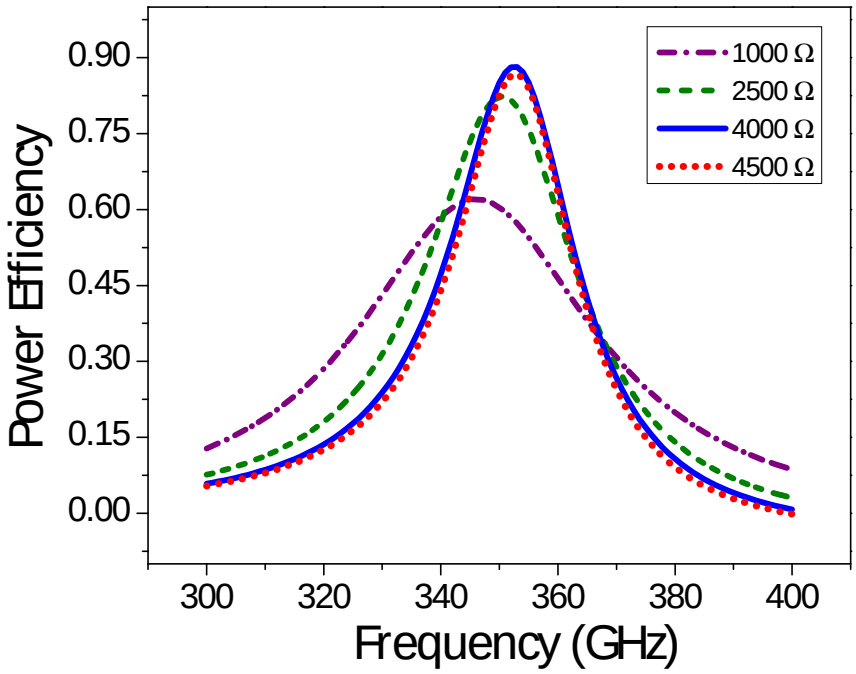

Figure 6.11: Calculated power efficiency of the flower-like energy harvester after adding Ti thin film at a normal incidence angle and loaded by different resistive sheets

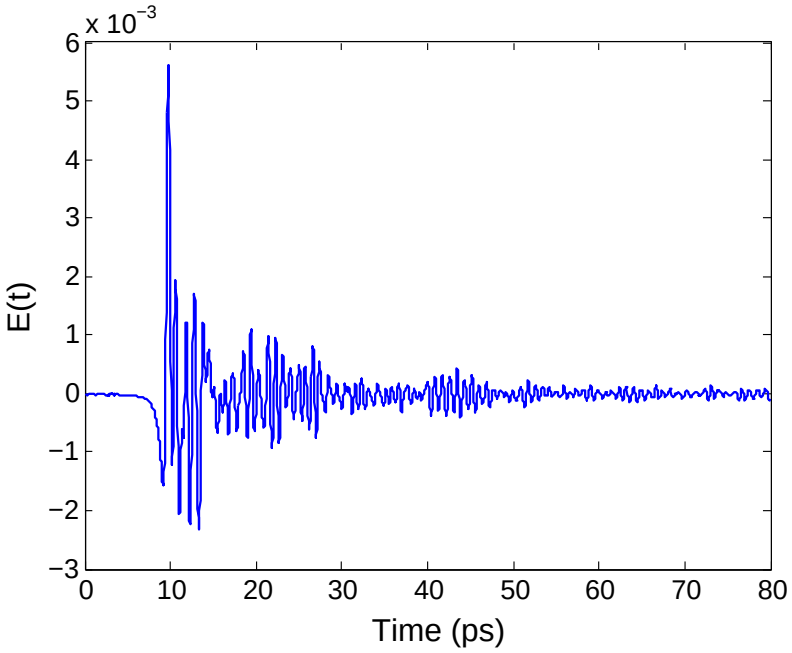

(a)

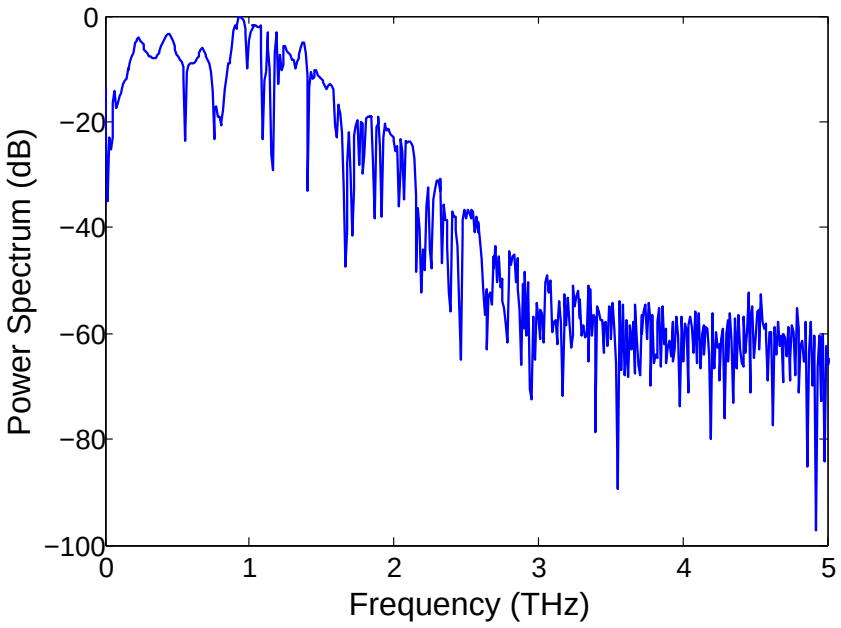

(b)

Figure 6.12: (a) Temporal THz wave and (b) power spectrum of THz wave of the sample

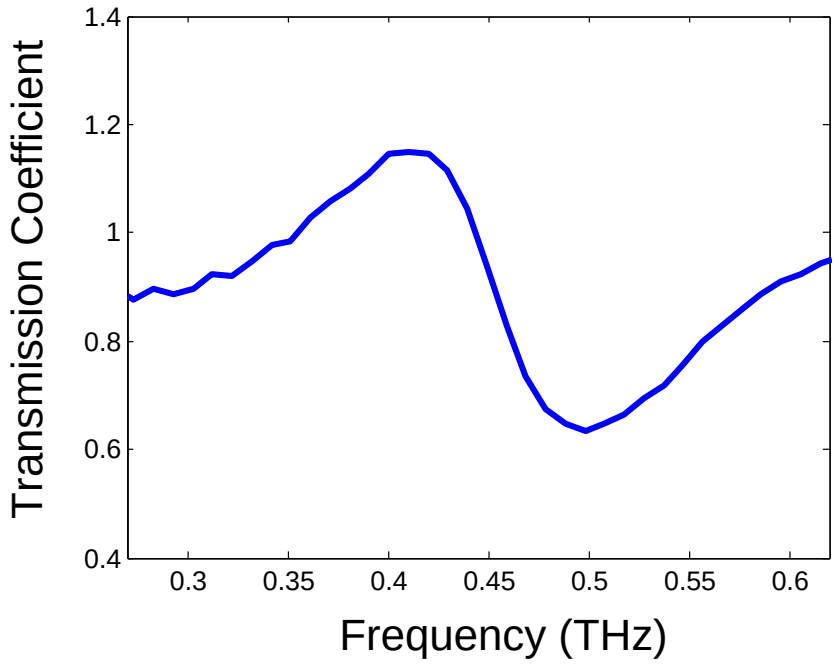

Figure 6.13: Transmission magnitude of the flower-like harvester

6.5 Conclusion

A flower-like array composed of electrically small resonators to harvest and channel electromagnetic energy in the infrared regime were designed and fabricated. The numerical results showed a high power harvesting efficiency reaching more than 85% at normal incidence angle. The theoretical findings were also compared with the experiment using THz-TDS technique.

Chapter 7

Concluding Remarks

7.1 Summary and Contributions

This thesis addressed a dramatic improvement in energy harvesting both in the microwave and infrared regimes utilizing electrically small particles. At the beginning of this thesis, a literature review of the main transducers to harvest energy that lies within the electromagnetic spectrum was introduced. In particular, photovoltaic technology and its recent advancements were presented. Furthermore, rectenna systems used for WPT purposes and their main elements, such as antennas and rectification circuits, were discussed. In this work, several topologies composed of electrically small resonators to harvest ambient electromagnetic waves were proposed. Succinctly, the results obtained from this research showed a potential for future enhancement of renewable energy conversion systems.

During the course of this research, various stages were achieved, starting with the proof of concept of a single SRR and moving to nano-scale fabrications and then THz-TDS measurements. In summary, this thesis offered following accomplishments:

- A new concept of harvesting energy utilizing an electrically small resonator was proposed. A prototype SRR designed at 5.8 GHz was simulated and fabricated to demonstrate the proposed concept.
  [O. Ramahi, T. Almoneef, **Mohammed R. AlShareef**, and M. Boybay, "Metamaterial particles for electromagnetic energy harvesting," *Applied Physics Letters*, vol. 101, no. 17, pp. 173903–5, 2012
  "Metamaterial particles for electromagnetic energy harvesting." *U.S. Patent Application no. 13/841652*, March, 2013.]

- A bow-tie antenna and the proposed SRR were compared to show the efficiency improvement of power harvesting. A substantial power efficiency improvement using the metamaterial element was observed compared to the classical antenna. The bow-tie antenna achieved about 13% power efficiency, whereas the SRR achieved more than 37%. A new efficiency definition was proposed to take into account the size reduction by utilizing electrically small resonators, which in turn, increases the total power efficiency. Moreover, two arrays having the same area, both designed at 5.8 GHz, produced $0.153\,mW$ and $0.632\,mW$, as power harvested for the bow-tie antennas and SRRs, respectively.
  [**Mohammed R. AlShareef** and O. Ramahi, "Energy harvesting in the microwaves spectrum using electrically small resonators," in *International Congress on Energy Efficiency and Energy Related Materials (ENEFM2013)*, vol. 155 of *Springer Proceedings in Physics*, pp. 265–272, Springer International Publishing, 2014]

- An array composed of electrically small resonators to harvest electromagnetic energy in the microwave regime was designed and fabricated. The proposed configuration created in- and out-of-phase currents, which in turn increased the current flow on the microstrip line and concurrently limited the dielectric loss in the substrate. Approximately 44% at 5.67 GHz and 38% at 5.77 GHz power harvesting efficiencies were achieved with the four and two circular SRRs arrays respectively, at a normal incidence angle. The concept of power harvesting with the proposed configuration was validated experimentally. Moreover, it was shown that positioning any two elements of the proposed configuration in a closely-adjacent manner contributed to improving the overall harvesting efficiency.
  [**Mohammed R. AlShareef** and O. Ramahi, "Electrically small particles combining even- and odd-mode currents for microwave energy harvesting," *Applied Physics Letters*, vol. 104, no. 25, pp. 253906–5, 2014]

- An ensemble of six square SRRs and a microstrip transmission to trap infrared energy was proposed. The metal of the structure, assumed to be silver in this work, was modeled using the Drude dispersion model and demonstrated potential for harvesting electromagnetic energy in the infrared spectrum despite the electric losses of silver at such high frequency. An ensemble of SRR cells was then used to increase the energy harvesting efficiency by employing a microstrip line within the SRR array to collect the power from the SRR elements and channel it to a resistive load. Power harvesting efficiencies of up to 80% were shown to be feasible using the proposed structure. Subsequently, an array of the proposed assembled harvester was fabricated using the conventional liftoff processes and the structure's robustness was enhanced by adding

a thin layer of titanium. When an experimental demonstration of the proposed structure was carried out using THz-TDS, the measurements were consistent with simulation results.
[**Mohammed R. AlShareef** and O. Ramahi, "Electrically small resonators for energy harvesting in the infrared regime," *Journal of Applied Physics*, vol. 114, no. 22, pp. 223101–6, 2013
Mohammed R. AlShareef, B. Cui, and O. Ramahi, "Fabrication of infrared energy harvester using electrically small particles," in *Technical Proceedings of the 2014 Clean Technology Conference and Trade Show*, pp. 120–123, Clean Technology and Sustainable Industries, 2014
"Arrays of electrically-small resonators for electromagnetic energy harvesting in the THz, infrared and visible frequency spectra and method to channel energy through waveguiding structures." *U.S. Provisional Patent US61912566*. December, 2013.]

- A flower-like array composed of electrically small resonators to harvest and channel electromagnetic energy in the infrared regime was designed and fabricated. The numerical results showed a high power harvesting efficiency reaching more than 85% at normal incidence. The theoretical findings were compared with experiment using THz-TDS technique.
  [**Mohammed R. AlShareef** and O. Ramahi, "Electrically small particles for harvesting and channeling infrared energy," in *Antenna Technology and Applied Electromagnetics (ANTEM), 2014 16th International Symposium on*, pp. 1–2, July 2014, *(Best Student Paper Award, third place)*]

7.2 Suggested Future Work

The concept addressed in this work, harvesting energy at different spectrum wavelengths, indeed opens the way to prototype an integral system that can trap and convert the electromagnetic energy into viable power efficiently and cost-effectively. Since the transducer investigated herein is the cornerstone of the harvesting systems and provides only AC signals, incorporating a rectification system would be a worthy interest to pursue. Thus, useful DC power can be obtained and then used for the designated applications. Increasing the power harvesting capability of a structure can be obtained by prototyping multiple arrays of that structure. However, multiple array elements add more complexity in terms of design and network matching. Therefore, different schemes of array structures need to be developed in order to increase the harvesting capability. In addition, optimization processes need to be considered to achieve the highest possible performance.

Since the proposed mechanism can be extended to operate at other frequencies, a logical extension to harvest the visible light energy would be of primary consideration. Furthermore, widening the bandwidth response of a transducer while maintaining the rectification and matching performance is worthy of examination.

Bibliography

[1] A. Luque, "Will we exceed 50% efficiency in photovoltaics?," *Journal of Applied Physics*, vol. 110, no. 3, pp. 031301–031301–19, 2011. ix, 1, 10, 12, 13

[2] G. Sala and I. Antón, *Photovoltaic Concentrators*, ch. 10, pp. 402–451. John Wiley & Sons, Ltd, 2011. x, 12

[3] D. K. Kotter, S. D. Novack, W. D. Slafer, and P. J. Pinhero, "Theory and manufacturing processes of solar nanoantenna electromagnetic collectors," *Journal of Solar Energy Engineering-Transactions of the ASME*, vol. 132, p. 011014, Feb 2010. x, 13, 14

[4] C. Simovski, D. Morits, P. Voroshilov, M. Guzhva, P. Belov, and Y. Kivshar, "Enhanced efficiency of light-trapping nanoantenna arrays for thin-film solar cells," *Opt. Express*, vol. 21, pp. A714–A725, July 2013. x, 14, 15

[5] E. Briones, J. Alda, and F. J. González, "Conversion efficiency of broad-band rectennas for solar energy harvesting applications," *Opt. Express*, vol. 21, pp. A412–A418, May 2013. x, 13, 14, 15

[6] J. McSpadden, L. Fan, and K. Chang, "Design and experiments of a high conversion efficiency 5.8 GHz rectenna," *Microwave Theory and Techniques, IEEE Transactions on*, vol. 46, pp. 2053 –2060, Dec 1998. x, 3, 17, 28

[7] J. Hagerty, F. Helmbrecht, W. McCalpin, R. Zane, and Z. Popovic, "Recycling ambient microwave energy with broad-band rectenna arrays," *Microwave Theory and Techniques, IEEE Transactions on*, vol. 52, pp. 1014–1024, March 2004. x, 17

[8] J. Bean, A. Weeks, and G. D. Boreman, "Performance optimization of antenna-coupled Al/Alo_x/Pt tunnel diode infrared detectors," *Quantum Electronics, IEEE Journal of*, vol. 47, pp. 126–135, Jan 2011. x, 19

[9] C. Ibarra-Castanedo, *Quantitative subsurface defect evaluation by pulsed phase thermography: depth retrieval with the phase*. PhD thesis, Laval University, 2005. xii, 53

[10] J. Yang, D. Cheong, J. Rideout, S. Tavakoli, and R. Kleiman, "Silicon-based multijunction solar cell with 19.7% efficiency at 1-sun using areal current matching for 2-terminal operation," in *Photovoltaic Specialists Conference (PVSC), 2011 37th IEEE*, pp. 1019–1024, June 2011. 1

[11] R. R. King, D. C. Law, K. M. Edmondson, C. M. Fetzer, G. S. Kinsey, H. Yoon, R. A. Sherif, and N. H. Karam, "40% efficient metamorphic GaInp/GaInAs/Ge multijunction solar cells," *Applied Physics Letters*, vol. 90, no. 18, p. 183516, 2007. 1

[12] M. Green, "Recent developments in photovoltaics," *Solar Energy*, vol. 76, no. 13, pp. 3 – 8, 2004. Solar World Congress 2001. 1

[13] M. Green, P. Basore, N. Chang, D. Clugston, R. Egan, R. Evans, D. Hogg, S. Jarnason, M. Keevers, P. Lasswell, J. OSullivan, U. Schubert, A. Turner, S. Wenham, and T. Young, "Crystalline silicon on glass (CSG) thin-film solar cell modules," *Solar Energy*, vol. 77, no. 6, pp. 857–863, 2004. 1

[14] A. G. Aberle, "Progress with polycrystalline silicon thin-film solar cells on glass at UNSW," *Journal of Crystal Growth*, vol. 287, no. 2, pp. 386–390, 2006. 1

[15] S. Pillai, K. R. Catchpole, T. Trupke, and M. A. Green, "Surface plasmon enhanced silicon solar cells," *Journal of Applied Physics*, vol. 101, no. 9, p. 093105, 2007. 1, 8, 9, 54

[16] R. L. Bailey, "A proposed new concept for a solar-energy converter," *Journal of Engineering for Power*, vol. 94, no. 2, pp. 73–77, 1972. 3

[17] J. McSpadden, T. Yoo, and K. Chang, "Theoretical and experimental investigation of a rectenna element for microwave power transmission," *Microwave Theory and Techniques, IEEE Transactions on*, vol. 40, pp. 2359–2366, Dec 1992. 3, 39

[18] Y.-H. Suh and K. Chang, "A novel dual frequency rectenna for high efficiency wireless power transmission at 2.45 and 5.8 GHz," in *Microwave Symposium Digest, 2002 IEEE MTT-S International*, vol. 2, pp. 1297–1300, 2002. 3

[19] Y.-H. Suh and K. Chang, "A high-efficiency dual-frequency rectenna for 2.45- and 5.8-GHz wireless power transmission," *Microwave Theory and Techniques, IEEE Transactions on*, vol. 50, pp. 1784–1789, July 2002. 3

[20] B. Strassner and K. Chang, "5.8-GHz circularly polarized dual-rhombic-loop traveling-wave rectifying antenna for low power-density wireless power transmission applications," *Microwave Theory and Techniques, IEEE Transactions on*, vol. 51, pp. 1548–1553, May 2003. 3

[21] Y.-J. Ren and K. Chang, "Bow-tie retrodirective rectenna," *Electronics Letters*, vol. 42, pp. 191–192, Feb 2006. 3

[22] Y.-J. Ren and K. Chang, "New 5.8-GHz circularly polarized retrodirective rectenna arrays for wireless power transmission," *Microwave Theory and Techniques, IEEE Transactions on*, vol. 54, pp. 2970–2976, July 2006. 3, 4, 39

[23] H. Sun, Y.-X. Guo, M. He, and Z. Zhong, "A dual-band rectenna using broadband yagi antenna array for ambient rf power harvesting," *Antennas and Wireless Propagation Letters, IEEE*, vol. 12, pp. 918–921, 2013. 3, 39

[24] W.-H. Tu, S.-H. Hsu, and K. Chang, "Compact 5.8-GHz rectenna using stepped-impedance dipole antenna," *Antennas and Wireless Propagation Letters, IEEE*, vol. 6, pp. 282–284, 2007. 4, 39

[25] N. Shinohara and H. Matsumoto, "Experimental study of large rectenna array for microwave energy transmission," *Microwave Theory and Techniques, IEEE Transactions on*, vol. 46, pp. 261–268, Mar 1998. 4, 16, 39

[26] D.-G. Youn, Y.-H. Park, K.-H. Kim, and Y.-C. Rhee, "A study on the fundamental transmission experiment for wireless power transmission system," in *TENCON 99. Proceedings of the IEEE Region 10 Conference*, vol. 2, pp. 1419–1422, Dec 1999. 4, 39

[27] Y.-H. Park, D.-G. Youn, K.-H. Kim, and Y.-C. Rhee, "A study on the analysis of rectenna efficiency for wireless power transmission," in *TENCON 99. Proceedings of the IEEE Region 10 Conference*, vol. 2, pp. 1423–1426, Dec 1999. 4, 39

[28] D. R. Smith, J. B. Pendry, and M. C. K. Wiltshire, "Metamaterials and negative refractive index," *Science*, vol. 305, no. 5685, pp. 788–792, 2004. 4

[29] J. B. Pendry, "Negative refraction makes a perfect lens," *Phys. Rev. Lett.*, vol. 85, pp. 3966–3969, Oct 2000. 4

[30] Y. Urzhumov and D. R. Smith, "Metamaterial-enhanced coupling between magnetic dipoles for efficient wireless power transfer," *Phys. Rev. B*, vol. 83, p. 205114, May 2011. 4, 20

[31] K. R. Catchpole and A. Polman, "Plasmonic solar cells," *Opt. Express*, vol. 16, pp. 21793–21800, Dec 2008. 7, 8

[32] C. E. Dungey and C. F. Bohren, "Light-scattering by nonspherical particles a refinement to the coupled-dipole method," *Journal of the Optical Society of America A*, vol. 8, no. 1, pp. 81–87, 1991. 8

[33] K. Catchpole and S. Pillai, "Surface plasmons for enhanced silicon light-emitting diodes and solar cells," *Journal of Luminescence*, vol. 121, no. 2, pp. 315–318, 2006. 9, 10, 11

[34] X. Wang, N. Waite, P. Murcia, K. Emery, M. Steiner, F. Kiamilev, K. Goossen, C. Honsberg, and A. Barnett, "Improved outdoor measurements for very high efficiency solar cell sub-modules," in *Photovoltaic Specialists Conference (PVSC), 2009 34th IEEE*, pp. 409–414, June 2009. 10

[35] A. Marti, P. A. Davies, J. Olivan, C. Algora, M. Terron, J. Alonso, J. Maroto, G. L. Araujo, J. Miñano, G. Sala, and A. Luque, "High efficiency photovoltaic conversion with spectrum splitting on gaas and si cells located in light confining cavities," in *Photovoltaic Specialists Conference, 1993., Conference Record of the Twenty Third IEEE*, pp. 768–773, May 1993. 10

[36] D. J. Friedman, J. M. Olson, and S. Kurtz, *High-Efficiency IIIV Multijunction Solar Cells*, ch. 8, pp. 314–364. John Wiley & Sons, Ltd, 2011. 10

[37] R. Winston and J. M. Gordon, "Planar concentrators near the étendue limit," *Opt. Lett.*, vol. 30, pp. 2617–2619, Oct 2005. 12

[38] P. Benítez, J. Miñano, P. Zamora, R. Mohedano, A. Cvetkovic, M. Buljan, J. Chaves, and M. Hernández, "High performance fresnel-based photovoltaic concentrator," *Opt. Express*, vol. 18, pp. A25–A40, April 2010. 12

[39] E. Lorenzo, *Energy Collected and Delivered by PV Modules*, ch. 20, pp. 905–970. John Wiley & Sons, Ltd, 2005. 13

[40] G. Climate and E. Project, "An assessment of solar energy conversion technologies and research opportunities," Tech. Rep. MSU-CSE-00-2, Stanford University, CA, USA, Summer 2006. 13

[41] Y. ming Wu, L.-W. Li, and B. Liu, "Gold bow-tie shaped aperture nanoantenna: Wide band near-field resonance and far-field radiation," *Magnetics, IEEE Transactions on*, vol. 46, pp. 1918–1921, June 2010. 13

[42] M. Schnell, P. Alonso-González, L. Arzubiaga, F. Casanova, L. E. Hueso, A. Chuvilin, and R. Hillenbrand, "Nanofocusing of mid-infrared energy with tapered transmission lines," *Nature Photonics*, no. 5, p. 283287, 2011. 13

[43] M. Bozzetti, G. De Candia, M. Gallo, O. Losito, L. Mescia, and F. Prudenzano, "Analysis and design of a solar rectenna," in *Industrial Electronics (ISIE), 2010 IEEE International Symposium on*, pp. 2001–2004, July 2010. 13

[44] A. M. A. Sabaawi, C. Tsimenidis, and B. Sharif, "Bow-tie nano-array rectenna: Design and optimization," in *Antennas and Propagation (EUCAP), 2012 6th European Conference on*, pp. 1975–1978, March 2012. 13

[45] E. Stefanakos, D. Goswami, and S. Bhansali, "Rectenna solar energy harvester," Feb 2012. US Patent 8,115,683. 13

[46] W. Brown and J. Triner, "Experimental thin-film, etched-circuit rectenna," in *Microwave Symposium Digest, 1982 IEEE MTT-S International*, pp. 185 –187, June 1982. 16

[47] R. Ramirez and F. De Flaviis, "A mutual coupling study of linear and circular polarized microstrip antennas for diversity wireless systems," *Antennas and Propagation, IEEE Transactions on*, vol. 51, pp. 238–248, Feb 2003. 16

[48] R. Vaughan and J. Andersen, "Antenna diversity in mobile communications," *Vehicular Technology, IEEE Transactions on*, vol. 36, pp. 149–172, Nov 1987. 16

[49] N. Zhu, R. W. Ziolkowski, and H. Xin, "A metamaterial-inspired, electrically small rectenna for high-efficiency, low power harvesting and scavenging at the global positioning system l1 frequency," *Applied Physics Letters*, vol. 99, no. 11, pp. 114101–114101–3, 2011. 16

[50] R. Gutmann and J. Borrego, "Power combining in an array of microwave power rectifiers," *Microwave Theory and Techniques, IEEE Transactions on*, vol. 27, pp. 958–968, Dec 1979. 16

[51] H. C. Torrey and C. A. Whitmer, "Crystal rectifiers," *MIT Radiation Laboratory Series*, Sep 1948. 17

[52] M. Sarehraz, *Novel rectenna for collection of infrared and visible radiation*. PhD thesis, University of South Florida, 2005. 18

[53] H. Odashima, K. Yamamoto, F. Matsushima, S. Tsunekawa, and K. Takagi, "Characteristics of metal-insulator-metal diodes as generators of far-infrared radiation," *Quantum Electronics, IEEE Journal of*, vol. 32, pp. 350–356, Feb 1996. 18

[54] C. Fumeaux, W. Herrmann, F. Kneubhl, and H. Rothuizen, "Nanometer thin-film ninioni diodes for detection and mixing of 30 thz radiation," *Infrared Physics and amp; Technology*, vol. 39, no. 3, pp. 123–183, 1998. 19

[55] D. Schurig, J. J. Mock, B. J. Justice, S. A. Cummer, J. B. Pendry, A. F. Starr, and D. R. Smith, "Metamaterial electromagnetic cloak at microwave frequencies," *Science*, vol. 314, no. 5801, pp. 977–980, 2006. 22

[56] N. I. Landy, S. Sajuyigbe, J. J. Mock, D. R. Smith, and W. J. Padilla, "Perfect metamaterial absorber," *Phys. Rev. Lett.*, vol. 100, p. 207402, May 2008. 22

[57] T. Chen, S. Li, and H. Sun, "Metamaterials application in sensing," *Sensors*, vol. 12, no. 3, pp. 2742–2765, 2012. 22

[58] S. I. Maslovski, P. M. Ikonen, I. Kolmakov, S. A. Tretyakov, and M. Kaunisto, "Artificial magnetic materials based on the new magnetic particle: metasolenoid," *Progress In Electromagnetics Research*, vol. 54, pp. 61–81, 2005. 23, 25

[59] X.-P. Zhang and S.-S. Zhong, "Resonant frequencies and dual-frequency operation of a bow-tie microstrip antenna," in *Antennas and Propagation Society International Symposium, 2002. IEEE*, vol. 2, pp. 60–63, 2002. 28

[60] X.-X. Yang, C. Jiang, A. Elsherbeni, F. Yang, and Y.-Q. Wang, "A novel compact printed rectenna for data communication systems," *Antennas and Propagation, IEEE Transactions on*, vol. 61, pp. 2532–2539, May 2013. 39

[61] H. Kanaya, S. Tsukamaoto, T. Hirabaru, D. Kanemoto, R. Pokharel, and K. Yoshida, "Energy harvesting circuit on a one-sided directional flexible antenna," *Microwave and Wireless Components Letters, IEEE*, vol. 23, pp. 164–166, March 2013. 39

[62] O. Ramahi, T. Almoneef, **Mohammed R. AlShareef**, and M. Boybay, "Metamaterial particles for electromagnetic energy harvesting," *Applied Physics Letters*, vol. 101, no. 17, pp. 173903–5, 2012. 39, 81, 93

[63] **Mohammed R. AlShareef** and O. Ramahi, "Arrays of electrically-small resonators for electromagnetic energy harvesting in the THz, infrared and visible frequency spectra and method to channel energy through waveguiding structures," 12 2013. US Patent 61912566. 39

[64] M. Bait Suwailam, *Metamaterials for Decoupling Antennas and Electromagnetic Systems*. PhD thesis, University of Waterloo, 2011. 42, 55

[65] R. Ziolkowski, "Design, fabrication, and testing of double negative metamaterials," *Antennas and Propagation, IEEE Transactions on*, vol. 51, no. 7, pp. 1516–1529, 2003. 42, 55

[66] D. R. Smith, S. Schultz, P. Markoš, and C. M. Soukoulis, "Determination of effective permittivity and permeability of metamaterials from reflection and transmission coefficients," *Phys. Rev. B*, vol. 65, p. 195104, April 2002. 42, 55

[67] **Mohammed R. AlShareef** and O. Ramahi, "Electrically small resonators for energy harvesting in the infrared regime," *Journal of Applied Physics*, vol. 114, no. 22, pp. 223101–6, 2013. 44, 81, 95

[68] M. Gratzel, "Photovoltaic and photoelectrochemical conversion of solar energy," *Philosophical Transactions of the Royal Society A: Mathematical, Physical and Engineering Sciences*, vol. 365, pp. 993–1005, April 2007. 52

[69] M. A. Ordal, R. J. Bell, J. Alexander, L. L. Long, and M. R. Querry, "Optical properties of fourteen metals in the infrared and far infrared: Al, co, cu, au, fe, pb, mo, ni, pd, pt, ag, ti, v, and w," *Applied Optics*, vol. 24, pp. 4493+, Dec 1985. 54, 78

[70] B. Ung and Y. Sheng, "Interference of surface waves in a metallic nanoslit," *Opt. Express*, vol. 15, pp. 1182–1190, Feb 2007. 54, 65

[71] M. A. Ordal, L. Long, R. J. Bell, S. Bell, R. R. Bell, J. Alexander, and C. Ward, "Optical properties of the metals al, co, cu, au, fe, pb, ni, pd, pt, ag, ti, and w in the infrared and far infrared," *Appl. Opt.*, vol. 22, pp. 1099–1119, April 1983. 54, 65

[72] H. Ehrenreich and H. Philipp, "Optical properties of ag and cu," *Physical Review*, vol. 128, no. 4, pp. 1622+, 1962. 54

[73] A. Inc., "http://www.ansys.com." ANSYS HFSS. 54, 78

[74] J. Baena, J. Bonache, F. Martin, R. Sillero, F. Falcone, T. Lopetegi, M. A. G. Laso, J. Garcia-Garcia, I. Gil, M. Portillo, and M. Sorolla, "Equivalent-circuit models for split-ring resonators and complementary split-ring resonators coupled to planar transmission lines," *Microwave Theory and Techniques, IEEE Transactions on*, vol. 53, no. 4, pp. 1451–1461, 2005. 55

[75] D. Qu, D. Grischkowsky, and W. Zhang, "Terahertz transmission properties of thin, subwavelength metallic holearrays," *Opt. Lett.*, vol. 29, pp. 896–898, April 2004. 68

[76] W. Withayachumnankul, B. S. Y. Ung, B. M. Fischer, and D. Abbott, "Measurement of linearity in thz-tds," in *Infrared, Millimeter, and Terahertz Waves, 2009. IRMMW-THz 2009. 34th International Conference on*, pp. 1–2, Sept 2009. 68

[77] D. M. Slocum, E. J. Slingerland, R. H. Giles, and T. M. Goyette, "Atmospheric absorption of terahertz radiation and water vapor continuum effects," *Journal of Quantitative Spectroscopy and Radiative Transfer*, vol. 127, no. 0, pp. 49–63, 2013. 68

[78] **Mohammed R. AlShareef** and O. Ramahi, "Energy harvesting in the microwaves spectrum using electrically small resonators," in *International Congress on Energy Efficiency and Energy Related Materials (ENEFM2013)*, vol. 155 of *Springer Proceedings in Physics*, pp. 265–272, Springer International Publishing, 2014. 94

[79] **Mohammed R. AlShareef** and O. Ramahi, "Electrically small particles combining even- and odd-mode currents for microwave energy harvesting," *Applied Physics Letters*, vol. 104, no. 25, pp. 253906–5, 2014. 94

[80] **Mohammed R. AlShareef**, B. Cui, and O. Ramahi, "Fabrication of infrared energy harvester using electrically small particles," in *Technical Proceedings of the 2014 Clean Technology Conference and Trade Show*, pp. 120–123, Clean Technology and Sustainable Industries, 2014. 95

[81] **Mohammed R. AlShareef** and O. Ramahi, "Electrically small particles for harvesting and channeling infrared energy," in *Antenna Technology and Applied Electromagnetics (ANTEM), 2014 16th International Symposium on*, pp. 1–2, July 2014. 95